Zeeman Deceleration of Supersonic Beam trapping of Paramagnetic Atoms in a Traveling Magnetic Wave

Manabendra Nath Bera

UNIVERSITÉ PARIS-SUD XI
U.F.R. SCIENTIFIQUE D'ORSAY

THÈSE

présentée pour obtenir le grade de

DOCTEUR EN SCIENCES
DE L'UNIVERSITÉ PARIS-SUD XI

par

Manabendra Nath BERA

Zeeman Deceleration of Supersonic Beam: Trapping of Paramagnetic Atoms in a Traveling Magnetic Wave

Soutenue le 28-03-2011 devant la commission d'examen composé de :

M. Francisco Perales	Rapporteur
M. Christian Bordas	Rapporteur
M. Osman Atabek	
M. Sebastiaan Y.T. van de Meerakker	
M. Nicolas Vanhaecke	
M. Pierre Pillet	Directeur de thèse

Laboratoire Aimé Cotton, CNRS, Université Paris-Sud XI - Campus scientifique d'Orsay, Orsay, France

Contents

ABSTRACT

This thesis describes the transverse guiding, longitudinal guiding and deceleration of supersonic beams of paramagnetic atoms by confining them in a co-moving magnetic trap. Much of the work presented in this thesis are, experimentally, the construction of the beam machine suitable for producing cold supersonic beams of atoms, various magnetic coils to form moving 3D-magnetic trap and the associated electronics, from scratch and this volume is dedicated to the technical development to build up a Zeeman decelerator using traveling magnetic waves which was the focus of my graduate work.

In the experiment we use two different atomic species that are helium and argon. The beam of helium is used to characterize the molecular beam machine as it has highly energetic metastable state which is easy to detect. The beam of argon is transversally guided and subsequently used to demonstrate the 3D-guiding and finally the deceleration. The cold pulsed beams of metastable atoms have been produced by first, supersonically expanding through $Liq.N_2$ cooled valve and then, excite them to the metastable state by electric glow discharge. The technics to produce stable discharge at $Liq.N_2$ temperature have been studied and presented. A beam of metastable helium with mean velocity $1220m/s$ and longitudinal temperature $13K$ and a beam of metastable argon with mean velocity $470m/s$ and the longitudinal temperature $10.5K$, have been produced in the experiment.

The traveling magnetic trap is formed by the combination of the magnetic fields from a quadrupole magnetic coil and a specially designed planner magnetic coil. The quadrupole magnetic coil connected to DC current produces a static magnetic field with the only field gradient along the transverse direction to the beam. The planner magnetic coil connected to AC current is capable of producing a sinusoidal traveling magnetic wave with the magnetic field gradient along the axial direction. With the home-built electronics, the planner coil can produce a magnetic wave with the amplitude of 0.69T (with 300A AC current) and the oscillation frequency of 40kHz. This results a traveling magnetic wave with velocity $464m/s$.

Several proof-of-principle experiment have been carried out using metastable cold and pulsed argon beam. We have studied the guiding properties of the quadrupole guiding

coil with different driving currents and atomic species (metastable helium and argon). The number of metastable argon atoms arriving to the detector through a long, narrow glass tube, can be increased by 4 times at end of the guide with 100A guiding current than non-guiding beam while it is 1.5 times for metastable helium. The guiding efficiency and transmission of the atoms at the end of the quadrupole guide has been understood and compared to the theoretical prediction by 3D-trajectory simulations. The metastable beam of argon has been 3D-guided at various velocity ($464m/s, 400m/s, 392m/s$) with the 28cm long decelerator. The temperature of the guided beam packet is observed to be 100mK. The 3D-guiding experiment demonstrates the capability of real 3D-trapping in the moving frame by the decelerator. Subsequently, the Zeeman deceleration experiment has been performed with metastable argon beam from initial velocity $400m/s$ to final velocity $380m/s$ and $370m/s$. Another set of experiment has been performed to decelerate from the initial velocity $392m/s$ to the final velocity $365m/s$. The number of transmitted atoms after the deceleration are expected to be reduced as the confining potential along the axial direction. The higher axial magnetic potential along with a longer decelerator is expected to produce more number of decelerated atoms and to bring them stand still in the laboratory frame which is the immediate next goal of the experiment.

Acknowledgement

The man is the product of process. I ackowladge and thank all, knowingly or un-knowingly, who contributed to this process and brought me to this stage.

First of all, I would like to express my deepest gratitude and thank to my supervisors M. Pierre Pillet and M. Nicolas Vanhaecke. Thank you for your guidance and boundless patience. I am very proud that I was given this opportunity working in your group. Thank you for support during my time in Paris and beyond. I also would like to thank M. Jacques Robert who taught me a lot on various topics ranging from problems in my experiment to fundamental questions in quantum field theory.

I am thankful to all my fellow, past and present group members and friends Sana Amairi and Azer Trimeche, whom I worked with during their master thesis or PhD thesis. Many of the success we accomplished during last two years were the group efforts and these are the main reason why I am writing this thesis using the pronoun *'we'*. Another person from whom I learned a lot is you, the tall Nicolas Saquet (I call him t-NiCo!). I really would like acknowledge and thank you for your helps. In particular, I'll never forget the time we spend outside the lab and your PhD jokes. I also greatly enjoyed to work with Anne in the same experimental room. Thanks a Ton Anne, although you sometime 'unnerved' me with your constant fears of leak or with your sodium barrel!

We are privileged to have excellent technical and administrative support in our laboratory. Much of this experimental work involving mechanical and electronics development only got done because of their efforts. I am thankful to all from mechanical and electronic workshops.

During my stay at Laboratoire Aimé cotton, I have strongly interacted almost all the members of the laboratory and enjoyed their company a lot. I would like to thank all of them, without listing everybody, for making the laboratory a nice place to work.

Finally, I sincerely thank my teachers, my parents, uncles and aunts, beloved brothers and sisters and my dear friends. Their genuine interest in and enthusiasm for what I do, is a constant motivation for me to be not only a good scientist but also a good human being.

Chapter 1

General Introduction

No amount of experimentation can ever prove me right; a single experiment can prove me wrong. - Albert Einstein

1.1 A search for new Physics: Precision Spectroscopy

In the beginning of the last century the physicists believed that the fundamental forces of the nature are invariant under the operations of various discrete symmetries (like, Parity (P), Time-Inversion (T) and Charge Conjugation (C)) and the continuous symmetry (e.g., Lorentz Invariance). In 1927, Wigner [1] discovered that the P and T are symmetries of Schrödinger equation and subsequently C was found to be a symmetry of Quantum Electrodynamics (QED) [2]. The development of the standard model of particle physics and the introduction of the strong and weak forces to explain the dynamics and stability of the atomic nucleus also were assumed to hold these symmetries, since there is no classical analogues of the new interactions.

In 1956, for the first time, it was suggested that the symmetry due to Parity is violated in the weak interaction [3]. Subsequently, in the next year it has been observed experimentally by Wu and co-workers in the β decay of polarized ^{60}Co [4]. Earlier in 1957, Landau proposed that the symmetry could be preserved at a much deeper level in the weak interaction [5]. After the Parity violation, physicists put all the other discrete symmetries on trial, but it was generally believed that the combined symmetries are still be conserved. In the year 1964, another breakthrough has been achieved with the discovery of non-conservation of combined Parity (P) and Charge conjugation (C) symmetry of the neutral long lived K-meson [6]. A history of the discovery of CP-violation and its consequences are well documented in [7, 8] and in the reviews [9, 10]. They have profound impacts on the understanding of the foundations of the weak force, one of the key ingredient of the standard model of particle physics. The theoretical understanding of weak interactions was mathematically unsatisfactory until the late 1960s, when a new theory was suggested independently by Glashow [11], Weinberg [12] and Salam [13]. According to this new theory the weak interactions and the electromagnetic interaction could be understood as different manifestations of a single underlaying interaction: the electro-weak interaction [14]. An important prediction of the theory was the existence of new particles such as neutral Z boson. However, it fails to give a deeper understanding of the physics that it describes. There are questions that are still unanswered for example, why there are three generations of fermions? What determines the masses of the particles? It also cannot explain the Big Bang baryogenesis which generally believed as a consequence of CP violation.

The development of various methods to produce cold and ultra-cold atoms, ions and molecules and their high resolution spectroscopy enormously contribute to metrology, measurements and tests of the fundamental constants and fundamental physical theories. With the help of single-ion precision measurement, the electron magnetic moment [15] and the fine structure constant α [16] have been measured with an unprecedented accuracy.

The implementation of atomic, molecular beams along with electric and magnetic resonance techniques allows to precisely determine the Rydberg constant [17], the Lamb shift in hydrogen atom [18]. The atomic and molecular physics tests exploit the low-energy (1eV) phenomenas which are particularly interesting to explore the fundamental physics in this energy scale as well as they are sensitive to new physics as the manifestations of the fundamental symmetry violations. In the following subsections, we shall briefly outline them.

1.1.1 Parity non-conservation

In particle physics, the weak interactions are mediated by the Z^0 (weak neutral current interactions) are very different from the charge current interactions by W^+ or W^- [19]. Atomic parity violation (APV) can measure set of model-independent electron-quark neutral coupling constants those are different from those can be accessed by the high energy experiments. In fact, atomic parity violation constrains on new physics beyond the standard model. The measurements determine the weak charge Q_w which quantify the electro-weak coupling strengths between the atomic electrons and the quarks of nucleus [20, 21]. The observation of the parity non-conservation was seen by Wieman and co-workers [22], for the first time, with atomic ^{133}Cs and later by Budker and co-workers [23] with atomic ^{174}Yb. So far, these are the only experiment to measure the nuclear anapole moment which is due to the parity violation. However, other experiments are proposed and underway probing different couplings in weak interactions, like [24–26] (e.g., coupling between electron-vector and nucleon axial-vector currents).

Along with the manifestation of parity non-conservation in the interactions between the elementary particles, one might wonder whether nature can choose some handedness over the others, in the macroscopic scale [27, 28]. For example, DNA, the basic building block of all living organisms, have right-handed helical structure. Why its chosen to be preferred over the left-handed helical structure? Why all living organisms exclusively contains left-handed amino acids? A chiral molecule, which is left-handed enantiomer, completely resembles all the thermodynamic properties like, density, boiling and melting points to the right-handed enantiomer however, shows drastically different bio-chemical properties. Does weak-interactions explain the mechanism behind these differences? A very sensitive experiment, to date, has been carried out based on saturation spectroscopy of two different enantiomers of $CHFClBr$ molecule [29]. However no parity-violating effect (the frequency difference between the enantiomer) has been observed at the sensitivity of 2.5×10^{-13} level. The next generation experiments are under way with heavier molecular beam and improved resolution techniques.

1.1.2 Testing the Time-Reversal Invariance: eEDM

The CPT theorem which requires the invariance under all three discrete symmetries C, P and T is believed to be conserved, implies a system has to violate T-symmetry if it violates CP-symmetry [30, 31]. The only system has been seen to violate T-symmetry is the Kaon. The standard model of particle physics considers T-symmetry to be not exact but nearly exact for the fundamental particles like, electrons, protons and neutrons [32, 33]. It has been proposed that electron and other fundamental particles have an electric dipole moment (EDM) as a consequence of breakage of both T and P-symmetry. The standard model predicts the EDM of electron less than $10^{-38} e\ cm$ where e is the charge of electron and it is too small to be measured experimentally. The standard model also fails to account for the predominance of matter than anti-matter in the universe [34]. However, various extension of standard model predicts the values within the range of $10^{-25} - 10^{-26}\ e\ cm$ which is very close to the current experimental limit [35] while the experiment has been carried out by measuring the differential Stark shift in atomic thallium. The observation of electron EDM demands extremely high electric field to observe the energy shift due to different alignments of the dipole along the quantization axis. It is advantageous to use heavy atoms and molecules as they offer higher sensitivities to the electron EDM. This is because, they can have high effective electric field ($E_e = QP$ with Q is the factor which includes all the details of the atomic or molecular system and P is the degree of polarization) inside the atom (for Th it is $\sim 70 MV/cm$) which far larger than the field could be produced in the laboratory. The effective electric field can be even larger in the heavy polar molecules than that of atoms [36]. Because for the polar molecules, $P \sim 1$ at a modest external electric field. A series of experiments are ongoing which use the polar molecules as high-electric-field laboratory. The experiments exploits either molecular beam or traps of neutral molecules including molecules YbF [37], PbO [38] and ThO [39] along with the other molecular systems. Several others have been proposed as viable candidate [40–44]. The use of the cold molecules in the sub-kelvin regime can increase the sensitivity to electron EDM by orders of magnitude [45]. Therefore, a search for the electron EDM is also a search for new physics beyond standard model.

1.1.3 Temporal Variation of the Fundamental Constants

The development and the basic understanding of physics relies on the fact that laws of nature do not differ from one point of space-time to the other in the universe. The theories unifying gravity with the other interactions suggest however, temporal and spatial variations of the fundamental 'constants' which quantify these interactions, in the expanding universe. The indication of the variation of the fundamental constants includes

fine-structure constant, strength constant of strong-interaction and the masses from Oklo natural nuclear reactor data and the observed quasar absorption spectra [46]. The recent observations from the measurements [47] of the variation of atomic (^{133}Cs) frequency at different distance from the Sun (the variation in distance is due to the ellipticity of the Earth's orbit), put a strong limit on the variation of fine-structure constant. The precision spectroscopic measurement of the Λ-doublet microwave transitions of the Stark decelerated cold OH molecules give a sensitivity of 1 part per million to change the fine structure constant ($\triangle\alpha/\alpha$) over $\sim 10^{10}$ years [48].

Similarly a strong limit has been drawn on a variable proton-to-electron mass ratio (μ) at $\triangle\mu/\mu \sim 1.2 \times 10^{-16} year^{-1}$ from the absorption lines from the molecules in the distance universe [49].

1.2 Quantum Phases, Cold Collision and Quantum Chemistry

The development of the (ultra)-cold atoms and molecules open various avenues to explore physics and chemistry in the low temperature regime. In an ultracold temperature the de Broglie wavelength associated with the particles become comparable (or even larger than the inter-particle separation), leads to various quantum phenomenas (depending on the spin) which cannot be seen at higher temperature. By cooling down a trapped Bosonic gas at some point, all the particles suddenly jump to the lowest trap state leads to a Bose-Einstein condensation, first observed in 1995 [50]. In this phase of matter the particles are indistinguishable from each other and behave like a super-particle. For Fermionic gas, by cooling down does not lead to shrink all the particles to one trap state due to the 'Fermi pressure' as the consequence of the Pauli exclusion principle. The first Fermi gas [51] has been produced the laboratory in 2001. The direct measurement of the phase transition from an incompressible superfluid to a Mott insulator [52], has been observed for the first time in 2002. Studying molecules in the quantum regimes are extremely interesting as they provide the properties like dipole moments, multiple internal degrees of freedoms like vibration and rotation which are absent for the atoms.

The development of the various molecular cooling and deceleration techniques enable us to investigate the elastic and inelastic cross-sections, due to the tunability of the velocity which provides the control over the collision energy. At low velocity the collisional dynamics are determined by the quantum effects. Mostly, the inelastic collision occurs more frequently than the elastic collision [53] and the cross-section becomes extremely sensitive to the internal structure of the collision partners, in this regime. A slight change of the internal state e.g., by applying external fields, can significantly change the final

products after the collision [54]. The long duration of the collision leads to the tunneling through repulsive potential even at zero temperature as has been observed from theoretical study [55]. Further, a van der Waals resonance state [56–58] can occur close to the tunneling and gives rise to completely different collision phenomenas.

Recently, there are several collision experiments that have been performed between Stark decelerated OH molecules and Xe [59], He and D_2 [60] ranging over several hundreds of cm^{-1}. It is expected that these experiments shall be marked as the beginning of the new type of chemistry experiment where the reaction can be completely controlled.

1.3 Towards Cold Molecular Ensembles

In 1950s the supersonic jet expansion introduced the first method to produce cold gaseous sample of molecules in the laboratory [61]. It introduced one of the very first methods to perform spectroscopies on radicals. The cold molecules were also produced from superfluid liquid helium droplets [62], which resembles the properties of the gas phase molecules. In 1980s the methods for the laser cooling have been developed [63]. The laser cooling technique relies on the fact that the atoms can be cooled by successive rapid absorption-spontaneous emission cycle in an atom when they are placed in a resonant light field. In every absorption-emission cycle the atom changes its momentum due to the photon recoil. By exploiting this effect and with additional external magnetic field to manipulate the atomic energy levels, the magneto-optical-trap (MOT) has been developed which is routinely used for producing ultracold atoms at temperature below 1mK with density of $10^{10} cm^{-3}$. The Doppler effect and the presence of external magnetic field provide a position and velocity dependent force in a MOT. As a result, the atoms experience a friction force damping their motion in the light field. Along with the dissipative spontaneous emission, this friction force leads to a compression in phase-space density. With the development of polarization gradient cooling and evaporative cooling the atoms can be cooled to nano-Kelvin temperature.

The realization of cold atomic ensembles have introduced the fascinating physics in the ultra-cold regime. The cold atomic samples have been used to study various quantum phases of matter [64–66], quantum optics [67], precision spectroscopies, atomic clocks [68], many body physics [69], along with the other numerous applications [70].

The molecules are difficult to cool by the laser cooling techniques as they have additional complex rotational and vibrational freedoms [71]. The branching ratios of various rotational de-excitation channels are in the order of unity [72]. Although, the rotational state repumping can be done but the leakage from various vibrational states are significant for most molecules which requires a large number of repump laser. However, various

effort have been made with certain molecules those have nearly diagonal vibrational state coupling matrices [73, 74]. Various techniques other than the laser cooling of molecule can be found in [75].

1.3.1 Photo-association and Magneto-association

There are two association techniques which lead to cold molecules starting from ultracold atoms [75]. In photo-association, the frequency of the photon is tuned in such a way that, two atoms resonantly absorb one photon to produce a molecule in a ro-vibrational level which belongs to an excited electronic state. In other words, the photon couples two atoms from an unbound continuum energy state on ground-state potential to a bound excited state. Subsequently it can reach to a bound state of the lower potential by emitting different wavelength photon. The produced excited molecules are translationally cold with the similar temperature of the atoms. As the photo-association efficiency depends on the wave function overlap between the lower unbound and the upper bound state, the molecules are formed in a vibrationally excited level in the initial bound state. Although, several schemes have been developed to produce molecules in vibronic ground state [76, 77]. The photo-association technique successfully applied to the alkali atoms to produce homonuclear molecules like, Rb_2 [78, 79], Na_2 [80], Li_2 [81], Cs_2 [82], K_2 [83], Ca_2 [84], H_2 [85], He_2^* [86]. The heteronuclear molecules are difficult to produced due to the molecular potential. However there are several heteronuclear (polar) molecules which are produced using photo-association technique in the laboratory such as $NaCs$ [87], KRb [88], $RbCs$ [89]. One of the major problem in photo-association is the molecular relaxation by spontaneous emission of photon which leads to the dissociation of the molecule into two independent atoms with higher kinetic energy than initially they had. It can be understood as the photoassociation is long range effect whereas a stable vibrational motion occurs at a shorter range of distance, in ground state molecule. The photo-association of atoms in a Bose-Einstein-Condensate also has been demonstrated [90–92].

Another association method to create ultracold molecule directly out of ultracold atoms is the magneto-association, referred as Feshbach resonance [93]. When the total energy (i.e., the scattering energy) of two atoms, which are interacting on a interaction potential, becomes closer to a bound state of a higher energy interaction potential, the Feshbach resonance occurs and the molecules are formed. This is possible because of the presence of different magnetic moments between the upper and the ground state interaction potential and the energy of the bound state can be tuned with respect to the ground state interaction potential. It relies on the adiabatic passage through a scattering resonance between two ultracold atoms which is tuned by the magnetic field applied on them. The first observation of coherence between atoms and molecules near a Feshbach

resonance has been achieved in a ^{85}Rb Bose-Einstein-Condensate [94]. Subsequently, the magneto-association has been used to produce ultracold Li_2 [95], Na_2 [96], K_2 [97], Cs_2 [98] molecules. There are few heteronuclear molecules that have been proposed to be produced using Feshbach resonance and several experiments are underway [93, 99]. The first production of heteronuclear LiK molecule [100] at the Feshbach resonance has been carried out recently.

To produce ultracold molecule, the association processes have played and currently playing crucial role, indeed. With the development of the new ideas, such as optical Feshbach resonance [101], coherent control of molecular dynamics [102], the association processes hold great promise in the future [103].

1.3.2 Buffer-gas Cooling

Before the advent of the laser cooling techniques, the conceptually simple cryogenic buffer-cooling technique has been used to produce cold atomic hydrogen to milli-Kelvin temperature. The method relies on the sympathetic cooling via elastic collisions with the buffer gas. Since all other species except He have much higher binding energies with cold surfaces (buffer-gas covered) with a temperature at which loading of the trap is possible, He is used as the buffer-gas thermalizing the atoms due the elastic collisions achieving low enough temperature to be loaded in a magnetic trap before they touch the cold surface. The method is very general i.e., it does not require the atoms or molecules possessing either electric dipole moment or particular optical transitions. That only requires the atoms or molecules to be paramagnetic. In order to ensure the atoms or molecules are thermalized (by enough number of collisions) on a small length (smaller than a cell, $\sim 1cm$) before they impinge on the wall, the density of the buffer gas needs to be high enough which puts the lower limit on the buffer-gas temperature. For example, the temperature can be used for ^3He and ^4He are $240mK$ and $800mK$, respectively.

The technique has been developed by the Doyle's group at Harvard [104] and has been used to demonstrate cooling and trapping the paramagnetic europium [105] and chromium [106], which were vaporized by ablating laser in the cold ^3He gas inside the cryostat. A temperature as low as $250mK$ has been achieved for atomic europium with the thermalization time of $30ms$. Due to the large magnetic moment of Eu (in $^8S_{7/2}$, $m_j = 7/2$), 1×10^{12} Eu atoms easily be loaded in a magnetic trap with the density of $5\times10^{12}cm^{-3}$ and can be stored in the trap for more than $100s$. As the technique does not depend on the internal structure of the species to be cooled (relies on elastic collision), the atoms those cannot be cooled by the conventional lase cooling techniques and even the molecules can be cooled using this method with the only requirement that they have to posses a magnetic moment. The molecular species: Calcium Monohydride (CaH) has been cooled

and trapped using this technique [107]. Approximately, 10^8 CaH molecules with a density of $8 \times 10^7 cm^{-3}$ were trapped at a temperature of $400 \pm 50mK$ with a trap life time $0.5s$. The further cooling of CaH using standard evaporative cooling is not possible since the time required to pump down the buffer gas ($\sim 20s$) exceeds the trap lifetime.

1.3.3 Velocity Selection

The method relies on the fact that the slow molecules which are already present in the room temperature velocity distribution, can be filtered out by the use of curved electric and magnetic fields. In the early fifties, the first attempt (unsuccessful) attempt had been made to distilled the slow atoms out from a hot beam using gravity [108]. However the first successful implementation of this method carried out in 1999 [109] to produce slow Li atoms from a thermal beam by the use of curved magnetic field. The atoms having sufficiently low enough kinetic energy can only be guided in the curved magnetic field and filtered out.

The realization of this technique for polar molecules is almost identical [110] except the bend electric guide is used exploiting the Stark effect associated with the polar molecules. The bend determines the upper limit of maximum longitudinal velocity can be guided. The molecules like Formaldehyde ($HCHO$) and deuteriated ammonia (ND_3) are produce in the laboratory using this technique. The flux of approximately $10^9/s$ $HCHO$ and a longitudinal temperature of a order of Kelvin has been achieved. Recently, this method has been implemented to study cold collision between neutral CH_3F molecule and ionic Ca^+ [111].

1.3.4 Stark Deceleration

The Stark deceleration is a general method to produce slow polar molecules starting from a supersonic molecular beam which has been introduced about a decade ego [112]. The technique exploits the fact that the pulse of polar molecule emerging from a pulsed supersonic beam can be decelerated by time dependent switching of the static inhomogeneous electric fields. In the decelerator, the inhomogeneous electric fields are created by series of pairs of parallel electrodes placed along the beam axis. The polar molecules possessing positive Stark shift (low field seeking state) while approach an electrode pair gain Stark energy (potential energy). As the consequence, molecules are decelerated by the inhomogeneous electric field since the total energy of the molecules is conserved. If the field is still switched on after the molecules pass the field maximum between the electrodes, the molecules are accelerated and finally gain their initial velocity. In the Stark decelerator, the field is sharply switched-off before the molecules reach the field maximum to prohibit

the acceleration along the descent. This switching-off of the applied electric field are too fast to be followed by the molecules results, the molecules keep their velocity unchanged with the instantaneous velocity prior to the switching of the field. By repeating this process in a cycle, a fixed amount of kinetic energy can be extracted from the molecules as they pass through each pair of electrodes and the molecules can be brought to rest.

The first demonstration of deceleration of polar molecules using Stark deceleration has been carried out on a pulsed beam of neutral metastable CO (in $a^3\Pi$) molecules from $225m/s$ ($E_{kin} = 59cm^{-1}$) to $98m/s$ ($E_{kin} = 11cm^{-1}$) [112]. An array of 63 synchronously pulsed electric field stages were used in the decelerator to carry out the deceleration along with radially guiding the molecules through out the process. There are several other molecular species like ND_3 [113], H_2CO [114], SO_2 [115], and CHF_3 or radicals like OH [116, 117], OD [118], NH [119] etc. that have been decelerated since the first demonstration of the Stark decelerator. Once the molecules are brought to stand still, they can be confined in electric traps [113], magnetic traps [120] or storage rings [121].

1.3.5 Zeeman Deceleration Using Pulsed Magnetic Fields

Analogous to the Stark decelerator, the Zeeman decelerator has been developed [122, 123] to decelerate a beam of paramagnetic atoms and molecules applying an external inhomogeneous magnetic field. The method relies on the Zeeman shift in presence of magnetic field to exert a force on the atoms or molecules which is proportional to the gradient of the magnetic field. The inhomogeneous magnetic fields are generated by series of solenoids (field stages) placed coaxially to the atomic or molecular beam axis. Similarly as in Stark decelerator when the paramagnetic atoms with positive Zeeman shift (in low field seeking state) approach one field stage, gain in potential energy with the cost of loss in kinetic energy, until they reach the field maximum. It leads to the deceleration as the total energy of the atoms are conserved. If the applied field is not switched-off and let the atoms pass through the whole field stage the atoms get accelerated as the exit the field stage and the resultant change in kinetic energy becomes zero, means no overall deceleration. On the other hand if the applied field is switched-off sharply before the atoms reach the field maximum, the acceleration during their exit from field stage can be avoided. The atoms loose some of their kinetic energy as they climb up the potential hill and reduce their velocity until the time field is applied and stay with this instantaneous velocity after the applied field is switched-off since the switching-off the applied field is too fast to be followed by the atoms. With the repetition of the cycle between the switching-on and the switching-off before the atoms reach the field maximum, a substantial amount of kinetic energy can be extracted and the atoms can be brought to a stand still.

Using this technique, Merkt's group has performed the successful deceleration of H

atoms from $313m/s$ to $225m/s$ [122] using 6 pulsed magnetic field stages and of D atoms from $422m/s$ to $367m/s$ using 7 pulsed magnetic field stages while Raizen's group has carried out the deceleration of Ne atoms from $446m/s$ to $56m/s$ using 18 pulsed magnetic field stages [124]. The molecular oxygen has been decelerated from $389m/s$ to $83m/s$ [125] using 64 magnetic field stages. The first experimental realization of magnetic trapping after the Zeeman deceleration has also been reported with H atoms from an initial velocity of $520m/s$ [126].

In both the Stark and Zeeman deceleration techniques, the field stages e.g., the electrodes for the Stark decelerator and solenoids for the Zeeman decelerator, that are used to manipulate the longitudinal motion (due to the longitudinal field inhomogeneity) are also used to radially confine the beam during the deceleration process. That introduces few constraints on the deceleration efficiency of the beam. Because of that there are new approaches which have been made towards new generation decelerators. These include Stark decelerator with different mode of operation [127], using traveling potential [128]. A proposition for the Zeeman decelerator with different mode of operation also has been made recently [129].

1.4 This Thesis

Inspired by the recently introduced multi-stage Zeeman decelerator and considering it's various constraints on the deceleration efficiency, we have built a Zeeman decelerator which has two independent magnetic field sources. One of them is to manipulate the longitudinal motion and the other one is to manipulate the radial motion of the beam, independently. The thesis describes this newly developed technique of Zeeman deceleration of paramagnetic atoms which uses the traveling magnetic waves (for deceleration) along with an additional quadrupolar magnetic field (for radial confinement). The Zeeman shift of the paramagnetic atoms in presence of the magnetic field is exploited to decelerate translationally cold atoms produced by pulsed supersonic expansion. The produced beam pulses have translational temperature of about $\sim 10K$, however have a mean velocity of several hundred m/s. The metastable argon atoms in $^3P_2$ has been chosen to demonstrate the first deceleration experiment. To produce the traveling magnetic waves, different kinds of magnetic coils are developed and implemented. A huge development for the electronics to drive the magnetic coils have been carried out, but cannot be included in this thesis as it is subjected to a patent.

The experimental works are presented as have been carried out during this thesis, in three parts, which have been partitioned in three chapters. First, the development of a new supersonic beam machine to produce translationally cold metastable atomic beams

along with the detection apparatus which have been described in Chapter 2. The chapter starts with the general properties of a supersonically expanded beam and progressively introduces the finer details of beam machine set-up, the creation, stabilization and the characteristics of the produced metastable atomic beams.

The Chapter 3 serves to illustrate the transverse magnetic guiding of metastable argon and helium beams. It includes the details of the Zeeman effect of helium and argon atoms, quadrupole guiding coil and its working principle. The chapter ends with the experimental results regarding the quadrupole transverse guiding, numerical simulations and the discussions.

In the Chapter 4, a thorough description has been considered to introduce the newly developed Zeeman deceleration method. At the beginning of the chapter, we discuss the working principle of the conventional Zeeman decelerator made of pulsed magnetic field and an attention has been drawn to highlight the major difficulties and the limitation of this method which are expected to be overcome using the new Zeeman decelerator developed during this thesis. Then we present two different kinds (although have same topological structure) of magnetic coils with the minute details of the produced magnetic field by the coils and finally the coil used for the Zeeman decelerator. Subsequently, the deceleration principle and the longitudinal motions of atoms during the course of 3D-guiding and deceleration are considered. Then we introduce the recent experimental results concerning the 3D-guiding and decelerations along with the numerical simulations supporting the experiment. The chapter finishes with the conclusion.

Chapter 2

Realization of a Supersonic Beam

I have tried to read philosophers of all ages and have found many illuminating ideas but no steady progress toward deeper knowledge and understanding. Science, however, gives me the feeling of steady progress: I am convinced that theoretical physics is actual philosophy. It has revolutionized fundamental concepts, e.g., about space and time (relativity), about causality (quantum theory), and about substance and matter (atomistics), and it has taught us new methods of thinking (complementarity) which are applicable far beyond physics. — Max Born

2.1 Introduction

In the development of modern physics, study of corpuscular beams has been played and is still playing a very important role since the last two centuries. It has initiated the study of directional beam of particles at such low pressure that the collisional effects between the particles are negligible in most of the cases. It has opened up the most direct and the most simple way to investigate streams of moving elementary particles, to obtain information about their properties. As soon as 1879, the beam of charged particles have been investigated by Sir William Crookes to establish the corpuscular character of cathode rays, which was finally recognized as a stream of free electrons. This is still consider to be a very important milestone in the progresses of modern physics. Later in 1894, the beam of positively charged particle has been observed and studied by E. Goldstein, which finally led to the discovery of proton. The first realization and study of neutral particles, i.e., atoms or molecules moving in straight line with a thermal velocity, has been carried out by Dunoyer [130] in 1911. Subsequent to Dunoyer's pioneering work, the work by O. Stern and collaborators recognized the real importance of molecular beams as a research tool, which has indeed led down many of the principles of molecular beam techniques [131, 132].

The precision measurements and the studies of nuclear, atomic or molecular properties were introduced by Rabi and collaborators using beam resonance method [108, 133] in 1938. The resonance method has been applied to measure nuclear magnetic moments, molecular radio-frequency spectroscopy [134] , determination of atomic states [135]. Following the track, the beam methods are still used for studying high precision spectroscopy testing fundamental physics [39, 136], matter-wave interferometry[137], cold-collisions[59, 120], high-resolution spectroscopy of molecules [138–140] including biologically important macro-molecules [141].

The principle behind achieving higher resolution and higher precision in various experiments needs cold ensemble to reduce the various broadening effects (like, Doppler effect, collisional broadening etc.), to access longer interaction time with the ensemble, to have precise informations of particles degrees of freedoms and finally, to have a fine control over them. At the end of the last century, another important milestone in modern physics has been made with the invention of the laser cooling techniques [142–144]. With the help of evaporative colling, it makes possible to achieve extreme low temperature (few nK above the absolute zero) for an atomic gaseous ensemble which can led to Bose-Einstein-Condensation [145, 146], a quantum phase of matter. It has initiated a new area in physics, in which particles interaction and their statistics, rather than single particles, are at center stage[147]. It has triggered the physicists to dream having even precise control over particle's motions. Unfortunately, this laser cooling technique work

for a small number of atomic systems and very little progresses have been made for laser cooling of molecules due to the difficulties to isolate a close two level transition (see for example[148]). For molecules, other techniques have been developed parallely, for realizing cold molecular ensembles,like various deceleration techniques of molecular beams. Generally, the gaseous ensemble is cooled to a few Kelvin using adiabatic supersonic expansion of the gas in the vacuum. Next, the deceleration techniques of supersonically expanded beam are used to prepare cold molecular sample. The deceleration techniques relies on time varying inhomogeneous electric, magnetic and optical fields which interact with the particles in a particular quantum state and these processes are phase-space conservative, means by this way we cannot cool the ensemble further. But what these methods can do, is filtering out a particular velocity class with a narrow velocity spread, then decelerate and finally stop them. Following the same track, in our deceleration experiment, we are using supersonically expanded atomic and molecular beam.

In this chapter our aim is to give a detailed description of the experimental set-up which we have built during my thesis. It covers both the theoretical concepts (in brief) and their experimental realizations. The structure of this chapter is as follows. After a brief discussion on the properties of a supersonic beam in section.2.2, we give an overview of our supersonic beam-machine in section.2.3. Then we describe the realization of supersonic beam in the laboratory in section.2.4. The section.2.5 describes the production of metastable atomic beams which includes a brief overview of gas discharge and their experimental realization. Then in section.2.6 and section.2.7 we discuss about the glass-tube section and the detection device, respectively. The section.2.8 contains experimental results, the characterizations of helium and argon beams. Finally we finish the chapter with the conclusion in section.2.9.

2.2 The Supersonic Beam

Beams of atoms and molecules are produced by letting them expand through a small orifice (of a nozzle), from a reservoir to a vacuum chamber.

Depending on the relative dimensions of the orifice and the mean free path (the mean path it travels before it collides with another atom or the wall), the expansion dynamics leads to different kinds of beams. If the orifice of the nozzle is much smaller than the mean free path the velocity distribution before and after the expansion will be the same. These kinds of beams are called effusive beams. If the orifice is much larger than the mean free path which can be achieved by increasing the pressure in the reservoir, the dynamics of the expansion drastically changes, because the particles can collide frequently while they are passing through the nozzle. As a result, the expanded beam has a different

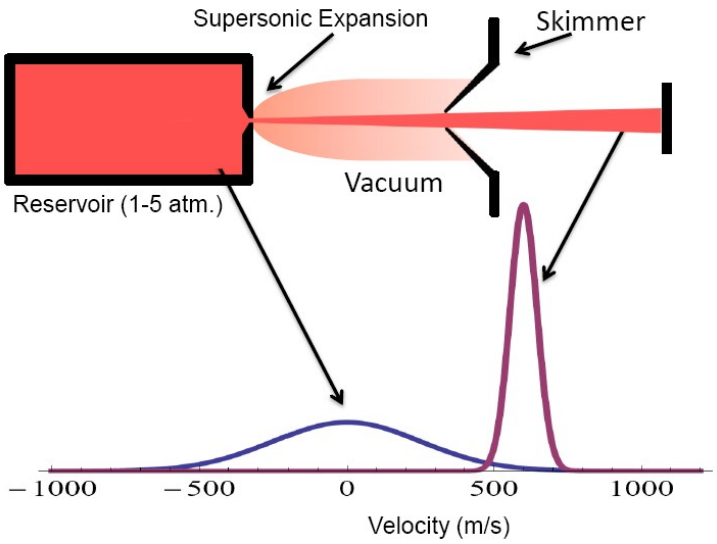

Figure 2.1: A schematic view of a supersonic expansion. A neutral beam is extracted from a high pressure gas source into a low pressure ambient background through supersonic, continuum free jet expansion. the lower figure shows the velocity distributions at 300K in a reservoir and in a supersonically expanded beam for argon.

velocity distribution (as shown in Fig.2.1), with higher mean velocity and much narrower velocity spread (means, lower translational temperature) than in the reservoir. This is a very elegant and general method to cool a gaseous ensemble, letting the high pressure gas (typically 1-5 atm.) freely expand (an adiabatic expansion) through a nozzle into a vacuum chamber. If we increase the pressure in the reservoir, it will lead to higher mean velocity of the beam. Above a critical reservoir pressure the particles are accelerated to a velocity equal to or higher than the local speed of sound, which is known as supersonic expansion regime.

2.2.1 Hydrodynamics and Thermodynamics

A schematic view of the hydrodynamics for a free jet expansion is shown in Fig.2.2. In the stagnation state (P_0, T_0), the gas starts from a negligibly small velocity. By imposing a pressure difference $(P_0 - P_b)$ the gas will be accelerated to the exit. When the expansion reaches supersonic regime, after the nozzle exit (see Fig.2.2), the gas does not respond to the boundary conditions (e.g., P_b, viscosity, heat capacity etc.) as it moves faster than the sound velocity. The background pressure inside the vacuum chamber is not zero and the expanding atoms push away the gases, which remain in the vacuum chamber. At a certain distance from the nozzle, a wall is formed which consists of congested atoms, known as the *Mach disk*. At this distance, numerous collisions occur between the atoms

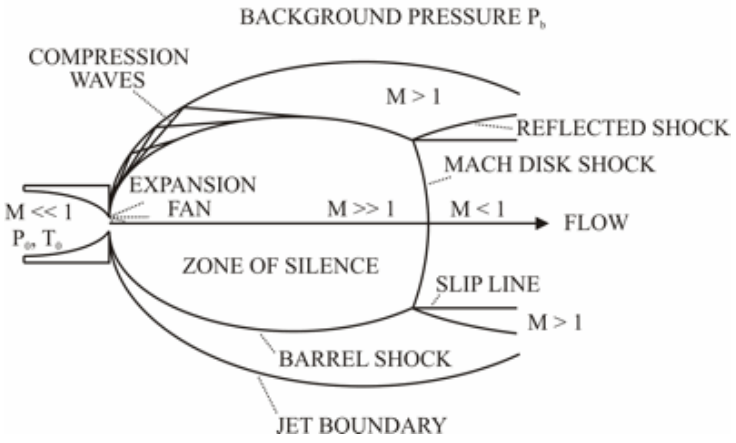

Figure 2.2: Continuous free jet expansion, adopted from [149]

and gases. In the space between the nozzle and the *Mach disk*, the number of collisions is very low and known as the *zone of silence*. Depending on the velocity of the beam, the dynamics of the flow can be characterized by Mach number ($M = V/V_{sound}$) which is defined as the ratio between the beam velocity and the velocity of the sound in the medium (for an ideal gas with molar mass M_g) $V_{sound} = \sqrt{\gamma RT/M_g}$. Inside the zone of silence **??**,

$$M = A\left(\frac{x}{d}\right)^{\gamma-1} - \frac{\frac{1}{2}\frac{\gamma+1}{\gamma-1}}{A\left(\frac{x}{d}\right)^{\gamma-1}} \cong A\left(\frac{x}{d}\right)^{\gamma-1} \tag{2.1}$$

where A is a constant (for noble gases such as He and Ar, $A = 3.26$ and $\gamma = 5/3$), d is the diameter of the nozzle, x is the distance from the nozzle and γ is the ratio of the specific heats at constant pressure and constant volume ($\gamma = C_p/C_v$). The Mach number M increases far from the nozzle in comparison to the diameter of the nozzle (i,e,. $x > d$) and however, eventually approaches a constant value as the number of collision reduces to zero by the expansion of the gas.

In the supersonic regime, the M becomes greater than one beyond the nozzle exit (see Fig.2.2). After the exit, the gas does not respond to the boundary conditions (e.g., P_b, viscosity, heat capacity etc.) as it moves faster than the sound velocity. But finally the shock wave, occurred in the process changes the supersonic flow and reduces the M, after the position of *Mach disk*. Once $M < 1$, the flow is able to adjust to the downstream boundary condition. With in the *zone of silence* the expansion is isoentropic and jet is free from the external boundary condition imposed by the ambient background pressure. By placing a skimmer in this region whose orifice is within the *zone of silence*, a beam of particles is extracted which is unaffected by the shock waves.

To understand the process let us consider an expansion where the expanding gas

is ideal with molar mass M_g and has a negligible viscous and heat conduction effect. Considering the energy conservation of the process, the first law of thermodynamics, the change in the enthalpy (h) per unit mass for such a free jet expansion is given by

$$\nabla h = V^2/2 = \int_T^{T_0} C_p dT \tag{2.2}$$

where ∇h is the change in total or stagnation enthalpy per unit mass before and after the expansion. V is the beam velocity. The temperature before and after the expansion are written as T_0 and T, respectively. After the supersonic expansion, the terminal velocity of the beam becomes,

$$V_0 = \sqrt{\frac{2RT_0}{M_g}\left(\frac{\gamma}{\gamma-1}\right)\left(1-\frac{T}{T_0}\right)} \tag{2.3}$$

where R, M_g are the universal gas constant, the molar mass of the gas respectively and $\gamma = C_p/C_v$, the specific heat ratio (C_p and C_v are the heat capacity at constant pressure and constant volume). Depending on the reservoir temperature and particle's mass, we can see that the typical beam velocities are on the order of a few hundreds to a few thousands meter per second.

For ideal gas mixtures we need to consider molar average heat capacity $\bar{C_p} = \sum X_i C_{p_i}$ and average molecular weight $\bar{M_g} = \sum X_i M_{g_i}$ where X_i is the mole fraction. Since the average kinetic energy of the mixture is characterize by $\bar{C_p}$ and T_0, each species can have different kinetic energy depending on their mass but have the same mean velocity in the continuum limit. In this way we can increase or decrease the mean velocity of the gaseous species by mixing it with lighter or heavier gaseous species in various proportions, respectively.

If we consider the $\bar{C_p}$ is constant within the temperature range, all the thermodynamic properties can be calculated with the following equations. The degree of cooling, defined as

$$\frac{T_0}{T} = \left(1 + (\gamma-1)M^2/2\right) \tag{2.4}$$

where M is the Mach number which is a property of the flow field (see Eqn.2.1), T_0 and T are the (translational) temperature in the nozzle and the jet, respectively. In order to cool the atoms requires high Mach number. For example, to cool the argon atoms from room temperature (e.g., 300K) to 3K, the Mach number should be ~ 20 which can be achieved at $x/d = 10$. For an isoentropic process the pressure and number density can be written in terms of temperature, as

$$\frac{P}{P_0} = \left(\frac{T}{T_0}\right)^{\gamma/\gamma-1} \tag{2.5}$$

and

$$\frac{n}{n_0} = \left(\frac{T}{T_0}\right)^{1/(1-\gamma)} \tag{2.6}$$

where T_0, P_0, n_0 and T, P, n are the temperature, the pressure and the density before and after the expansion.

We also can calculate the phase-space density A in the beam, is defined as

$$A = n\Lambda^3 = n_0 \left(\frac{T}{T_0}\right)^{1/(1-\gamma)} \left(\frac{2\pi\hbar^2}{mkT}\right)^{3/2} \tag{2.7}$$

where $\Lambda = (2\pi\hbar^2/mkT)^{1/2}$ is the thermal de Broglie wavelength. A is also know as degeneracy parameter of the gas. In our case, the Λ is much smaller than the inter-particle distance and the gas can be considered as a classical or Maxwell-Boltzmann gas.

Now, let us consider the velocity distribution in a supersonically expanded beam. At some distance from the nozzle of the valve, the collision rate of the particles drops as the gas expand and jet become collision free. The thermodynamic properties of the gas stop evolving and the temperature and the velocity of the gas is set. The particles in a given volume element at a larger distance from the nozzle, have smaller velocity component along the streamline and the perpendicular velocity distribution decreases with increasing distance. While, the parallel (longitudinal) velocity components stays unaffected [150]. So, the velocity distribution far from the valve can be expressed by neglecting the perpendicular components and it becomes,

$$P_v(v_z) = \frac{1}{\delta v_z\sqrt{2\pi}}\ exp\left(-\frac{(v_z - v_{z0})^2}{2(\delta v_z)^2}\right) \tag{2.8}$$

where v_{z0} is the mean velocity of the beam along z (which is the beam axis) and $\delta v_z = \sqrt{kT_z/m}$ where T_z, k and m are the longitudinal temperature in Kelvin, Boltzmann's constant and mass of the particle, respectively. If a pulsed beam produced by pulsing the valve for an infinitesimally small time, a detector located at L downstream from the valve exit will record the corresponding time-of-flight (TOF) distribution,

$$P_v(t) = \frac{L}{\delta v_z\sqrt{2\pi}}\frac{1}{t^2}\ exp\left(-\frac{(v_{z0}t - L)^2}{2(\delta v_z)^2 t^2}\right) \tag{2.9}$$

When the $\delta v_z \ll v_{z0}$ in a beam $P_v(t)$ results in a Gaussian time-of-flight profile and the time corresponds to the most probable arrival becomes equal to L/v_0. We shall see that this TOF distribution describes the experimental data reasonably well, Fig.2.15.

2.3 General Presentation of the Supersonic Beam-Machine

Since we have started from scratch, our first goal was to find previously used chambers, modify them according to our design, needs and finally assemble them together and make it working.

The first step has been to build a vacuum chamber for the production of the molecular beam which we call the source-chamber. The second step has been to build another vacuum chamber which contains the device for the detection, we call it the experimental-chamber. Finally, the third step has been to connect these two chambers all together with a long narrow glass-tube. This narrow-tube section is the heart of our experiment and is dedicated to the deceleration and guiding of the supersonic beam. The realization of the magnetic coils for guiding and deceleration in the Laboratory are also another important step for our experiment, shall be described in the next chapters.

The Fig.2.3 shows the experimental set-up which consists of mainly three sections. First, the source chamber to produce the atomic and molecular beam. Second, a $43cm$ long narrow glass-tube connecting two chambers and finally the detection chamber with detection device.

The source-chamber and the experimental-chamber are pumped respectively by *OSAKA* (model: TG600M, capacity $620l/s$) and *Pfeiffer* (model: TPU520, capacity $520l/s$) molecular turbo pump. Both the chambers are primarily pumped by one root pump *Busch* (capacity $30m^3/h$), which alone assures a vacuum $5\times10^{-2}mbar$ in both the chambers. The *OSAKA* is a magnetic-suspended (hence oil free) compound molecular turbo pump which is compatible for radicals and other corrosive gases. The vacuum inside the chambers are measured by *Pfeiffer compact full range gauge* (Type: PKR251). When all the pumps are running, the vacuum in side the source-chamber and the experimental-chamber are $10^{-7}mbar$ and $5\times10^{-8}mbar$, respectively. The narrow glass-tube section is differentially pumped by two turbo pumps attached with the source and experimental-chamber. We do not know the real quality of the vacuum in this part.

The source chamber contains an input gas-line to the valve. The valve is suspended by a triangular plate which is firmly held with the source-chamber, makes sure the precise position and the direction of the valve (see Fig.2.4). A $Liq.N_2$ cooling chamber is installed around the valve to cool the valve at an user defined temperature (typically to $\sim 160K$). Two thermocouples (Pt100) are introduce to measure the temperature on the valve and the $Liq.N_2$ chamber. After the valve ends, there comes discharge electrodes and a filament to produce metastable beam. A 2mm diameter skimmer is placed $\sim 2cm$ down-stream after the end of the discharge apparatus (see Fig.2.4).

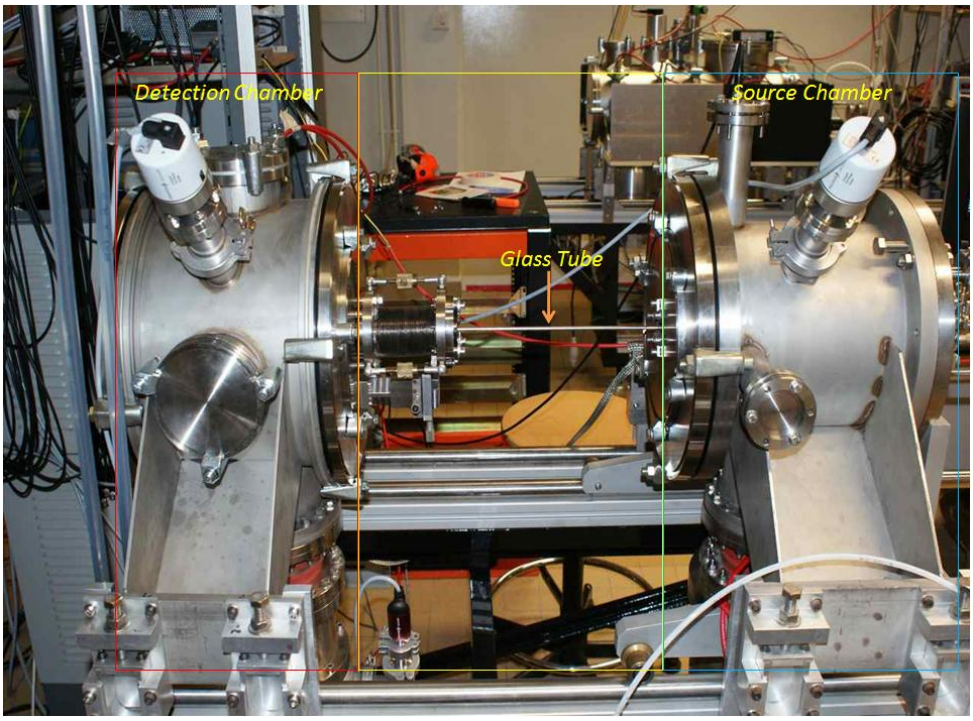

Figure 2.3: Picture of the experimental set-up without the magnetic coils. The beam direction is from right to the left. The chamber on the right is the source-chamber containing all the devices for supersonic expansion (e.g., supersonic valve, $Liq.N_2$ cooling chamber for the valve, discharge electrodes, filament to stabilize the discharge, skimmer etc.) and the experimental-chamber containing detection device, MCP (Micro-Channel-Plate), is on the left. And these two chambers are connected by a long-narrow glass tube, which is dedicated to the guiding and the deceleration of the beam.

After the skimmer the glass-tube section starts (see Fig.2.4). A 43cm long glass tube connects the source-chamber and the experimental chamber. To align the glass tube with the skimmer direction we have mounted the end of the glass tube on a bellow which is again mounted on a mm-screw attached with the experimental chamber.

For the control, the automation and the synchronization of the various components of the experiment, we use TTL signals. The TTL signals are generated by a computer which is using *National Instrument NI PCIe-6537* card. The card is being controlled by *LabView* program. It is able to produce a TTL pulse with an user defined on-time and off-time, independently to other TTL pulses. It provides all the time sequences and their synchronization for various components of the experiments, like valve, electric discharge, guiding and deceleration electronics. The LabView program is also used for data acquisition from a *Lecroy WaveRunner 42Xs* digital oscilloscope.

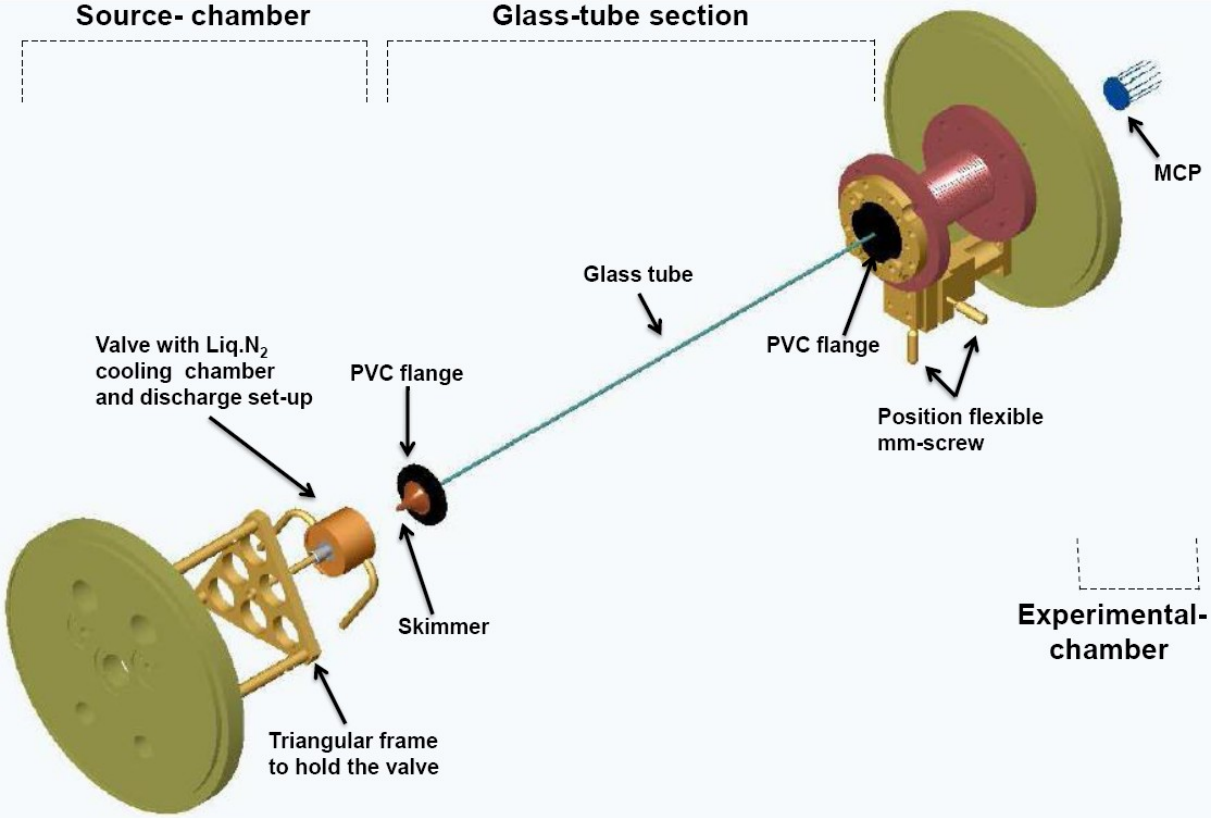

Figure 2.4: The schematics of the hole supersonic beam set-up with detection apparatus. Metastable beam-pulse is produced by electric glow discharge at the exit of the valve. After, the beam passes through skimmer, then the glass tube and finally to the detector. The time-of-flight (TOF) distribution of the metastable beam over 57cm flight from the valve to MCP detector is measured when the metastable beam-pulse strikes on the MCP wall.

2.4 Realization of Supersonic Expansion

The supersonic expansion is carried out by letting the gas pass through a small orifice from a high pressure reservoir to the vacuum. We use a solenoid valve with a $1mm$ orifice diameter which operates in pulsed mode.

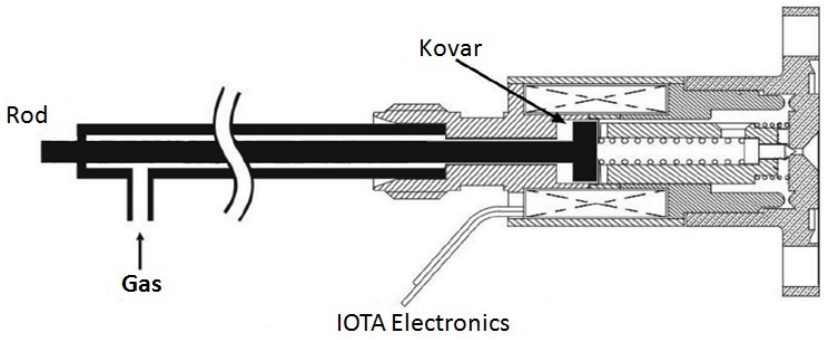

Figure 2.5: Schematic of a modified pulsed valve, adopted from [151]

The model of the valve we are using is $Parker - General\ Valve$, series 9. This valve has been modified to adopt the range of temperature we work with, especially for $Liq.\ N_2$ temperature. The modification of the valve is shown in the Fig.2.5. A micro-meter screw is connected to the interior of the valve through the gas-line by thin non-magnetic stainless-steel rod. One end of the rod is attached with a circular non-magnetic stainless-steel plate which is situated inside the valve and the other end with the micro-meter screw. It is used to change and control the movement of the poppet inside the valve, which is very important at low temperature. The stagnation pressure is typically $2bar - 4bar$. The repetition rate of the experiment is typically 1 Hz which rises the pressure inside the source chamber to $\sim 5 \times 10^{-6} mbar$ while the vacuum inside the experimental-chamber hardly changes. The valve is operated and controlled by $IOTA\ one$ electronic driver and it can produce $\sim 180\mu s$ long gas pulse at room temperature (at lower temperature it can produce even shorter pulses $\sim 150\mu s$). The valve is actively cooled by $Liq.N_2$. The $Liq.N_2$ is flown, in a controlled way, to a small chamber which encases the valve. To make a good thermal connection between the surfaces of $Liq.N_2$ chamber and the valve we use a low-temperature, high-vacuum compatible thermally conducting grease ($Apiezon\ N$). To have control in the flow of $Liq.N_2$ we use a storage bottle ($AIR\ LIQUID,\ model\ TP100$), able to flow a constant flux of $Liq.N_2$ by self-pressurizing (typically $0.4bar$ inside the bottle) itself. The temperature is measured using Platinum-based thermo-couple (model $Pt100$). To control the temperature of the valve, which finally determines the mean velocity and velocity spread of the beam, we use a temperature controller ($STATOP$). It controls the temperature by a PID (Proportional Integral Derivative) loop, consisting of a $Liq.N_2$ chamber, valve and an adjustable heater (resistors), where the heater is placed

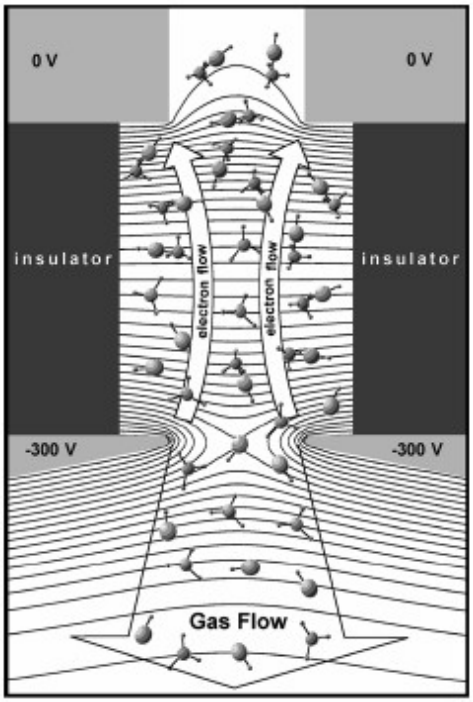

Figure 2.6: Schematic of an electric glow discharge[153]

at the entrance of the $Liq.N_2$ line. When the beam is operational, the temperature on the valve-body is typically $158K$ and on $Liq.N_2$ chamber is $88K$. Then the gas is passed to the electrodes for the discharge, which comes right after the exit of the valve. The supersonic expansion is taken place at the exit of the discharge set-up.

2.5 Producing Metastable He and Ar Atoms

The gas discharge is one of the powerful methods to prepare a metastable quantum state of atoms and molecules. All types of gas discharges can be classified into two major groups, DC discharge and RF/Microwave discharge. An excellent study of all kinds of gas discharge physics is given in [152].

The fundamental processes involved in DC discharge includes ionization of atoms by electron impact, motions of charged particles in electric field, charge multiplication in electron avalanche (which is the fundamental element of the plasma breakdown process) and finally, secondary electron production at the cathode. A typical scheme for a DC discharge is shown in Fig.2.6.

In electron avalanche processes, the electrons drifts in an electric field towards the anode and gain kinetic energy from this field and cause ionization of atoms by collisions. This results in a fast multiplication of ions and electrons. The electron avalanches do

	He	Ne	Ar	Xe	N_2	H_2
Electron mean free path (m.Torr.cm), typical for 1-10 eV electrons[152]	60	120	30		30	20
Ionization coefficient (cm^{-1}), for $E/p = 10V/(cm.Torr)$ [152]	50	50	5			
Secondary emission yield, from tungsten/platinum cathode [152].	0.21	0.30	0.09	0.02	0.005	0.003
Breakdown voltage (kV) at $p.d = 100Torr.cm$	1.5	0.8	1.5		6.3	4

Table 2.1: Glow discharge properties for various gases.

not evolve only in time, but also in space along the direction of the electric field. The ionization coefficient, α, which is the number of ionization events by electron impact per unit length along the electric field direction is

$$\alpha/p = A\ exp(Bp/E) \tag{2.10}$$

where p is the pressure, E/p is the reduced field strength and A, B are the gas-specific constants, derived from experiments. The ionization coefficient for various gases are given in Table.2.1.

The secondary electron emission can occur through several processes [154]. First, thermionic emission, due to high temperature heating of the electrode. Second, field emission, electron release due to strong electric field gradient near to the electrode. Finally, electron emission due to particle (i.e. positive ions, excited atoms, electrons and photons) impact on the electrode surface. For most low-pressure gas discharges, particle-impact electron emission (by Auger processes) is the dominant secondary emission mechanism. For a given electron, that starts at the cathode will cause an electron avalanche towards the anode which again produces ions by ionizing atoms through electron-impact collisions. The produced electrons in this ionization process leave the ions behind the discharge gap, as the electrons are much faster than the ions. By this way the number of secondary electrons are increased.

The density of the metastable atoms can be calculated [155] by considering various production and loss processes involved in the discharge. The main production processes incorporate (i) fast-electron-impact excitation from ground state atoms, (ii) fast-ion and fast-atom impact excitation from ground state atoms, and (iii) radiative recombination between anions and slow electrons. The main loss processes include (i) fast-electron-impact ionization from the metastable levels, (ii) fast-electron-impact excitation from the metastable level to higher energy levels, (iii) population transfer to the nearby reso-

nant level by thermalized electron collisions, which is known as electron quenching, (iv) metastable-atom-metastable-atom collisions, resulting in ionization of one of the atoms, (v) Penning ionization of sputtered atoms from the cathode, and (vi) two-body and three-body collisions with ground state atoms. For a discharge cell with 1.5cm long and infinitely wide with molybdenum cathode at 75Pa argon pressure and 850V discharge voltage, the metastable argon density varies between $2 \times 10^{10} cm^{-3}$ to $5 \times 10^{13} cm^{-3}$ [155].

The operation of glow discharge plasmas with microsecond or millisecond duration pulsed power affords many advantages over steady-state operation [156, 157]. It enables higher instantaneous power to be used, which results, in increased sputtering, excitation and ionization in the process. A plasma produced during the discharge is said to be in state of thermodynamic equilibrium if every process which occurs in plasma, is fully reversible. However, pulsed glow discharges do not show this thermodynamic equilibrium[158], as the proper forward and reverse reactions do not always balance each other. That can occur for many different reasons, for example, when the voltage is removed from a glow discharged plasma, the electrons produced are no longer accelerated by the electric field, resulting a thermalization in the high-energy electrons. They can recombine with the ions and produce highly excited neutral states. If the ions recombine and diffuse from the discharge region it initially disrupt the Saha balance (i.e., the degree of ionization) which describes the balance between electron ionization of excited atom's states by fast electrons and three body recombination of ions with two thermal electrons. The shorter pulse width of pulsed glow discharge makes the plasma even further from the thermodynamic equilibrium conditions.

2.5.1 Realization and Stabilization of the Discharge

The production of metastable helium and argon atoms have been performed in the laboratory by discharging the pulsed supersonic beams of the respective gases. Argon atoms have two metastable levels, i.e., the $(3p^5 4s)\ ^3P_2$ level and the $(3p^5 4s)\ ^3P_0$ level at 11.55eV and 11.72eV above the ground state respectively. Also two resonant levels are laying closely to the metastable levels, i.e., the $(3p^5 4s)\ ^3P_1$ level and the $(3p^5 4s)\ ^1P_1$ level at 11.62eV and 11.83eV above the ground state, respectively. These state can decay to the ground state by radiative emission. For Helium atom, the metastable state i.e., the $(1s2s)\ ^3S$ is at 19.8eV above the ground state.

The discharge has been carried out by placing two electrodes at the exit of the valve (see Fig.2.7). So, the discharge takes place just before the supersonic expansion. We use stainless-steel electrodes with $1mm$ diameter orifice, separated by $1.6mm$ thick teflon spacer with 1mm diameter pinhole at the center. Typical back ground pressures are $2bar - 3bar$ for He and Ar gases. The typical discharge voltage for Helium and Argon

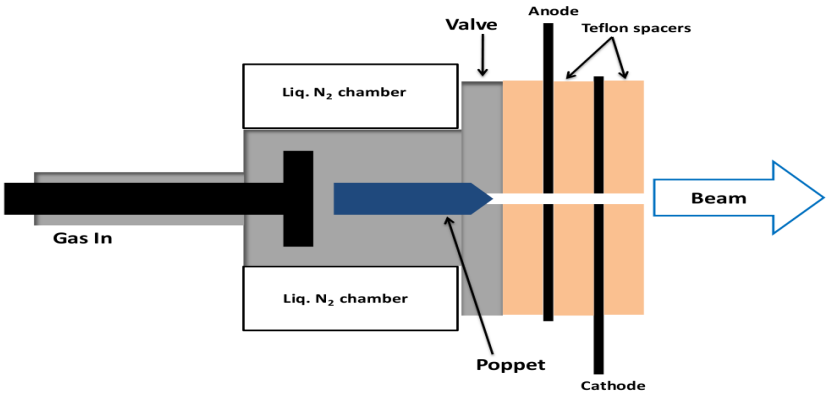

Figure 2.7: Schematic of our discharge set-up. Two stainless steel electrodes (cathode and anode in the figure) with a pinhole of diameter 1mm, are placed right after the exit of the valve. The electric glow discharge is carried out by passing the gas through the electrodes. The typical voltage difference between the electrodes is $1kV$. Each electrodes are separated by $1.6mm$ thick teflon spacers with the 1mm diameter pinhole at the center. The supersonic expansion takes place at the exit of the discharge set-up.

are 1250V and 850V, respectively. We have found that, the intensity of the metastable argon beam is more at low valve temperature than at room temperature which can be explained as the beam intensity is more at lower temperature. We also have noticed that DC discharge for helium is more stable than the DC discharge for argon. This can be explained as the secondary electron production for helium discharge is more than argon discharge (see Table2.1). As expected, we have noticed that a continuous DC discharge of a pulsed supersonic beam increases the mean velocity and the velocity spread of the metastable beam than a pulsed DC discharge. To produce a beam with low mean velocity and velocity spread it is necessary to cool down the valve and perform pulsed DC discharge, that is what we do in our experiment.

A high-voltage electric pulse is generated (see Fig.2.8) using high-voltage switch (*BEHLKE*). The *BEHLKE* is triggered by TTL generated using National Instruments (NI) card. As we have already discussed the discharge processes depend not only on time but also in space, it is hard to realize a self-sustained discharge for pulsed beam as its particle density varies both in space and time. It disturbs the steady-state electron emission processes. Again a short, pulsed discharge (typically $10\mu s - 20\mu s$) to produce shorter metastable beam packet makes it even more difficult achieving a stable discharge.

As we mentioned before the stability of a discharge can be gained by achieving a steady-sate secondary electron emission between the discharge electrodes. Since it is a pulsed discharge process, we never can reach a steady-state process but some tricks can

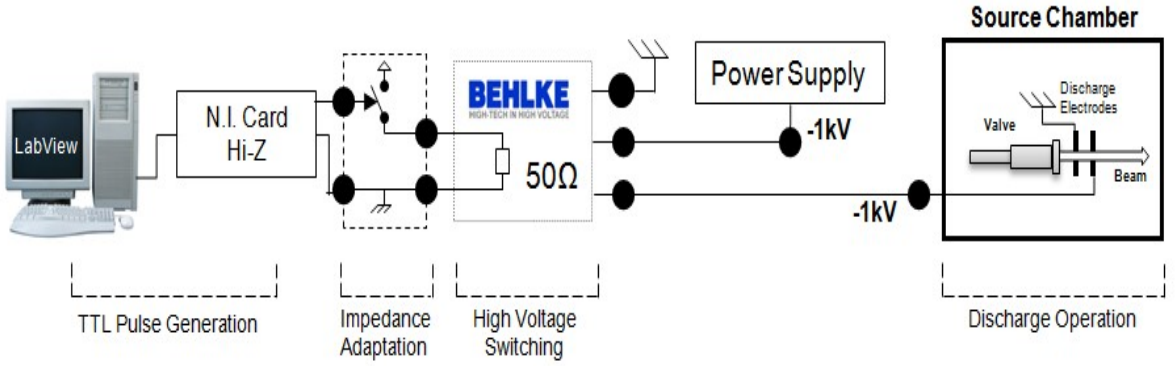

Figure 2.8: The scheme for the pulsed electric glow discharge. A TTL pulse is generated by the NI-card, triggers the *BEHLKE* to produce a short high-voltage pulse and finally, is applied to the cathode mounted at the exit of the valve for discharge.

be used to achieve a quasi-steady-state discharge process. Here we mention the tricks we use to optimize the argon discharge in our experiment.

a) We have noticed that, the installation of an electron emitting filament near the discharge electrodes helps to stabilize the discharge process. As it provides an additional electron-current between the electrodes which helps to initiate the ignition process at the beginning and then, stabilizes the process by supplying additional electrons.

b) Increment in the discharge voltage between the electrodes can also stabilize the discharge process by helping the production of more secondary electron emission and accelerate them between the electrode. But on the other hand it increases the mean velocity and the velocity spread of the beam, which we have observed in the experiment.

c) The effect of the back-ground pressure of argon also plays a crucial role. As, with increasing the back ground pressure we can have more number of particles which also increases the number of secondary electrons and stabilizes the electron avalanches. We have noticed that, after reaching certain back-ground pressure a further increase in pressure does not changes the discharge process so much.

d) The implementation of multiple valve pulses in each valve pulse-sequence instead of only one valve pulse, dramatically stabilizes the discharge process which has been observed in our experiment. While, one of the pulses is pulsed discharged and others are continuous DC discharged (see Fig.2.9). That reduces the discontinuities in the secondary electron production and makes sure of the presence of some electrons even after the first pulsed discharge process finishes, which helps to initialize the subsequent

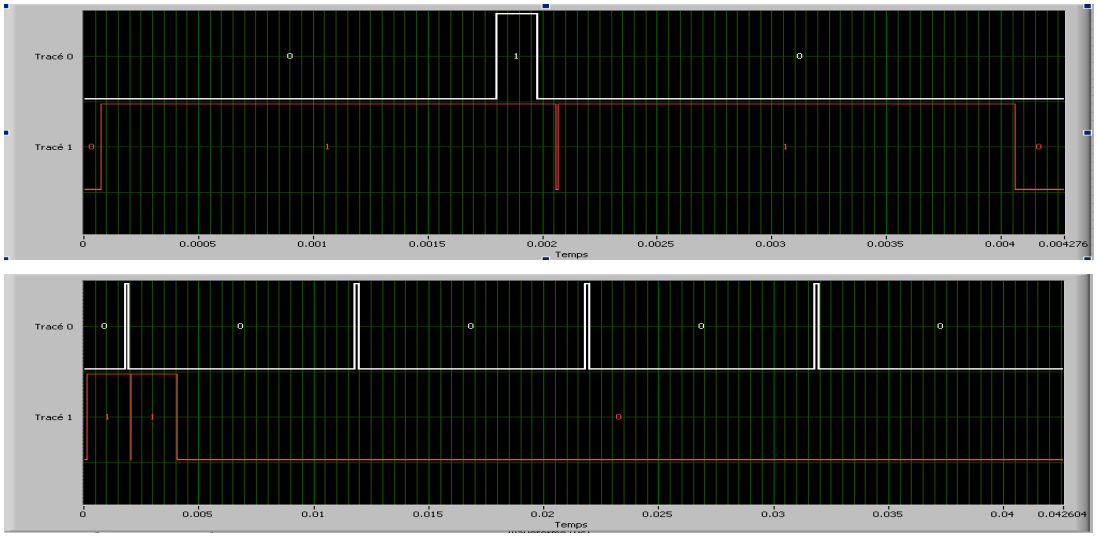

Figure 2.9: A typical pulse sequence for a stable discharge. The white traces and the red traces represent the pulse sequence for valve and discharge voltage. The upper-level of the white traces corresponds to opening time of the valve. The **upper-figure** shows a pulsed voltage DC glow discharge where the upper-level of the red trace corresponds to $0V$ and the lower-level corresponds to $\sim -1000V$. It is important to notice that, we apply the discharge pulse $\sim 70\mu s$ later than the end of the valve pulse. The reason behind it is that, the mechanical constraint in the valve which not only makes a delay to begin the beam pulse but also changes the position distribution profile of the pulse. The **lower-figure** shows a discharge with multiple valve pulses in one valve-pulse sequence. In this case, the first valve-pulse is pulsed DC discharged while the others are continuous DC discharged.

pulsed discharge process, going to take place in the next valve pulse-sequence.

The statistics (see fig.2.10) of successful discharges has been carried out at room temperature with respect to various backing pressures, various discharge voltages and various currents from the filament. The stability of the discharge is better with more filament current, indicates the achievement of steady secondary electron emission process with additional electrons provided by the filament. The increment in argon back pressure stabilizes the discharge process, at the same time it increases the metastable argon atom density as indicated from the MCP signal. With using more discharge voltage between the electrodes we also can stabilize the discharge process because of more secondary electron production but at the same time it increases the mean velocity and the velocity spread of the beam. By increasing the number of valve pulses in a valve pulse-sequence, the discharge process gets stabilized. But, on the other hand it pollutes the glass-tube with more number of pulses, which is only differentially pumped by two chambers.

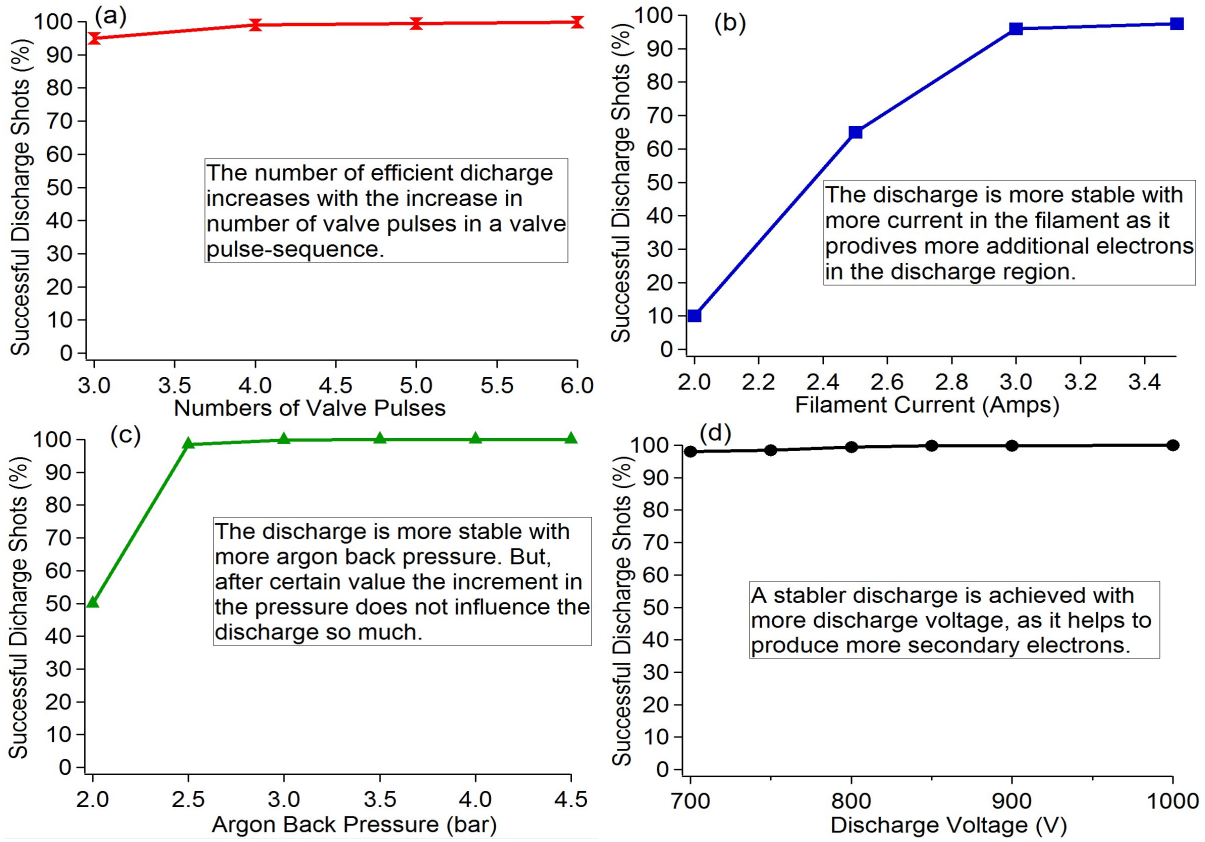

Figure 2.10: Statistics of successful discharge has been done experimentally at room temperature with various discharge conditions like, number of valve pulses, various filament currents, various back-pressures of argon and various discharge voltages. For convenience, the points are joined with straight line in the figures.

Fig.2.10 shows the statistics we have carried out with various number of valve pulses, various filament currents, various back-pressures of argon and various discharge voltages. In each case we use $170\mu s$ long valve pulse, $30\mu s$ long discharge pulse with $750V$ voltage difference between the electrodes (except for the case where we have done the statistics with respect to various voltages). The Fig.2.10(a) shows the number of successful discharges per 1000 valve pulse-sequence with respect to various numbers of valve pulses in each pulse-sequence with $1Hz$ repetition rate, $3bar$ argon back-pressure and filament current $3Amps$. In this scan, we use the time separation between the valve pulses in such a way that the total time duration of the pulse sequence is $\sim 600ms$. The Fig.2.10(b) shows the number of successful discharges per 1000 valve pulse-sequence with respect to various filament current with 2 valve-pulses in each shot, $1Hz$ repetition rate, $3bar$ argon back-pressure. The Fig.2.10(c) shows the number of successful discharges per 1000 valve pulse-sequence with respect to various argon back-pressures with 3 valve-pulses in each sequence, $2Hz$ repetition rate and $3Amps$ filament current. The Fig.2.10(d) shows

the number of successful discharges per 1000 valve pulse-sequence with respect to various discharge voltage between the electrodes with 3 valve-pulses in each sequence, $2Hz$ repetition rate, $3bar$ argon back-pressure.

2.6 Glass Tube Section

After the production of the metastable beam pulse, it enters the glass-tube section (see Fig.2.4), dedicated to the magnetic coils for guiding and deceleration, which begins right after the skimmer. The inner and outer diameters of 43cm long narrow glass-tube are 1.2mm and 3mm, respectively. The glass-tube is differentially pumped by both the source and experimental-chamber. The flanges holding the glass-tube is made up of PVC plastic material and nonmagnetic-steel since, this section is dedicated to the magnetic coils and a rapid switching in the driven current is necessary, as we shall see in the next chapters.

This is the most important section in our experiment. At the same time, it is very difficult to get a beam through it because of three reasons. First, the particles are crashed on the way to the detector, on the tube's wall due to non-zero transverse velocity of the beam, which finally reduces the intensity of the beam. We also have noticed the number of particles arrive at the detector decrease with the increase in length of the glass tube. But, addition of a quadrupole guide reduces this effect, we shall see that in the next chapter. Second, the alignment of the skimmer, glass-tube and the detector, which is very often not perfectly aligned as the glass tube itself can be bent. Since the position and direction of the skimmer defines the direction of the beam, it is very important to align the glass-tube with the skimmer. For that, the end of the long glass-tube is mounted on a mm-screwed position flexible flange (see Fig.2.4) and the glass tube is encased with a long, straight holder, generally the guiding and the deceleration magnetic coils plays the role of the holder. It ensures the arrival of the beam to the detector (in the experimental chamber) in a straight line. Third, the glass tube is differentially pumped by two chambers connected to it and the chambers are pumped by the turbo-molecular pumps. The pumping is not very efficient when the repetition rate of the experiment goes high. That is why we work with maximum 2Hz repetition rate.

2.7 Detection

The principle of the detection is based on the electron emission and their multiplication when an excited particle or a positive ion strikes the surface of the MCP as indicated in Fig.2.11. The plates are made up of many channels (diameter $\sim 10\mu m$). If a potential gradient is established along the channel, multiple secondary electrons are emitted, when

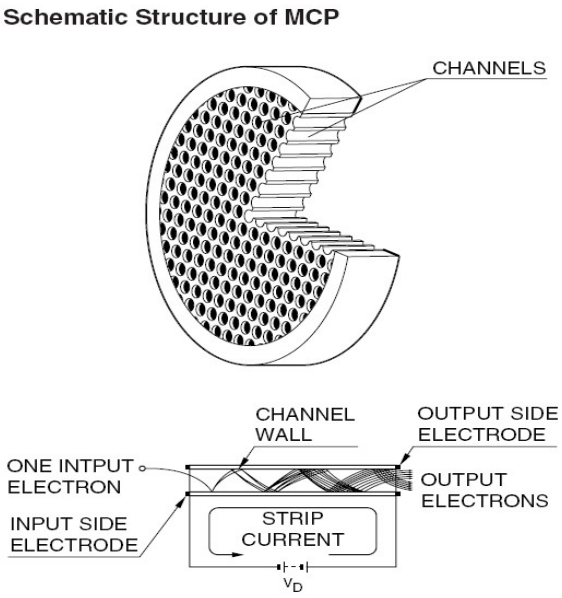

Figure 2.11: Schematic of the MCP plate and the way it multiplies the number of electron when an electron enters at the input of a channel. The figure is adopted from *HAMAMATSU PHOTONICS*.

an electron enters a channel from the input side and strikes its inner wall. These secondary electron gets accelerated due to the potential gradient and strike the opposite wall again, due to its parabolic trajectory. That further produces secondary electrons. This process continues and repeats until the output of the channel. As a result, a large number of exponentially increased electrons are extracted from the output side and collected at the anode.

We use home-build two stage micro-channel-plate (MCP) as our detector. The MCP ($HAMAMATSU,\ F1552-074$) plate we are using is of $0.3mm$ thickness and $7.5\mu m$ channel-diameter. The schematics of our MCP-assembly is shown in Fig.2.12.

The voltage difference between two MCP plates is 2kV. The electrons, produced after a positive ion or an excited atom, are collected with anode and the anode is connected to the oscilloscope which finally records the informations regarding particles arrival to the MCP. The typical TOF-signal we receive from the MCP detector looks like as shown in Fig.2.12. The first peak of the TOF-signal (see Fig.2.12) corresponds to the photon signal generated in the discharge process and the second one corresponds to metastable atoms. The photon signal indicates the beginning of the discharge which can also be considered as the time, when the atoms start their flight.

We already have noticed in the previous section, the pulsed electric glow discharge is not stable in each repetition of the experiment. Because of that we trigger our other experimental components like magnetic guiding and deceleration as these are effective

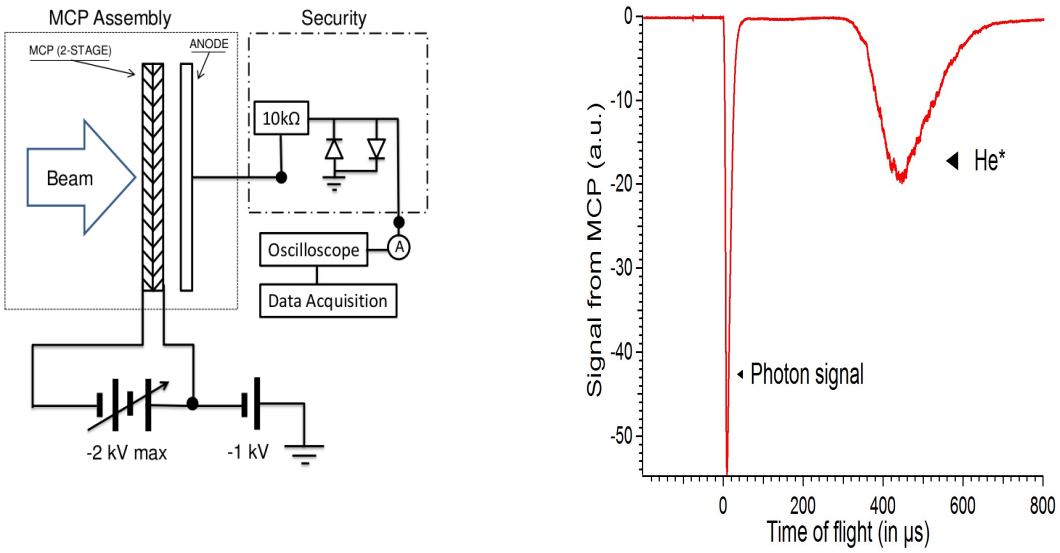

Figure 2.12: (Left) Schematic of an MCP-assembly for positive ions and excited particles. (Right) A typical signal from MCP indicating the time of arrival of He beam at $Liq.N_2$ cooled temperature.

only if there is an efficient discharge to produce a nice metastable beam, depending on the photon-signal form the MCP. A scheme of the triggering set-up for the guiding and the deceleration electronics is shown in Fig.2.13. It compares the signal amplitude (in mV) from the MCP with respect to a user defined amplitude and act as a gate.

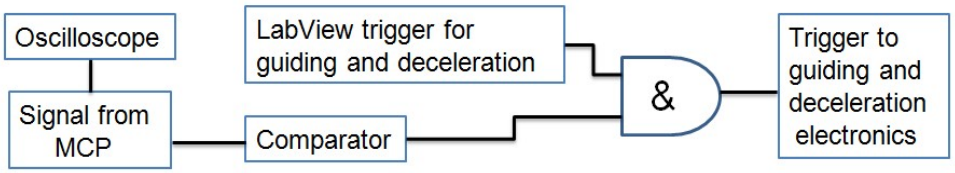

Figure 2.13: Schematic for triggering of guiding and deceleration electronics.

If the photon-signal is more than a certain voltage (e.g., 50mV for Ar beam, which is enough to confirm an efficient discharge), then only the other components of the experiment are triggered. More details can be found in [159].

2.8 Experimental Results

In the experiment supersonic beams of metastable helium (He^*) and metastable argon (Ar^*) are produced. The typical length of valve pulse used for both the beam is $\sim 180\mu s$ and duration of the discharge pulse of $10 - 15\mu s$. For the He^* and Ar^* beams, the

discharge voltage used are 1200V and 850V. The observed experimental signals shows that the mean velocity and the velocity spread can be reduced by cooling down the valve by $Liq.N_2$ cooling, which is presented in Fig.2.14

The mean velocity and the longitudinal velocity spread are calculated from the TOF profiles by fitting with the function,

$$p(t) = N + \frac{B}{t^2} Exp\left(-\frac{(t-t_0)^2}{2W^2t^2}\right) \tag{2.11}$$

where L is the distance traveled by the atoms which is 57cm. The adjustable parameters of the fit are the background N, the peak height B and the width W. The mean velocity is $v_{z0} = L/t_0$ and the longitudinal temperature T_z, by the comparing with the Eqn.2.9 becomes,

$$T_z = \frac{mW^2L^2}{kt_0^2} \tag{2.12}$$

where m and k are the mass of the atom and Boltzmann constant.

In the Fig.2.15 the fitting is shown for the observed experimental TOF signal of metastable helium beam at room temperature. The found mean velocity, velocity spread and the longitudinal temperature are $1900m/s$, $210m/s$ and $20.5K$, respectively.

Gas	Valve temperature	Discharge voltage	Discharge pulse	Mean velocity	Longitudinal velocity spread	Longitudinal temperature
He^*	300K	1200V	15 μs	1900m/s	210m/s	20.5K
He^*	158K	1200V	15 μs	1220m/s	165m/s	13K
Ar^*	300K	850V	10 μs	714m/s	115m/s	64K
Ar^*	158K	850V	12 μs	471m/s	47m/s	10.5K

Table 2.2: The characteristics of He^* and Ar^* beam in the experiment.

The experiments have been performed to produce He^* and Ar^* beam in both room temperature and $Liq.N_2$ and the result are summarized in Table.2.2. For metastable helium beam at room temperature (300K) the mean velocity and velocity spread are 1900m/s and 210m/s, respectively corresponds to 20.5K longitudinal temperature. At $Liq.N_2$ cooled temperature the mean velocity and the velocity spread are 1220m/s and 165m/s, respectively, corresponds to 13K longitudinal temperature. While for metastable Ar beam at room temperature, the mean velocity and the longitudinal velocity spread are 714m/s and 115m/s corresponds to 64K. For $Liq.N_2$ cooled metastable Ar beam, the mean velocity and longitudinal velocity spread are 471m/s and 47m/s, which corresponds to 10.5K.

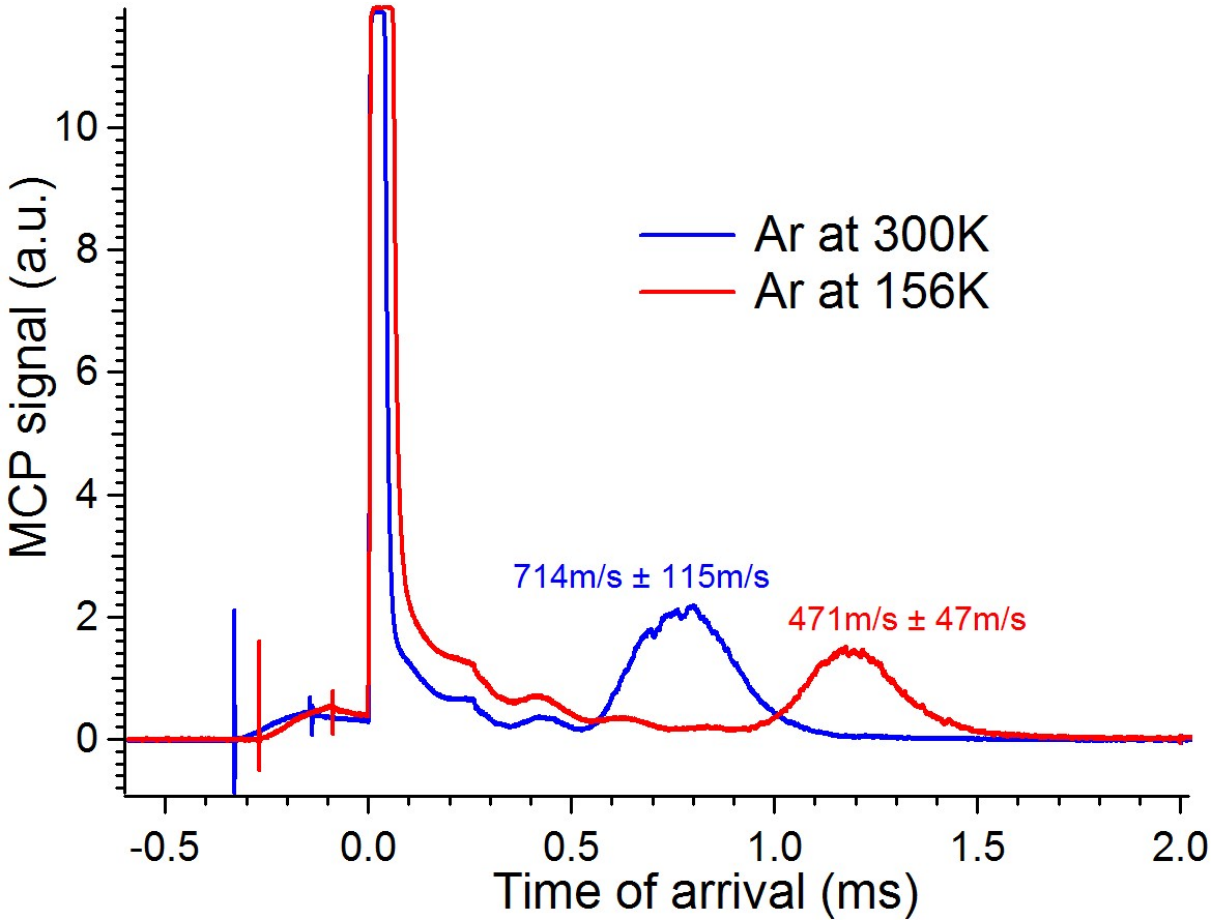

Figure 2.14: The observed experimental signals for Ar^* beam at room temperature (300K) with $10\mu s$ and 850V discharge pulse (shown in blue) and at $Liq.N_2$ cooled temperature (158K) with $12\mu s$ and 850V discharge pulse (shown in red). The beginning of pulsed discharge is indicated by a huge photon-signal from MCP. The effect of $Liq.N_2$ cooling is pronounced as we can see from the signal, indicated (*mean velocity* $\pm$ *velocity spread*) with the mean velocities and the velocity spreads. The longitudinal temperatures of the beam with the valve temperature of 300K and of 158K are 64K and 10.5K, respectively.

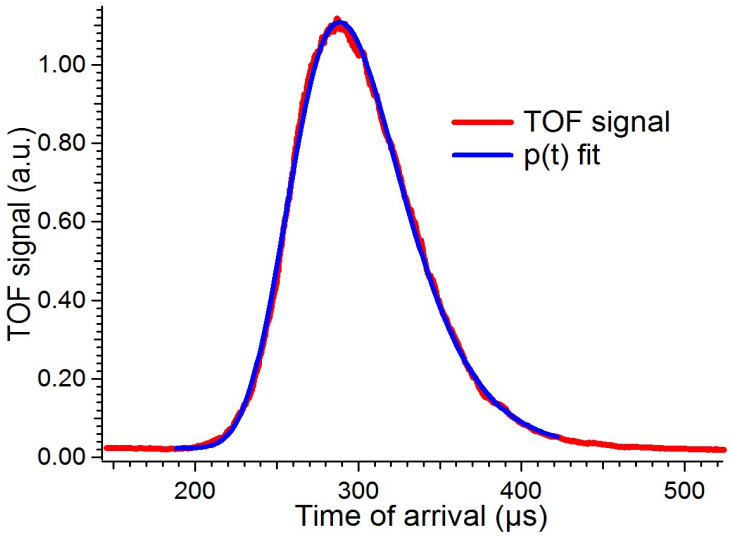

Figure 2.15: The TOF distribution of metastable He (He^*) beam at room temperature (300K) with 180μs long valve pulse and 15μs long and 1200V discharge pulse. The observed experimental signal is shown in red trace and the blue trace represents the fitting using the Eqn.2.11 with the parameter $L = 57cm$. The mean velocity and the longitudinal velocity spread of the beam are $1900m/s$ *and* $210 \pm 0.1m/s$, respectively which corresponds to a longitudinal temperature of $20.5K$.

The production of metastable atom is based on electric glow discharge, which is a heating process and that occurs just after the exit of the supersonic valve. So, the temperature of the valve solely does not determine the mean velocity and the spread in velocity of the beam. We must have to consider the heating processes during the course of discharge, which is quite complicated to modelize. We always find, the velocities of the beam higher than expected at measured valve temperature. At 300K,the terminal velocity of Ar-beam after the supersonic expansion, is 560m/s, theoretically. But the experimental result for room temperature and $Liq.N_2$ cooled metastable argon beam indicates the reservoir temperature (following Eqn.2.3) to be 490K and 213.5K, respectively. The reservoir temperature at room temperature and $Liq.N_2$ cooled metastable He beam, as indicated by the mean velocities are to be 347.4K and 143K, respectively.

2.9 Conclusion

In this chapter we have described our supersonic beam machine and its working principles. We made an emphasis on the importance of supersonic beams and how it can be a tool to cool down a thermal ensemble. In our experiment, we have realized supersonic metastable helium and argon beams. We have demonstrated experimentally the stabilization of

pulsed electronic DC glow discharge and the detection of metastable argon and helium beams. We also, have introduced pre-cooling of the supersonic valve to produce even colder beams with lower mean velocity and narrower velocity spread. We have produced a metastable argon beam which has the characteristics of 471m/s mean velocity with longitudinal temperature 10.5K and a metastable helium beam of 1220m/s mean velocity with longitudinal temperature 13K. Finally, a dense, cold metastable beam of argon is realized with lower mean velocity, which is a good starting point for magnetic guiding and deceleration experiment.

Chapter 3

Zeeman Guiding of Paramagnetic Atoms

Man is slightly nearer to the atom than to the star. ... From his central position man can survey the grandest works of Nature with the astronomer, or the minutest works with the physicist. ... [K]nowledge of the stars leads through the atom; and important knowledge of the atom has been reached through the stars. — Sir Arthur Stanley Eddington

3.1 Introduction

The concept of manipulation and control over the motions of neutral particles with electric and magnetic fields have been started since the emergence of the idea of space quantization. The quantization of angular momentum was proposed by Debye and Sommerfeld in order to explain the spectrum of hydrogen atom. This concept of space quantization primarily was not seriously considered by the physics community rather it was regarded as a purely mathematical description, as it did not manage to establish a rational explanation based on classical mechanics until 1922.

In the year 1921, an experiment was proposed by Otto Stern which can test the space quantization [160]. The experiment (see Fig.3.1) which is known as Stern-Gerlach experiment, was performed in 1922 based on deflection of particles [161] and confirmed the concept of space quantization as a consequence of particles intrinsic properties, the quantization of spin angular momentum. The Stern-Gerlach experiment involves sending a beam of neutral silver atoms through an inhomogeneous magnetic field and observing their deflection. If we treat the particle as a classical spinning dipole, it will precess in a magnetic filed as the magnetic field exerts a torque on the magnetic dipole. If the particle moves through homogeneous magnetic field, the forces which are exerted on the opposite ends of the magnetic dipole cancel each other out so, the magnetic field has no effect on the particle's trajectory. However, if we consider an inhomogeneous magnetic field the force exerted on one end of the dipole will be slightly greater than the other end of the dipole and results a net force to deflect the trajectory of the particle. By considering a classical spinning object, one would expect the distribution of the spin angular momentum vector to be random and continuous. It should produce a smooth and continuous distribution on the screen of the detector, after the deflection in the experiment. The particles passing through the Stern-Gerlach apparatus instead had shown a discontinuous distribution, deflected either up or down by a specific amount which indicates the quantized values (discrete distribution) of the spin angular momentum, in other words there is not a continuous distribution of the possible angular momenta. A nice account on the impacts of this experiment is noted in [162]. In 1927, T. E. Phipps and J. B. Taylor reproduced the effect by using hydrogen atoms in their ground state, that reconfirmed the idea of space quantization[163]. Among the descendants of the Stern-Gerlach experiment are the prototypes of nuclear magnetic resonance, optical pumping, the lasers, the atomic clocks also the incisive discoveries like the Lamb-shift, the anomalous magnetic moment of electron leading to quantum electrodynamics and all the experiments exploiting transitions between space quantized quantum states and manipulations of particles motions in a selected quantum state.

With an inhomogeneous field one can select the atoms and molecules in a specific

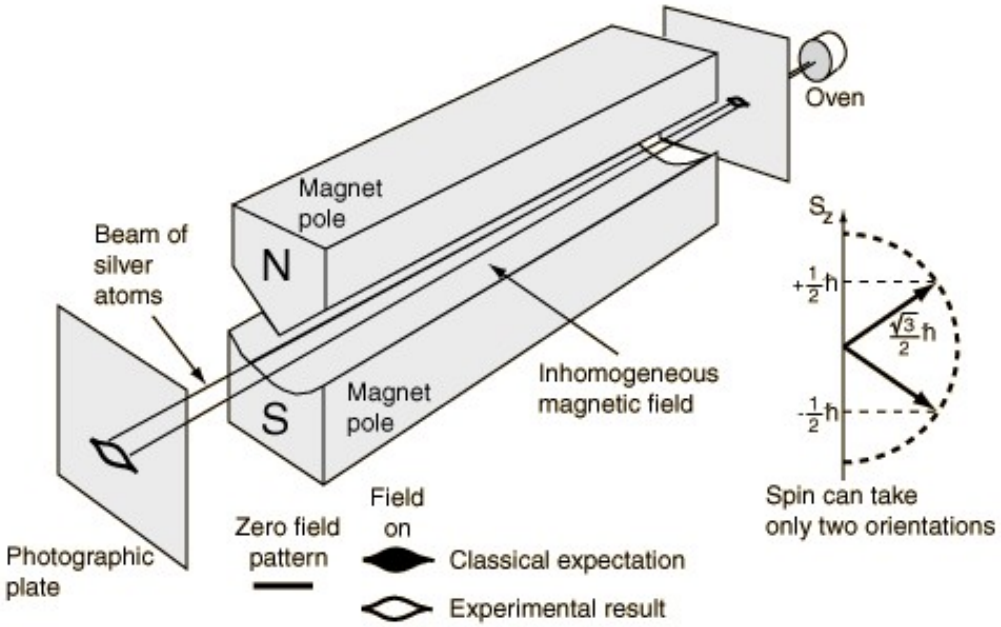

Figure 3.1: The schematic representation of the Stern-Gerlach experiment adopted from *http://hyperphysics.phy-astr.gsu.edu/hbase/quantum/imgqua/steger.*

state due to the space quantization property of a quantum system. This can be used to filter a particular quantum state rejecting the unwanted ones but it does not lead to enhance the signal intensity due to the particles are only in the selected quantum state. However, instead of only filtering, by the use of electric and magnetic lenses to focus the particles (in a quantum state), one can overcome the problem. In the years 1950-60 the physicist had learned that the electric and magnetic multi-pole fields are able to focus particles in two dimensions acting on the electric and magnetic dipole moments. The electrostatic and magnetic focusing of atomic and molecular beams were conceived and realized [164–166] to improve considerably the beam method for spectroscopy or quantum state selection. The lensing technique found its application as well to achieve Microwave Amplification by Stimulated Emission of Radiation (MASER) by using highly dense, state selected ammonia molecules [167].

Since the Maxwell's equations do not allow to have a maximum of static electric or magnetic field in free space [168, 169] the multi-pole field focuses the particles in low-field-seeking states (see next section), which are attracted towards the low field region in an inhomogeneous field. Using this property one can guide an atomic or molecular beam by extending the lens in the beam direction.

This chapter is concerned with a quadrupole magnetic guiding of the beams of paramagnetic atoms. The structure of this chapter is given as follows. In Section3.2 we give

an overview of the Zeeman effect of an atom placed in a magnetic field. Then we describe the experimental set-up for the quadrupole guiding, the driver electronics and the guiding field geometry in the section3.3. The section3.4 presents the details of our experimental results and the 3D-trajectory simulations and finally the conclusion is made in section3.5.

3.2 Atoms in a Magnetic Field

3.2.1 Magnetic moment

Let us consider an electron (with mass m_e and charge $-e$) which has intrinsic spin angular momentum $\mathbf{s}$. The intrinsic magnetic moment $\boldsymbol{\mu_s}$ associated with it can be expressed as

$$\boldsymbol{\mu}_s = -g_s \frac{\mu_B}{\hbar}\mathbf{s} \tag{3.1}$$

where $\mu_B = e\hbar/2m_e c$ is called the Bohr magneton and is effectively the magnetic moment in atomic unit and c is the speed of light in vacuum. g_s is the gyromagnetic ratio for the electron spin which is equal to 2 according to the prediction of Dirac's relativistic theory of electron spin but when the higher order quantum electrodynamics effects are included the value increases by about 0.1%.

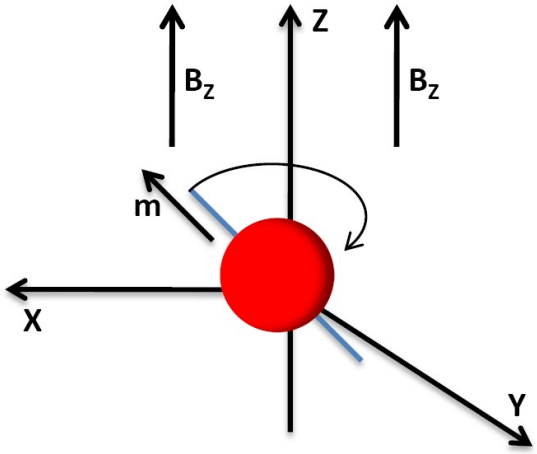

Figure 3.2: The precession of a magnetic dipole ($\mathbf{m}$) when it is placed in a magnetic field ($\mathbf{B_z}$) along z, known as Larmor precession.

If we consider a spinless electron orbiting around a nucleus in a quantum state of orbital angular momentum $\mathbf{l}$, it behaves like a current loop with a magnetic moment $\boldsymbol{\mu_l}$ which is proportional to the orbital angular momentum $\mathbf{l}$:

$$\boldsymbol{\mu}_l = -g_l \frac{\mu_B}{\hbar}\boldsymbol{l} \tag{3.2}$$

where g_l is the gyromagnetic ratio of electron's orbital angular momentum which is equal to 1. The nucleus also often has a magnetic moment, but as it is much heavier and consequently, the magnetic moment is much smaller than that of electron hence we can neglect it in this purpose.

When the electron spin and the orbital angular momentums are taken into account simultaneously (which is the case for an atom), the magnetic moment of each electron becomes,

$$\boldsymbol{\mu}_e = -\frac{\mu_B}{\hbar}(g_s \boldsymbol{s} + g_l \boldsymbol{l}) \tag{3.3}$$

For an N-electron atom, the total magnetic moment is written as,

$$\boldsymbol{\mu} = -\frac{\mu_B}{\hbar}(g_s \boldsymbol{S} + g_l \boldsymbol{L}) \tag{3.4}$$

where $\boldsymbol{S} = \sum_{i=1}^{N} \boldsymbol{s_i}$ and $\boldsymbol{L} = \sum_{i=1}^{N} \boldsymbol{l_i}$. By considering $g_s = 2$, $g_l = 1$ and $\mathbf{J} = \mathbf{L} + \mathbf{S}$ the previous equation reads,

$$\boldsymbol{\mu} = -\frac{\mu_B}{\hbar}(\boldsymbol{J} + \boldsymbol{S}) \tag{3.5}$$

3.2.2 Magnetic energy

The potential energy, V associated with a magnetic moment $\boldsymbol{\mu}$ placed in a uniform magnetic field $\mathbf{B}$ depends on the relative angle between them:

$$V = -\boldsymbol{\mu} \cdot \boldsymbol{B} \tag{3.6}$$

With the magnetic field applied along the z-direction this becomes,

$$V = -\mu_z B_z \tag{3.7}$$

In the absence of magnetic field, the unperturbed energy levels of the atom are always rigorously characterize by the quantum numbers J and m_J, the total angular momentum and it's projection on the magnetic field axis. So, for a quantum level α associated with a state vector $|\alpha J m_J\rangle$ (where α represents all the other quantum numbers of the state) the standard eigenvalue equations hold:

$$J_z|\alpha J m_J\rangle = m_J \hbar |\alpha J m_J\rangle \tag{3.8}$$

$$J^2|\alpha J m_J\rangle = J(J+1)\hbar^2 |\alpha J m_J\rangle \tag{3.9}$$

In absence of the magnetic field the quantum levels are degenerate in m_J due the spherical symmetry. But, the introduction of an axial field breaks this symmetry as well as the degeneracy and splits the m_J levels in various energy states. For a weak magnetic field J and m_J still remain the good quantum numbers and the magnetic energy $\triangle E$ can

be obtained using first order perturbation theory. The shift in energy of the state $|\alpha J m_J\rangle$ is given by

$$\triangle E = \langle \alpha J m_J | V | \alpha J m_J \rangle \tag{3.10}$$

or

$$\triangle E = -B_z \langle \alpha J m_J | \mu_z | \alpha J m_J \rangle \tag{3.11}$$

μ_z is the z-component of the vector operator $\boldsymbol{\mu}$. Now to evaluate the matrix element we use:

$$\langle \alpha J m_J | m_L + 2 m_S | \alpha J m_J \rangle = \frac{\langle \alpha J m_J | (\boldsymbol{L} + 2\boldsymbol{S}) \cdot \boldsymbol{J} | \alpha J m_J \rangle}{\hbar^2 J(J+1)} \langle \alpha J m_J | J_z | \alpha J m_J \rangle \tag{3.12}$$

where m_S and m_L are the projections of S and L on the quantization axis. Since $\langle \alpha J m_J | J_z | \alpha J m_J \rangle = m_J \hbar$ the shift in energy becomes,

$$\triangle E = -B_z \frac{m_J}{\hbar J(J+1)} \langle \alpha J m_J | \boldsymbol{J} \cdot \boldsymbol{\mu} | \alpha J m_J \rangle \tag{3.13}$$

With the $\boldsymbol{\mu}$ from Eqn:3.5 the above expression can be written as

$$\triangle E = \mu_B B_z m_J \frac{\langle \alpha J m_J | J^2 + \mathbf{J} \cdot \mathbf{S} | \alpha J m_J \rangle}{\hbar^2 J(J+1)} \tag{3.14}$$

or

$$\triangle E = \mu_B B_z m_J \left(1 + \frac{\langle \alpha J m_J | \mathbf{J} \cdot \mathbf{S} | \alpha J m_J \rangle}{\hbar^2 J(J+1)} \right) \tag{3.15}$$

One can see that the magnetic energy depends on the matrix element of the projection of **S** on **J**. Again, the matrix element does not depend on the choice of the z-axis and independent of m_J. The dependence of the weak field Zeeman-effect on m_J lies entirely in the proportionality which is expressed in Eqn.3.15 and known as the g-factor of the level

$$g_{\alpha J} = 1 + \frac{\langle \alpha J m_J | \mathbf{J} \cdot \mathbf{S} | \alpha J m_J \rangle}{\hbar^2 J(J+1)} \tag{3.16}$$

So, the magnetic energy becomes

$$\triangle E = g_{\alpha J} \mu_B B_z m_J \tag{3.17}$$

If we consider an atom in an inhomogeneous magnetic field, depending on the orientation of the projection of the total angular momentum along the field axis, the atom can minimize its potential energy in a low field field region (known a low field seeker) and in a high field region (high field seeker) as one can see from the Eqn:3.17.

3.2.3 Spin-Orbit coupling and Zeeman Effect in Atoms

The effect of spin on a charged particle's motion in an electro-magnetic field is known as the spin-orbit interaction. The general expression of the Hamiltonian considering the spin-orbit interaction is $H = H_0 + H_{SO}$ where H_{SO} is written as

$$H_{SO} = W(r)\mathbf{L} \cdot \mathbf{S} \tag{3.18}$$

where $\mathbf{L}$, $\mathbf{S}$ are the orbital and spin angular momentum and $W(r)$ is the spin-orbit coupling constant. H_0 is the unperturbed Hamiltonian of the atom represents a familiar central-force problem as,

$$H_0 = -\frac{\hbar^2}{2m} \bigtriangledown^2 + V(r) \tag{3.19}$$

where the first term represent the kinetic energy while the second term represents the potential energy. We can immediately recognize that neither $\mathbf{L}$ nor $\mathbf{S}$ commutes with the complete Hamiltonian H. But, the total angular momentum vector operator $\mathbf{J} = \mathbf{L} + \mathbf{S}$, does commute with the H since $\boldsymbol{L} \cdot \boldsymbol{S} = 1/2(J^2 - L^2 - S^2)$. The simultaneous eigenstates can be formed by the mutually commuting coupled operators L^2, S^2, J^2 *and* J_z (instead of the uncoupled operators L^2, L_z, S^2 *and* S_z). These make up a suitable set of correct unperturbed basis functions, as the perturbation matrix is automatically diagonal with respect to them.

Now, if we consider an atom, exposed to a constant uniform magnetic field along z-axis the Hamiltonian becomes $H_T = H_0 + H_{SO} + H_Z$ where H_Z is expressed as

$$H_Z = \frac{\mu_B}{\hbar}(g_s S_z + g_l L_z) \cdot B_z \tag{3.20}$$

is the Zeeman Hamiltonian and as we mentioned before g_s *and* g_l are equal to 2 and 1, respectively. In general cases, the matrix element of $H_{SO} + H_Z$ is small compared to H_0.

Now we shall divide our discussion into two parts: the weak field case and the strong field case. These two different cases are determined by the spin-orbit interaction energy. If the change in potential energy (the Zeeman energy) due to the presence of magnetic field is smaller as compare to the spin-orbit interaction energy, the field is considered to be *weak* otherwise it is *strong*. The weak field case is the regime of the ordinary Zeeman effect while the strong field case is corresponding to the Paschen-Back effect.

For the weak field case, it is well presumed that the spin-orbit coupling effect has already been taken into account, consequently the eigenstate functions are described in the coupled angular momentum basis sets. In this coupling case, the quantum state $|\alpha J m_J\rangle$ of an N-electron atom is an eigenstate state of L^2, S^2, J^2 and J_z where $\mathbf{L} = \sum \mathbf{l_i}$, $\mathbf{S} = \sum \mathbf{s_i}$ and $\mathbf{J} = \mathbf{L} + \mathbf{S}$. Generally the quantum state is written in this case as

$$|\alpha J m_J\rangle = |\gamma L S J m_J\rangle \tag{3.21}$$

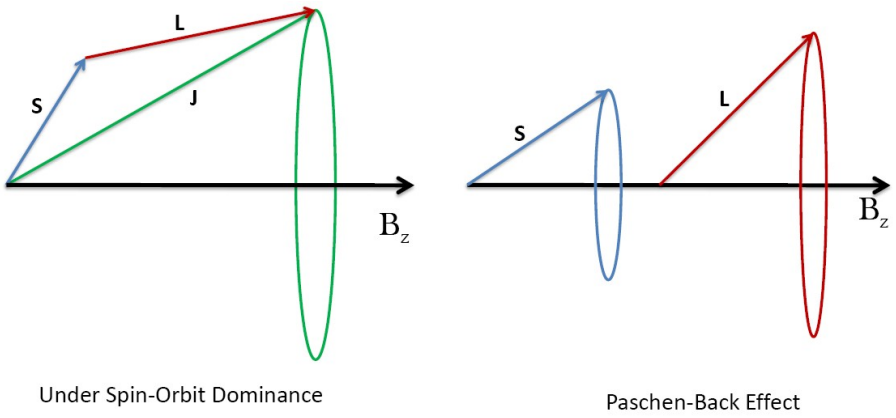

Figure 3.3: The coupling of the spin and the orbital angular momentum in weak (the figure on the left) and strong field (the figure on the right) regimes.

where γ represents all other quantum numbers to specify the state. Furthermore, the assumption of weak field case already considers that the individual quantum states due to only the spin-orbit coupling are well apart and isolated so that the attention can be confined to the matrix elements which are diagonal in L, S, and J. Now, the Zeeman matrix element in this basis is expressed as

$$\langle \gamma LSJm_J|m_L+2m_S|\gamma LSJm_J\rangle = \frac{\langle \gamma LSJm_J|(\boldsymbol{L}+2\boldsymbol{S})\cdot\boldsymbol{J}|\gamma LSJm_J\rangle}{\hbar^2 J(J+1)}\langle \gamma LSJm_J|J_z|\gamma LSJm_J\rangle \tag{3.22}$$

Since $(\boldsymbol{L}+2\boldsymbol{S})\cdot\boldsymbol{J} = J^2+\boldsymbol{J}\cdot\boldsymbol{S}$ and $\boldsymbol{J}\cdot\boldsymbol{S} = \frac{1}{2}(J^2+S^2-L^2)$, we obtain,

$$\frac{\langle \gamma LSJm_J|(\boldsymbol{L}+2\boldsymbol{S})\cdot\boldsymbol{J}|\gamma LSJm_J\rangle}{\hbar^2 J(J+1)} = 1+\frac{(J(J+1)+S(S+1)-L(L+1))}{2J(J+1)} \tag{3.23}$$

Substituting it in Eqn.(3.14), the g-factor is expressed as

$$g_{\alpha J} = g_{LSJ} = 1+\frac{J(J+1)+S(S+1)-L(L+1)}{2J(J+1)} \tag{3.24}$$

g_{LSJ} is called the Landé g-factor and depends only on L, S, and J.

As the strength of the magnetic field is increased to the point where the splitting in energy due to the presence of the magnetic field becomes comparable to the splitting in energy due to the spin-orbit coupling, it is no longer legitimate to isolate a quantum state with specific value of $\mathbf{J}$. In this case the perturbative Hamiltonian is written as

$$H' = W(r)\mathbf{L}\cdot\mathbf{S}-\frac{\mu_B}{\hbar}(L_z+2S_z)B_z \tag{3.25}$$

The calculations are most conveniently done in the uncoupled basis sets $|\gamma Lm_L Sm_S\rangle$. So the matrix element due to the Zeeman interaction becomes

$$\langle \gamma L'm'_L Sm'_S|(L_z+2S_z)|\gamma Lm_L Sm_S\rangle = (m_L+2m_S)\delta_{L'L}\delta_{m'_L m_L}\delta_{m'_S m_S} \tag{3.26}$$

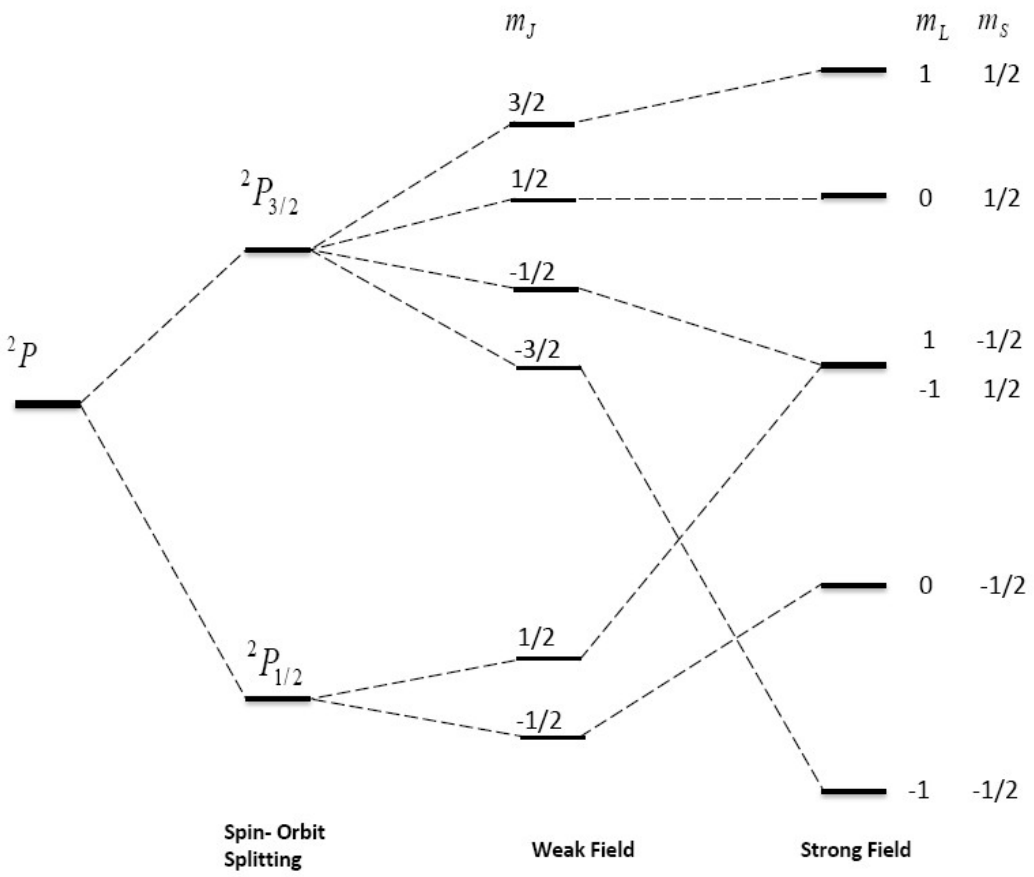

Figure 3.4: The Zeeman splitting of ^2P quantum state in the weak and strong field regime.

By expressing **L** and **S** in their spherical component, the matrix element of the spin-orbit coupling can be written as

$$\langle \gamma L' m'_L S m'_S | \mathbf{L} \cdot \mathbf{S} | \gamma L m_L S m_S \rangle = \langle \gamma L' m'_L S m'_S | -L_+ S_- + L_0 S_0 - L_- S_+ | \gamma L m_L S m_S \rangle \quad (3.27)$$

which will vanish unless

$$\triangle m_L = 0, \ \pm 1, \quad \triangle m_S = 0, \ \pm 1 \quad (3.28)$$

Let us consider a quantum state ^2P with $\mathbf{l} = 1$ and $\mathbf{s} = 1/2$. Since it has non-zero spin and orbital angular momentum, the quantum state will split in various coupled angular momentum (J) states due the spin-orbit coupling. In this case, they are $^2P_{3/2}$ and $^2P_{1/2}$ correspond to $J = 3/2$ and $1/2$, respectively. Now if we place it in a weak magnetic field where energy splitting due to the presence of the magnetic field is less than that of the spin-orbit coupling, these individual quantum states split in various m_J (the projection of J on the magnetic field axis) due to the Zeeman interaction. In the opposite limit where the magnetic field is strong compared to the spin-orbit interaction, the magnetic

field dissolves the spin-orbit coupling, i.e., **l** and **s** are practically decoupled and precess independently around magnetic field axis (shown in Fig.3.3). Therefore the quantum number J looses its meaning and various J and m_J levels are mixed as shown in the Fig.3.4.

3.2.4 Zeeman Effect in Helium and Argon

For helium atom, the ground state (^1S) has the electronic configuration $1s^2$. In the first metastable excited state (^3S) with the electronics configuration is $1s^12s^1$ and has no spin-orbit interaction as $\boldsymbol{L} = 0$. The electronic configuration of the ground state of argon atom is $1s^22s^22p^63s^23p^6$, whose only energy level is $^1S_0$. The next higher configurations are the $1s^22s^22p^63s^23p^54s^1$ and $1s^22s^22p^63s^23p^54p^1$ which have respectively, 4 and 10 energy levels. Assuming for the moment that LS coupling holds, then adding the angular momentums of 4s electron having $l = 0$ and $s = 1/2$ with the 17-electron core $1s^22s^22p^63s^23p^5$ of $l = 1$ and $s = 1/2$ and using the normal rule for addition of angular momentum imply that, the only allowed value of **L** would be **L** = 1 (P-state) and two allowed values for **S**: **S** = 0 (singlet states) and **S** = 1 (triplet states). So, the four states of this configuration would be $^1P_1$ and $^3P_{0,1,2}$. The ten states of the second excited configuration in LS coupling would be $^1S_0$, $^1P_1$, $^1D_2$, $^3S_1$, $^3P_{0,1,2}$ *and* $^3D_{1,2,3}$. Among these states the lower and accessible metastable states are $^3P_0$ and $^3P_2$, in our experiment. The spin-orbit splitting in the ^3P way much higher (as one can see in Table 3.1) than that of the splitting ($\sim 1cm^{-1}$) due to the Zeeman effect in our experiment. Therefore, we are in the weak field regime.

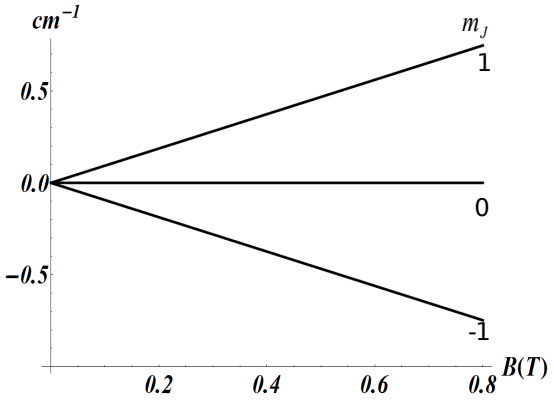

Figure 3.5: The Zeeman diagram of metastable He atom in $^3S_1$. The Zeeman shift is linear within the magnetic field ($\sim 0.8T$) used in the experiment.

The ground states of argon and helium atoms are diamagnetic as they have closed shell electronic structure. So, they do not interact with the external magnetic field. But

Paschen label	Level	J	Energy (cm^{-1})
ground	$3p^6\ ^1S_0$	0	0.0
$1s_5$	$4s[3/2]^o_2\ ^3P_2$	2	93143.8
$1s_4$	$4s[3/2]^o_1\ ^3P_1$	1	93750.6
$1s_3$	$4s'[1/2]^o_0\ ^3P_0$	0	94553.7
$1s_2$	$4s'[1/2]^o_0\ ^1P_1$	1	95399.8
$2p_{10}$	$4p[1/2]_1\ ^3S_1$	1	104102.1
$2p_9$	$4p[5/2]_3\ ^3D_3$	3	105462.8
$2p_8$	$4p[5/2]_2\ ^3D_2$	2	105617.3
$2p_7$	$4p[3/2]_1\ ^3D_1$	1	106087.3
$2p_6$	$4p[3/2]_2\ ^3P_2$	2	106237.6
$2p_5$	$4p[1/2]_0\ ^3P_0$	0	107054.3
$2p_4$	$4p'[3/2]_1\ ^1P_1$	1	107131.7
$2p_3$	$4p'[3/2]_2\ ^1D_2$	2	107289.7
$2p_2$	$4p'[1/2]_1\ ^3P_1$	1	107496.4
$2p_1$	$4p'[1/2]_0\ ^1S_0$	0	108722.6

Table 3.1: The different energy levels of Argon(I), adopted from NIST [170].

if we excite them to a metastable electronic state (e.g., for argon $1s^22s^22p^63s^23p^54s^1$ and for helium $1s^12s^1$) they experience the Zeeman splitting. The life-time of the argon $^3P_2$ metastable state and helium $^3S_1$ metastable state are 38s and 8000s, respectively which is sufficient enough since the typical time-of-flights (TOFs) for our experiment are in the order of milliseconds. For our quadrupole guiding experiment the maximum magnetic field strength experienced by the atoms is 0.06 Tesla. The corresponding change in potential energy for metastable Ar ($^3P_2,\ m_j = 2$) and metastable He ($^3S_1,\ m_j = 1$), respectively are

$$\Delta E_{Ar} = 10.42 \times 10^{-6}\ eV \quad (0.084\ cm^{-1}) \tag{3.29}$$

$$\Delta E_{He} = 6.95 \times 10^{-6}\ eV \quad (0.056\ cm^{-1}) \tag{3.30}$$

The Zeeman diagram for metastable helium in ^3S and argon in $^3P_2$ state are presented in Fig.3.5 and Fig.3.6, respectively.

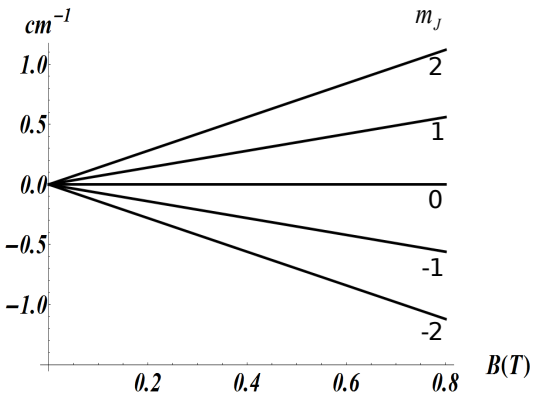

Figure 3.6: The Zeeman diagram of Ar atom in $^3P_2$ metastable state. It exhibits a linear Zeeman shift within the magnetic field ($\sim 0.8T$) used in the experiment.

3.3 Quadrupole Guiding

We have performed the magnetic guiding experiment with the beam of metastable helium and argon beams. The experimental set-up consists of three major sections. The first section devoted to the production of the metastable beams is referred as the source-chamber, the second section consists of a long narrow glass tube, connecting the source-chamber to the detection-chamber, the third section, where the MCP detector is mounted. This second section (glass-tube) is dedicated to the guiding coils. A schematics of the whole set-up is presented in Fig.3.7. The production of the metastable beams are carried out by letting them pass through two stainless-steel discharge electrodes after the supersonic expansion from $Liq.N_2$ cooled valve. The electrodes are placed right after the exit of the valve. The typical voltage difference between the electrodes are $\sim 1000V$ for He and $\sim 850V$ for Ar beams, respectively. After the discharge, the beam passes through a $2mm$ diameter skimmer to filter out and collimate the dense central part of the supersonic beam. The Skimmer is placed at $2cm$ downstream to the end of discharge electrodes along the beam direction. Right after that, the beam enters the long narrow glass tube. The quadrupole guiding coil is placed around the glass tube (see next subsection). After the beam is guided, while it is passing through the tube, the atoms are detected by the MCP detector when they are impinging on the MCP. In all the experiments presented here, the quadrupole guiding coil is operated between 0A to 100A currents in the guide. The mean velocity and the velocity distribution of the helium and argon beams are extracted from the MCP signal where the MCP detector is installed 59.5cm downstream from the valve.

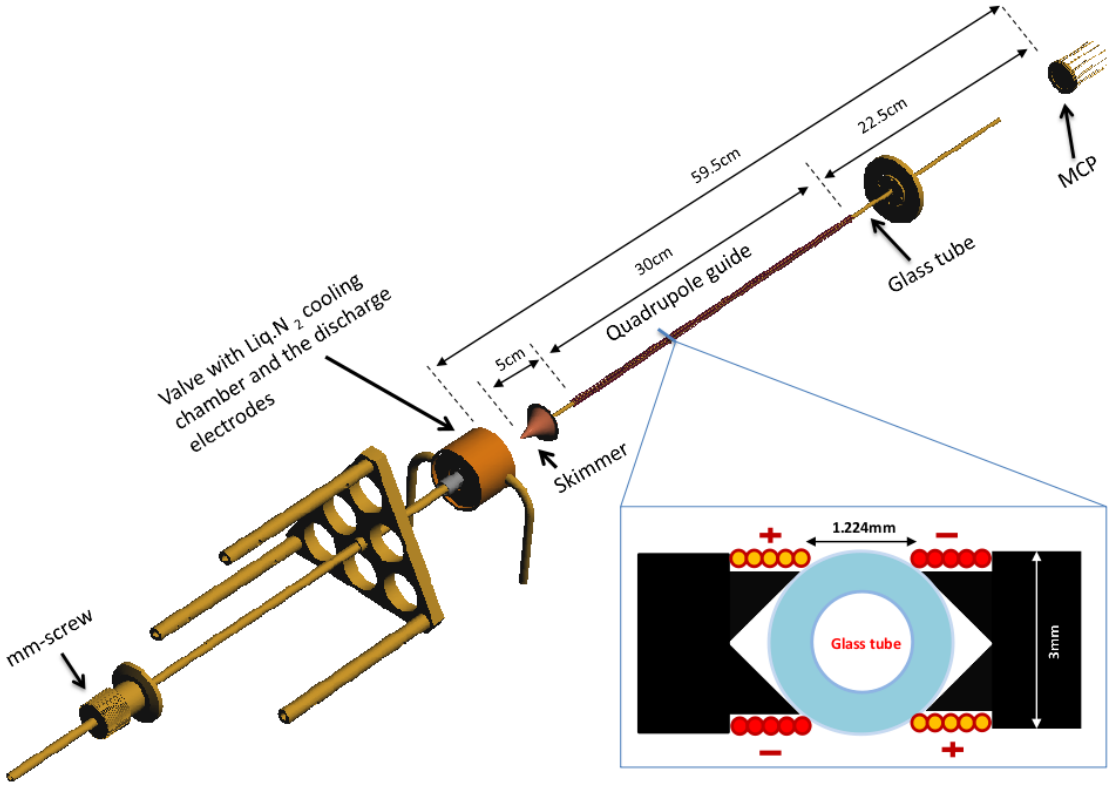

Figure 3.7: The scheme of the supersonic beam set up with quadrupole guiding coil and the detection apparatus. The supersonic beam is produced by expanding the gas through the nozzle (1mm diameter) of the valve. The stainless steel discharge electrodes are mounted right after the nozzle to produce metastable beams. The skimmer is placed 2cm downstream from the valve exit. The beam passes through a 43cm long, 1.2mm inner-diameter glass tube. The MCP detector is installed 59.5cm downstream from the valve exit. The quadrupole guide (with the copper wire diameter 0.345mm) starts at 7cm and ends at 37cm from the valve exit. The inset shows the arrangement of the quadrupole wires around the glass tube. The signs are indicating the direction of the currents flowing in the wires.

3.3.1 The Quadrupole Set-Up and the Field Geometry

The quadrupole guide set-up is schematically depicted in Fig.3.7. It consists of four set copper wires which are placed around the glass tube. Each set has five wires of 30cm long and 0.345mm diameter, are held parallel together in a plane to increase the magnetic field strength inside the guide. The neighboring wire-sets carry current of opposite sign. The quadrupole guide is coaxial with the beam axis or in other words coaxial with the glass tube. The magnetic field strength is zero on the axis of the glass-tube and the field strength rises with distance from the center. The trapping region for an atom with low field seeking state is defined by the central region of the guide. The field geometries, calculated by Biot-Savart Law are shown in the Fig.3.8 and Fig.3.9. With a current of 100A in the copper wire, a maximum magnetic field can be achieved up to 0.06 Tesla inside the glass-tube while the diameter of the glass-tube is 1.2mm.

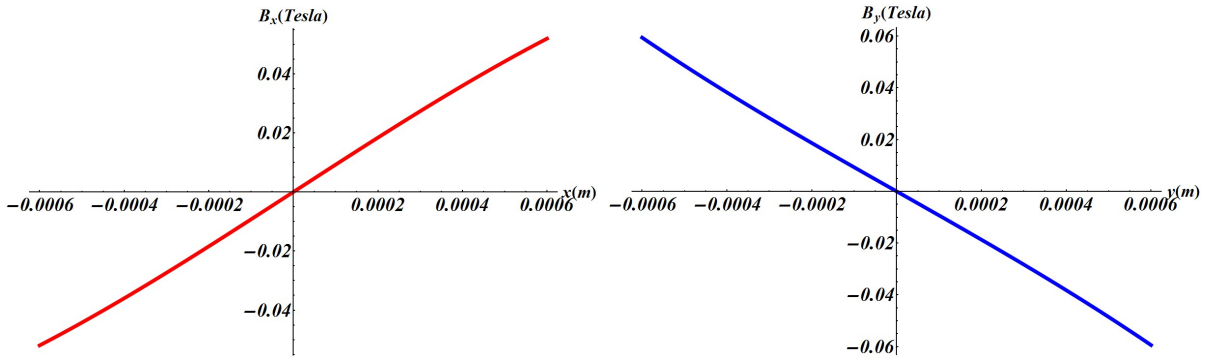

Figure 3.8: The magnetic field vectors inside the quadrupole guide with 100A current. The figures show the variation of magnetic field vectors B_x and B_y along the radial directions. With in the inner-diameter (1.2mm) of the glass tube the field components vary almost linearly.

Since the guiding coil has a finite length (30 cm), the magnetic flux density inside the guide is different from the magnetic flux density at the entrance (exit). The magnetic field along the beam axis is zero. But if we consider it at a position away from the beam axis, the magnetic field slowly increases as we approach the entrance and reaches a constant value which has been shown in Fig.3.10. The reverse effect is also present at the exit of the guide. A non-zero field is present at 5mm before the entrance of the guide and it reaches the constant value at 5mm after the entrance of the guide. The typical mean velocity of a supersonic beam, in our experiment is nearly 500m/s. As a result, the beam spend very little time while it traverses through this region and consequently has a negligible effect on the particles trajectories of the beam. So, this inhomogeneity of the field does not introduce any observable effect in the signal of the guided beam.

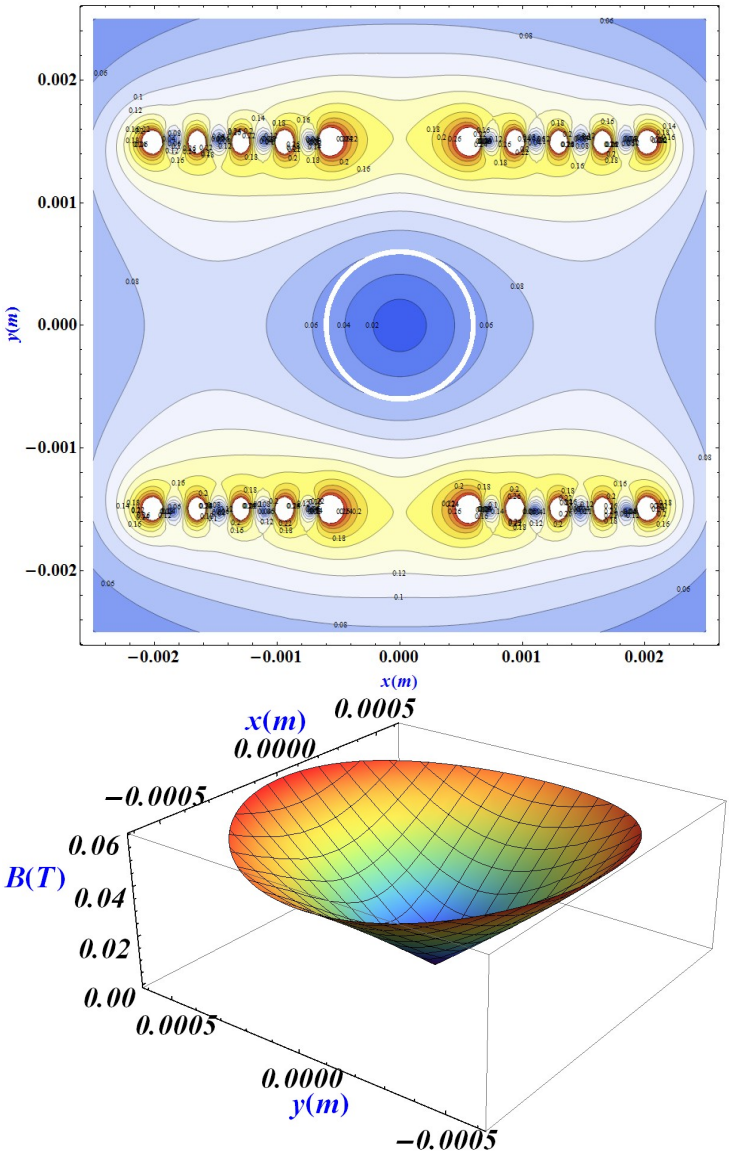

Figure 3.9: The magnetic field geometries inside the quadrupole guide with 100A current. The upper figure (the contour plot) shows the variation of magnetic field strength along the radial directions. The white circle in the middle indicates the position of the glass tube with the inner diameter 1.2mm. The lower figure shows the 3D-view of the field and indicates a nearly linear variation of the magnetic field strength along the radial directions.

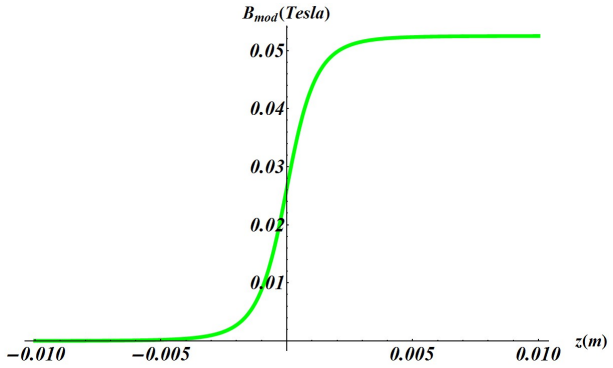

Figure 3.10: The variation of the magnetic field strength at the entrance (exit) of the quadrupole guide with 100A current at a radial position $x = 0.4mm$ and $y = 0.4mm$. The field is almost zero at 5mm far from the beginning (end) of the quadrupole guide. At the position where the guide starts, it acquires 0.025 Tesla of magnetic field and gradually increases to the steady value of 0.052 Tesla within 5mm in side the guide.

3.3.2 The Driver Electronics

The guiding of the paramagnetic atoms are performed by fast switching the DC current in the guiding coil. The current is driven to the coil by discharging a high energy capacitor in a pulsed mode. The fast switching is done using IGBTs (Insulated Gate Bipolar Transistor). The schematics of the electronics, which is used in our experiment, is shown in Fig.3.11. The input TTL pulses from NI-card which is driven by the LabView program, to charge and discharge the 2mF capacitor (C1 in the Fig.3.11) connected to a power supply which can provide 300V with 100mA limiting current. The Q1 IGBT is used for charging the high energy capacitor and the other Q2 and Q3 IGBTs are used for discharging the high energy capacitor to flow the current in the guiding coil. The charge and discharge of the capacitor are carried out using two independent TTL pulses. To keep the low-voltage electronics part in safe we introduce a time delay between the charge and the discharge pulses. The pulse sequences for the guiding experiment are depicted in Fig.3.12.

A typical pulse of the DC current flown in the guiding coil is shown in Fig.3.13. The current in the wires of the guiding coil is measured with *LeCroy current Probe* (CP500). The profile of the current follows the exponential decay,

$$I(t) = \frac{V_0}{R} exp(-t/RC) \tag{3.31}$$

where $R = 1.5\Omega$ is the load and $C = 2mF$ is the capacitance. V_0 is the capacitor voltage at $t = 0$.

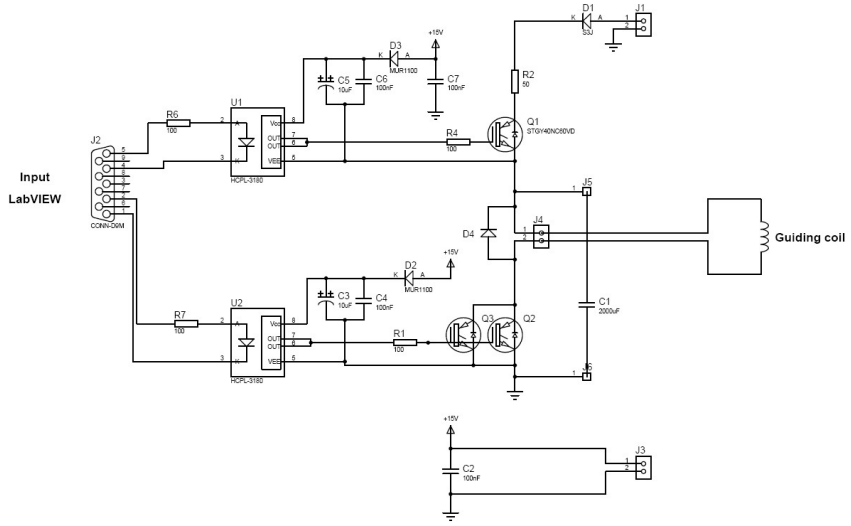

Figure 3.11: The schematics of the electronic-driver circuit, designed for the magnetic quadrupole guide.

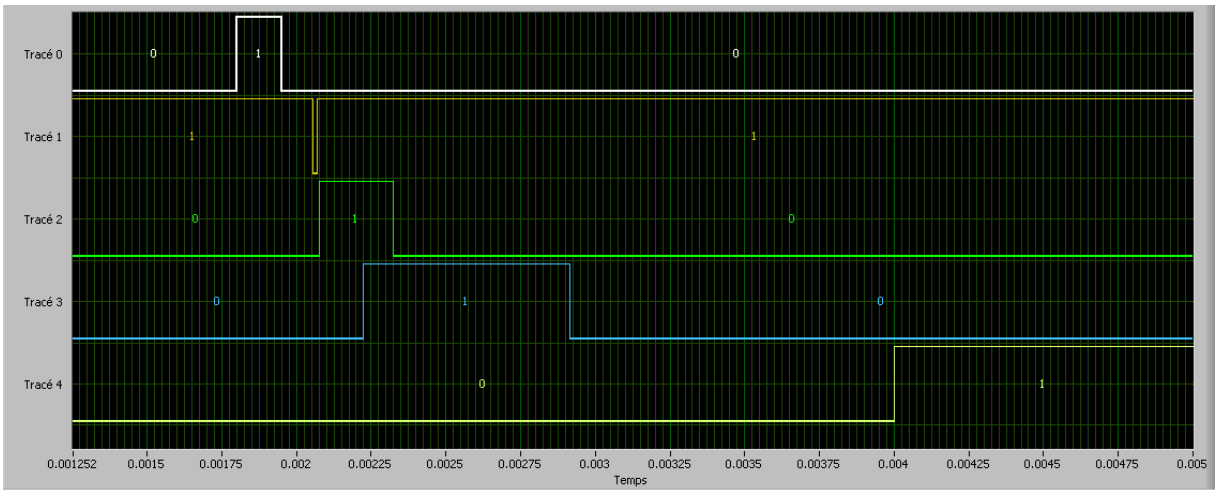

Figure 3.12: The typical scheme of the various pulse sequences in the guiding experiment. The trace0 (in white) represents the pulse ($\sim 180\mu s$ long) for the General Valve for the supersonic expansion while the trace1 (in yellow) indicates the voltage pulse ($\sim 15\mu s$ long) for the electric glow discharge which starts $\sim 75\mu s$ after the end of the valve pulse. The trace2 (in green) shows the trigger of the experiment. The $\sim 650\mu s$ long guiding current pulse is indicated in trace3 (in blue) while the trace4 (in greenish-yellow) represents the $\sim 600ms$ pulse to charge up the capacitor and it starts relatively long after the end of the guiding current pulse.

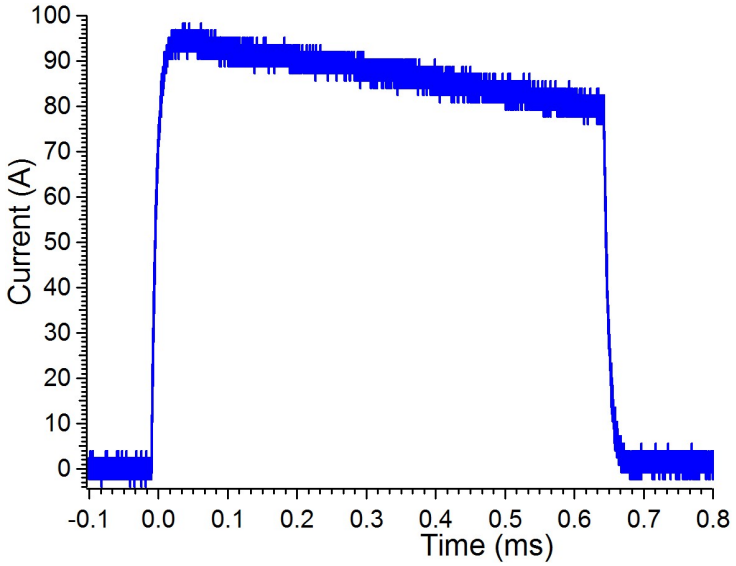

Figure 3.13: The experimentally observed 650μs long DC current pulse flown to the guiding coil when it is connected to 200V.

3.4 Experimental Results and Simulations

A beam of atoms (or molecules) diverges as it moves due to the presence of non-zero velocity spread in the radial direction. If we let the beam passes through a long narrow glass tube during its flight, which is the case for our experiment, a significant number of atoms crash on the inner wall of the tube. The number of particles crash increases with the increase in the length of the glass tube. On the other hand, if we focus the particles in the radial direction by implementing the quadrupole guide the atoms can be guided to the detector without much spread in the radial direction results an increase in the intensity of the beam consequently, an increase in MCP signal.

Let us consider the case for metastable argon atoms in $^3P_2$ quantum state, emphasize on the population distribution of various magnetic quantum sates and the fate of these states while the magnetic guiding is in progress. In the absence of the magnetic field, all the magnetic sublevels (m_J) are degenerate, which is the consequence of the spherical symmetry. But, as we gradually increase the magnetic field (the case when they enter the magnetic guide) the degeneracy breaks. The splitting in energy depends on whether the projection of the spin is parallel or anti-parallel to the applied magnetic field. The population in the various splitted energy levels shall be distributed equally. The reasons behind it is that, the $^3P_2$ metastable state of argon is 93143.8 cm^{-1} above the ground state $^1S_0$ while the typical splitting energy for various magnetic quantum states are in the order of 0.1 cm^{-1} in a magnetic field ($\sim 0.06T$) reachable in our experiment. So, the population distribution according to Boltzmann statistics is nearly uniform in these mag-

netic sublevels. Moreover, there are no accessible thermalization process as the collisions between the atoms are highly improbable in a supersonically expanded beam. This is also similar for the metastable helium beam as the metastable state (^3S) is $159855cm^{-1}$ above the ground state (^1S).

As we have mentioned in the last section, the positive m_J levels are only trapped in the magnetic guide, while the negative m_J are repelled out of it. So, out of these five levels ($^3P_2,\ m_J = 2,\ 1,\ 0,\ -1,\ -2$), the argon atoms with $m_J = 1$ and $m_J = 2$ are trapped in the magnetic guide. Again, the argon atoms with ($^3P_2,\ m_J = 0$) and ($^3P_0,\ m_J = 0$) are passed trough the guide as if there is no magnetic field since they do not interact with it and of course, they contribute to the MCP signal. For the helium atoms, only the $^3S_1,\ m_j = 1$ is guided while the $^3S_1,\ m_j = 0$ and $^1S,\ m_j = 0$ pass through the guide without interacting with it.

The observed effect of the magnetic quadrupole guiding of metastable helium and argon beams in the experiment, are presented in Fig.3.14 and Fig.3.16, respectively. The intensity of the TOF signal increases with the increase in current in the quadrupole guiding coil. That is expected as the guiding force (the gradient of the magnetic field strength inside the guide) increases with higher guiding current consequently capturing higher radial velocity components in the beam. We have observed that the integrated area of the TOF signal of metastable argon beam is increased to ~ 4 times (see Fig.3.17) with 100A current to the non-guided signal, while for metastable helium beam it is nearly 1.5 times. We also have noticed that the intensity of the signal slowly saturates as we rise the guiding current in the guiding coil after 100A.

Within the dimension of the tube (with 1.2mm diameter) the magnetic field strength can be considered as cylindrically symmetric, within a good approximation. The velocity acceptance in the radial direction for argon atoms in $^3P_2,\ m_J = 2$ quantum state with a 100A current in the guiding coil is $\sim \pm 6m/s$ while for helium atoms in $^3S_1,\ m_J = 1$ quantum state with the same guiding current is $\sim \pm 17m/s$.

One must note that, the inclusion of the guiding field can also lead to a loss in beam intensity. In the experiment the glass tube is longer than the quadrupole guide and after the end of the quadrupole guide the atoms still pass through the rest of the glass tube ($\sim 20cm$ long) to the detector and can crash due to strong focusing effect. The numerical simulations for an imaginary beam with zero initial velocity spread in the radial direction shows that the guiding field can lead to a substantial loss as it introduces a velocity spread in the radial direction and results in particles loss which is due to the crash on the glass-tube, after the quadrupole guide ends. Presence of non-zero radial velocity spread in the beam shows that the beam intensity at the detector increases then acquires a maximum value and finally decreases with the increase in guiding current. For example, for the beam of argon in $^3P_2,\ m_j = 2$ state and with $3m/s$ radial velocity spread reaches maximum

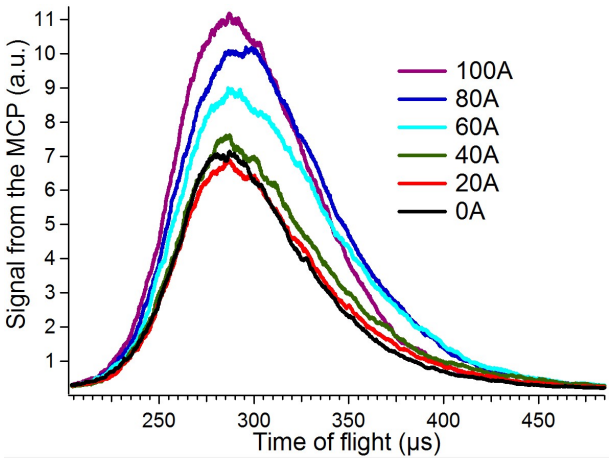

Figure 3.14: The observed signals (TOF distribution) from the MCP using various currents in the quadrupole guiding coil. It shows the quadrupole guiding of helium beam at room temperature ($\sim 300K$). The mean velocity and the longitudinal velocity spread of the helium beam are 1880m/s and 220m/s ($\sim 23K$). The signal increases as the guiding current rises from 0A to 100A. The guided signal is increased by ~ 1.5 times with 100A guiding current with respect to the non-guided signal. The mean velocity and the longitudinal velocity spread of the beam does not change with various guiding currents.

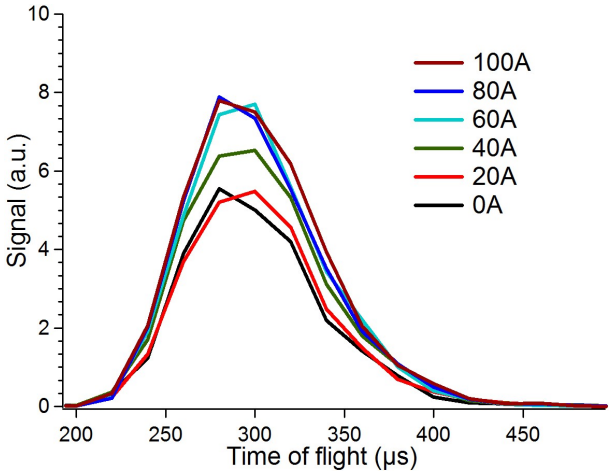

Figure 3.15: The simulated signal (TOF distribution) of helium beam with various currents in the quadrupole guiding coil, at room temperature ($\sim 300K$). We keep the mean velocity and the longitudinal velocity spread similar as the experimental results shown in Fig.3.14.

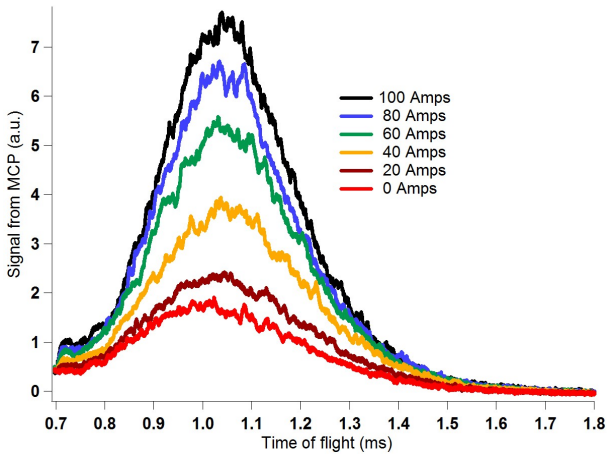

Figure 3.16: The observed TOF distribution using various currents in the quadrupole guiding coil. It represents the quadrupole guiding of argon beam at $Liq.N_2$ cooled temperature $\sim 158K$. The mean velocity and the longitudinal velocity spread of the argon beam 540m/s and 80m/s respectively ($\sim 31K$). The mean velocity as well as the longitudinal velocity spread of the beam does not change with various guiding currents.

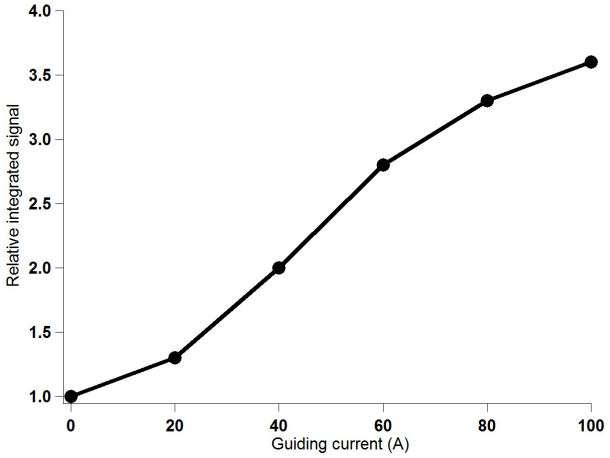

Figure 3.17: The relative increment in integrated MCP signal with various guiding currents, observed in the experiment. The figure indicates the increment in number of guided atoms due to the quadrupole guiding of argon beam at $Liq.N_2$ cooled temperature $\sim 158K$ with various currents. The integrated signal increases by ~ 4 times in the case of 100A guiding current than that of 0A.

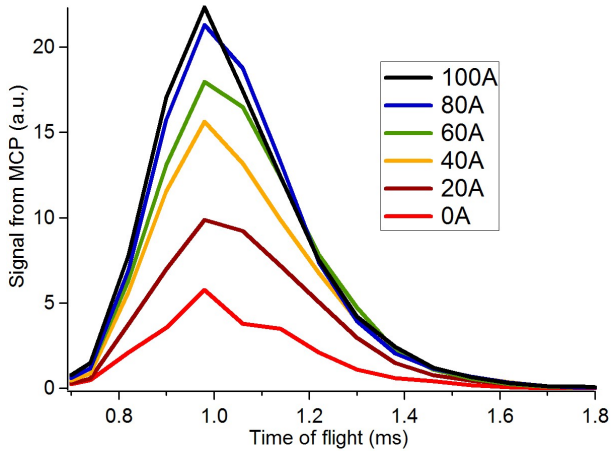

Figure 3.18: The simulated TOF distribution of argon beam using various currents in the quadrupole guiding coil. The TOF distribution shows the quadrupole guiding of argon beam at $Liq.N_2$ cooled temperature $\sim 158K$. In the simulations, the uniform position distribution (with $\triangle z = 6mm$, $r = 0.5mm$ at t=0) and the Gaussian distribution with velocity spread $\triangle v_r = 8m/s$, are considered. We keep the mean velocity and the longitudinal velocity spread similar as the experimental results shown in Fig.3.16.

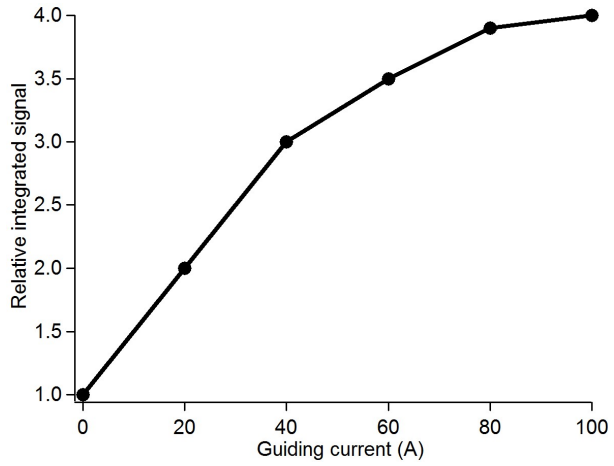

Figure 3.19: The relative increment in integrated MCP signal with various guiding currents, is carried out by 3D-trajectory simulations. The figure indicates the increment in number of guided atoms due to the quadrupole guiding of argon (in $^3P_2$) beam at $Liq.N_2$ cooled temperature $\sim 158K$ with various currents. The integrated signal increases by ~ 4 times in the case of 100A guiding current than that of 0A.

intensity at 80A guiding current while it is reduced with 100A guiding current due to strong focusing. So, the increment in the observed signals due to the quadrupole guiding results from the collecting effect of these two counter-intuitive processes.

The numerical simulations are carried out to see the effect of quadrupole guiding. The magnetic field is calculated (using Biot-Savart law) and imported in a grid (with 10000 grid-points/m in x, y, z-directions) to a program written in C++ language which is dedicated to the 3D-trajectory simulation. The magnetic field is interpolated using linear interpolation and used to calculate the particles motions by numerically (using Runge-Kutta Nyström algorithm) integrating the equation of motion. In the simulations, the initial cloud is created using random generators, at position of the valve. The position distributions inside the valve (with diameter of 1mm and 6mm long) are considered to be uniform while the velocity distributions are Gaussian. Due to the constraint imposed by the radius of the valve nozzle and the glass-tube at the entrance of the guide, the accepted radial velocity spread of the beam is limited and depends on the longitudinal velocity and the position of the atoms. For an argon atom with the velocity 540m/s can have maximum $\sim \pm 8.5 m/s$ radial velocity such that it reaches the entrance of the quadrupole guide without being crashed before. It indeed, indicates that the radial velocity distribution of the atoms in the beam which are reaching the entrance of the quadrupole guide, has a truncated Gaussian distribution.

The numerical 3D-trajectory simulations of the time of flight (TOF) distributions and the effect of magnetic guide on TOFs have been performed and presented in Fig.3.15 and Fig.3.18 for metastable helium and argon beams, respectively.

In absence of the guiding field the only atoms reaching the detector from the valve are those with small enough transverse velocity, such that they do not crash on the inner wall of the glass-tube and make through it. In the presence of the quadrupole guiding field the particles are trapped in the radial direction and oscillates in the finite region inside the glass-tube (see Fig.3.21) and finally reach the detector. More is the strength of the guiding field more will be number of guided particles with higher velocity components along the radial directions (see Fig.3.20). As a result, the integrated area under the simulated time of flight signal increase with higher guiding current as shown in Fig.3.19.

For helium, the integrated area under the simulated TOF is increased nearly by 1.5 times for 100A guiding current than that of non-guided signal. This is well agreed with the experiment. For the magnetic guiding of the argon atoms we see from the simulated TOF that the integrated area is increased by nearly 4 times with 100A than that of the signal without the magnetic guiding which is also the case for the experimental results.

The atoms are radially trapped in the quadrupole guide and oscillate in the radial direction with respect to the beam axis in their flight to the detector as they feel a restoring force towards the beam axis. The 3D-trajectory simulations show that the

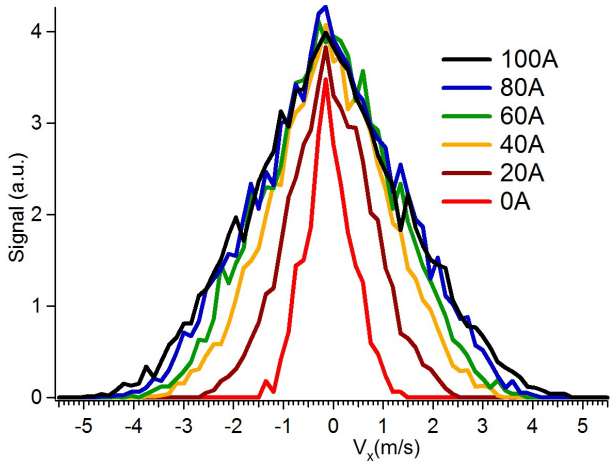

Figure 3.20: The figure shows the radial (along x-axis) velocity distributions of the guided beam at the detector with various guiding currents. The simulations are carried for argon atoms in $^3P_2$ state while the other parameters are kept unchanged. Although the velocity acceptance in the beam gradually increases with the increase in guiding current, the radial velocity in the beam does not increase that much and seems to approach a saturated value since the loss of atoms in the beam also increases with higher guiding current.

number oscillations increases with increasing the guiding current as shown in Fig.3.21(a) and (b). The acceptance in radial velocity also increases with the rise in guiding current as shown in the lower panel of the Fig3.21.

The atoms with negative m_J values (high field seekers) are not guided and consequently crashed on the glass tube. The trajectories of the argon atoms in the $^3P_2$, $m_J = -2$ with a 100A and 20A current in the guiding coil are shown in Fig.3.22. Both for 100A and 20A guiding currents most of the argon atoms in $^3P_2$, $m_J = -2$ state crash within $\sim 20cm$ inside the guide.

The guided beam at various guiding current contains guided particles with various transverse velocities. Which can be seen from the phase-space under the execution of the guiding force. The isoenergic lines in phase-space are shown in the Fig.3.23 for metastable argon atom in $^3P_2$, $m_J = 2$ with 100A guiding current, which indicates the transverse velocity acceptances ($\sim 6m/s$) inside the guide (inside the glass tube). The outer most closed line (with the maximum area) implies that, for a particle which resides inside this bounded region will stay inside through out its evolution. On the other hand, the particles, outside this region will crash on the glass tube during its flight.

The signature of the quadrupole guiding in phase-space is shown in the Fig.3.24. It indicates the conservation in phase-space points in the guided region. With a careful observation, one can see that the final shape of the phase-space after guiding is spiral-like. That can be explained as follows. During the process of guiding the phase-space

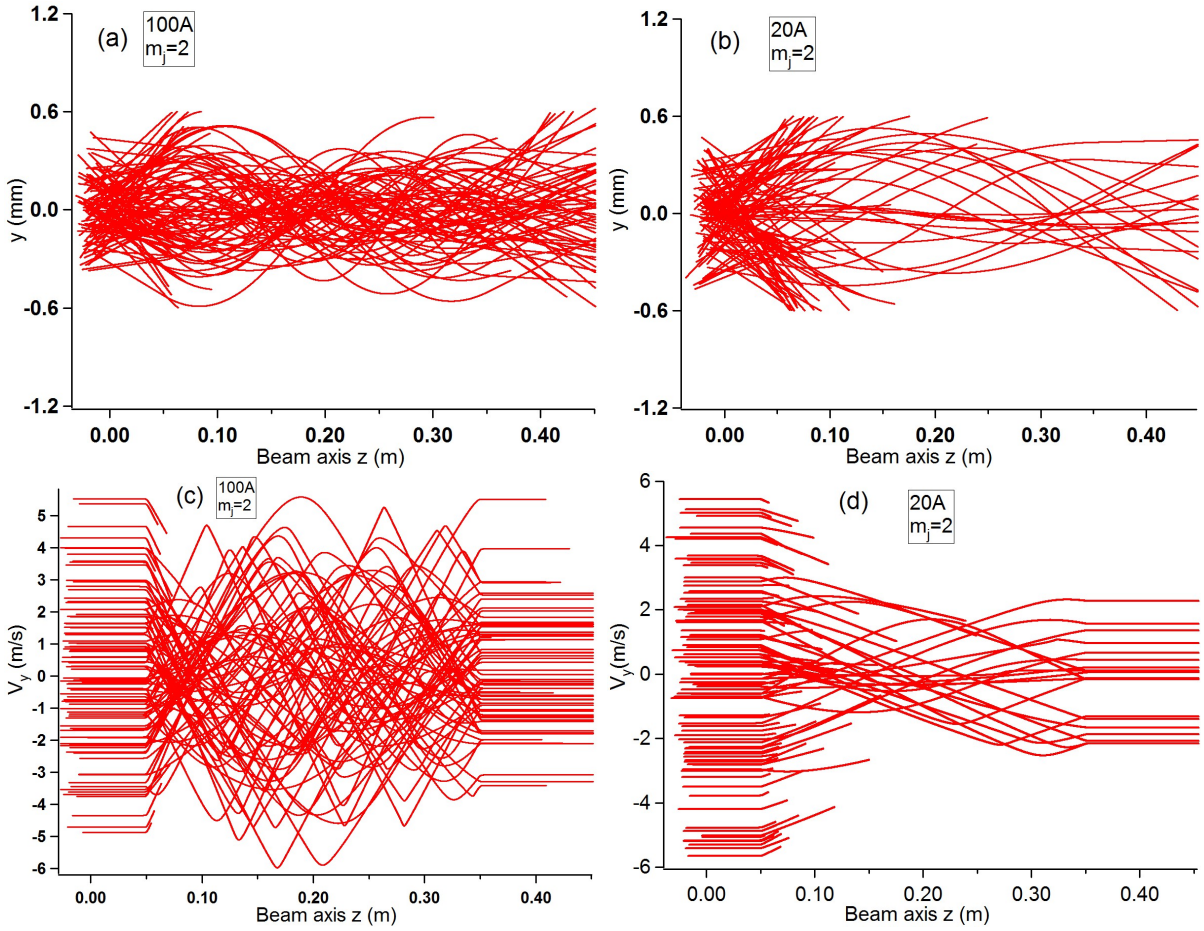

Figure 3.21: The simulated trajectories of the metastable argon atoms ($^3P_2$, $m_J = 2$) along the z-axis (the beam axis) during the course of quadrupole guiding. In the figure, the guide starts at 5cm and ends at 35cm along the z-axis from the skimmer. The effect of guiding on position and velocity along the radial direction (y) are shown in (a) and (c) with 100A, respectively and, (b) and (d) with 20A, respectively.

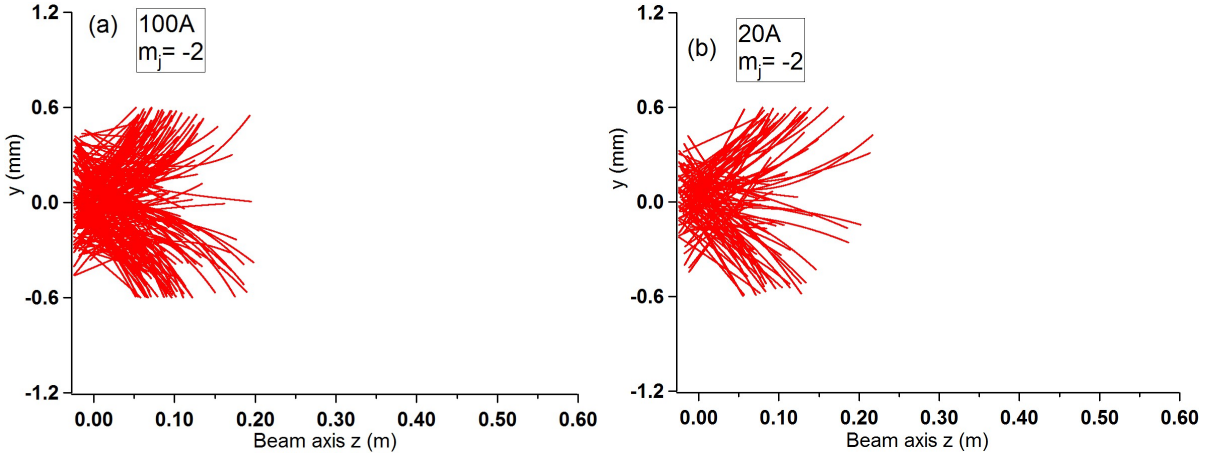

Figure 3.22: The simulated trajectories during quadrupole guiding for the argon atoms ($^3P_2$) in $m_J = -2$ (a) with 100A current and (b) with 20A current in the quadrupole guide.

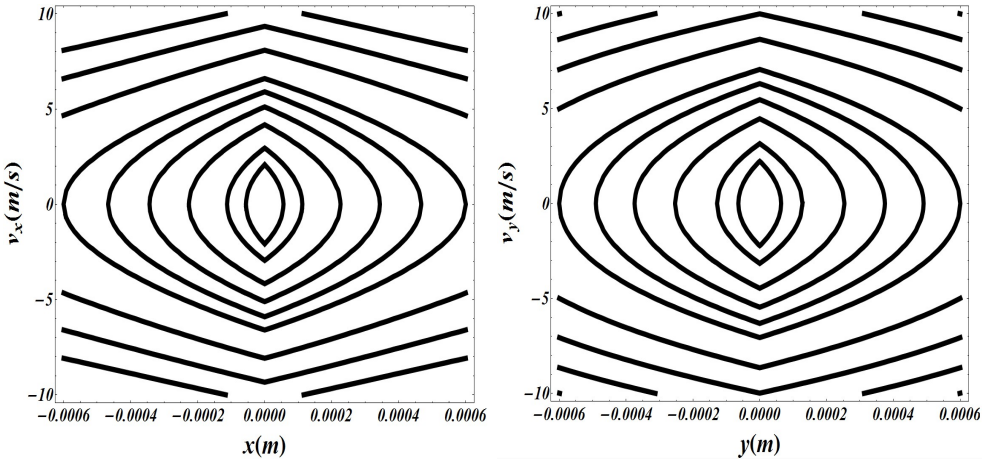

Figure 3.23: The isoenergic trajectories in phase space, calculated for argon atoms in $^3P_2$, $m_J = 2$ metastable state with 100A guiding current in the quadrupole coil, inside the glass tube (diameter 1.2mm).

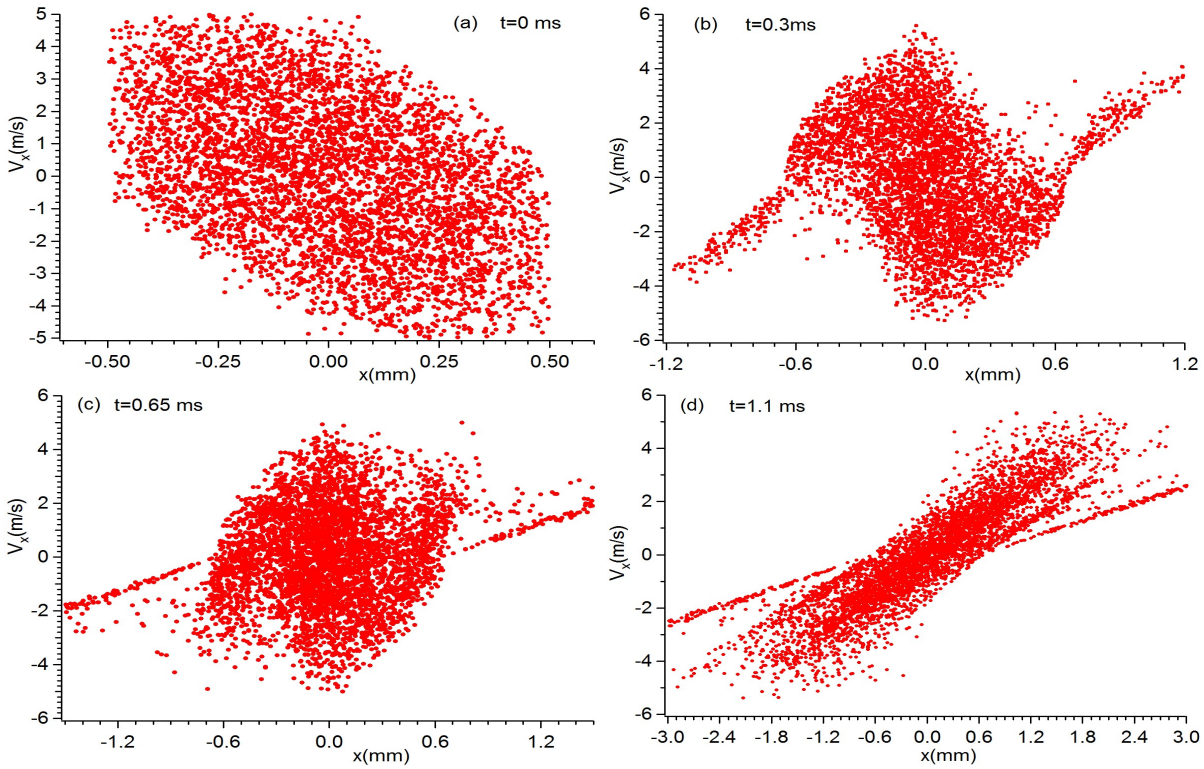

Figure 3.24: The time evolution in phase-space during the course of quadrupole guiding, simulated by 3D-trajectory simulations. The simulations have been carried out for 30cm long guiding of a beam (mean velocity 540m/s and longitudinal velocity spread 80m/s) of metastable argon atoms in $^3P_2$, $m_J = 2$ quantum state and 100A current in the quadrupole guiding coil. The figure (a) represents the phase space distribution of the beam pulse at t=0 (the initial cloud). The figure (b) is corresponds to the evoluted phase space distribution at t=0.3ms. The figure (c) shows the phase space distribution at t=0.65ms, nearly at the exit of the guide and the figure (d) is corresponds to the phase space distribution at t=1.1ms which is close to the detector.

points rotates in a clockwise direction in the phase-space stable region. The phase-space points which are situated at the edge of the trap (with the maximum in position) and have a negligible velocity, move rather slowly than that of the point far inside the trap. So, during the course of evolution these phase-space points lag behind than the others and that finally results a phase-space with a spiral shape.

3.5 Conclusion

In this chapter we have demonstrated the 30cm long quadrupole magnetic guiding of paramagnetic atoms (metastable helium and argon) which has been carried out experimentally.

The magnetic guiding experiments are demonstrated using the beam of metastable helium and argon with various current in the quadrupole guide. The effect of the guiding are indicated by the increment of the MCP signals, generated when the metastable atoms impinge the surface of the MCP. More is the current in the guiding coil more intense is the signal from MCP since, more number of particles (with higher transverse velocity) are guided to the detector. For the argon beam, the integrated signal from the MCP can be increased by ~ 4 times with 100A guiding current than that for the non-guided beam. While for helium beam, the MCP signal is increased by ~ 1.5 times with 100A guiding current than the non-guided beam. The numerical simulations are carried out to verify the guiding effects on the beam. It has been seen from the simulations that the higher guiding current can also induce atom losses due to strong focusing, as it introduces higher transverse velocities. The transverse temperature of the argon beam is $\sim 4.8K$ while for the helium beam it is $\sim 0.2K$ as evaluated from the simulations. The mean velocity and longitudinal temperature are seen to be not affected by the guiding process.

Chapter 4

Deceleration and Trapping of Argon Using Traveling Magnetic Waves

I am among those who think that science has great beauty. A scientist in his laboratory is not only a technician: he is also a child placed before natural phenomena which impress him like a fairy tale. We should not allow it to be believed that all scientific progress can be reduced to mechanisms, machines, gearings, even though such machinery has its own beauty. –Marie Curie

4.1 Introduction

The ultimate control over the various degrees of freedom in gas-phase atoms and molecules has been the long standing dream for the physicists and chemists since the last century. In the last decades the physicists have developed various techniques to produce the translationally cold gaseous ensembles of atoms and molecules [108]. With the discovery of the laser cooling and evaporative cooling, trapping and manipulating atoms have revolutionized the atomic physics, resulting new areas in physics like, study of dilute gases of simple atoms and quantum many body physics [69]. Alike the atoms, the possibilities to investigate the molecular behavior at low temperature motivate physicists and chemists from diverse backgrounds to produce cold and dense molecular ensembles, certainly as an inspiration from the great success of cold atoms. But, unfortunately, the conventional laser cooling techniques does not work for the molecules because of their complicated quantum structures. However, this complex internal structure of molecules are become even more interesting by itself as it offers the properties which are not available with the atoms. Indeed, a source of cold, trapped molecular ensemble holds the promise to open up a completely new regime in physics and chemistry.

The production of cold molecular ensembles are not straightforward as the regular extension of laser cooling technique to molecules is too complicated and cumbersome to realize in the laboratory. Using various properties of molecules, there are at least about ten different methods that have been developed to produce cold molecular ensemble, while the number is increasing rapidly with time. Over the past decade, several powerful techniques have been developed, based on cold ($\sim 1K$) but fast molecules prepared by supersonic expansion. These approaches include various methods based on collisions [171, 172] and the deceleration of supersonic beam exploiting the interactions with optical field [173], inhomogeneous electric [112] and magnetic field [122]. The later two methods exploit the energy shift due to Stark and Zeeman effect in an electric and magnetic field, respectively. In an inhomogeneous field, the quantum states that are shifted to higher (lower) energy as the molecules approach higher field region feel a force towards the region where the field is lower (higher) and the quantum state is referred to low-field-seeking (high-field-seeking) state.

The deceleration using the Stark deceleration technique is applied to a few molecules [174] such as ND_3 [113], CO [112], H_2CO [114], SO_2 [115], and CHF_3 or radicals like OH [116, 117], OD [118], NH [119] etc. which can now be produced with the temperature in the milli-Kelvin range. These molecules are then trapped using electrostatic and magnetic fields [113, 120, 121]. In Stark deceleration the longitudinally inhomogeneous electric field is produced by the use of arrays of electrodes [112], in a static configuration. The introduction of controlled time dependences, by rapidly switching the electric fields

between two static configurations, generates an effective traveling Stark potential well that moves along the molecular beam and is used to reduce the molecular velocity in a quasi-continuous (multi stage) fashion [175].

Based on the similar principle, the Zeeman deceleration technique has been developed to decelerate and manipulate the motion of the atoms and molecules, making use of the Zeeman effect and the inhomogeneous magnetic field produced from the arrays of solenoids [122, 123]. The technique can be extended to long range of atomic and molecular species, with the only requirement that the species has to posses a magnetic moment in either ground state or metastable excited state. Several species like atomic H [122], [176], Ne [124] and molecular oxygen [125] have been decelerated using this technique.

In both these deceleration techniques, the static inhomogeneous electric or magnetic field is used and the deceleration is performed by rapidly switching them between two static configurations to extract kinetic energy form the atoms (or molecules) in the beam. During the deceleration, the electrodes or the solenoids (the field stages) used for the deceleration are also used to periodically focus the atoms (or molecules) in the radial directions. Unfortunately, the radial focusing force for a given longitudinal position differs along longitudinal direction. Due to that, the longitudinal and the radial motions of the atoms (or molecules) are not completely independent. As has been observed, it can led to various phenomenas because of the coupling between the longitudinal and transverse motions which are not expected if one ignores the transverse motion like, low deceleration efficiency at lower rate of deceleration, loss of atoms (or molecules) due to overfocusing at low longitudinal velocity and parametric amplification of the transverse oscillation at a certain longitudinal velocity [129, 177, 178]. Additionally in the Zeeman deceleration, there present a finite rise and fall time ($\sim 5 - 10\mu s$) of the magnetic field pulse (which is $\sim 100ns$ for the Stark decelerator and the effects can be neglected [112]) and has been seen to deplete the deceleration efficiency, although the efforts are being made to optimize this effect [129].

To overcome the above mentioned difficulties constraining the deceleration efficiency, a different mode of operation of the Stark deceleration has also been demonstrated [127, 177], which uses additional transverse focusing field stages. It also requires a larger decelerator. In this mode of operation, the deceleration is carried out by using every third field stage (the pair of electrodes) as the deceleration stage while the two intermediate stages are being used to provide additional transverse focusing force during the deceleration. That increases the deceleration efficiency. In this mode of operation, the focusing along the longitudinal and transverse directions are done by using distinct field stages which effectively decouples the longitudinal and the transverse motions. Among the several other motivations [127, 177], the larger decelerator can increase the deceleration efficiency (longitudinal phase space acceptable area) also, as it allows the less kinetic

energy to be removed per field stage. Very recently, similar mode of operations are also considered for the Zeeman deceleration and the simulations have been shown to increase the deceleration efficiency [129]. Among the other approach, the recent development in Stark deceleration based on chip-decelerator [179] and macroscopic traveling trap [128] are capable of reducing the loss processes and subsequently increasing the phase space acceptance of the decelerator. During the last three years, we have developed a Zeeman decelerator using traveling magnetic waves, that may overcome the major difficulties present in the conventional decelerators (Stark and Zeeman).

In this chapter, we introduce this new technique based on Zeeman deceleration that relies on the genuine movable three dimensional trap. It contains the details of the magnetic field sources, the working principle and the recent proof-of-principle experiments carried out in our laboratory. The structure of the chapter is as follows. In the beginning of the chapter, section.4.2, we introduce the principle of the existing Zeeman deceleration technique to clarify the improvement that may be brought by this new deceleration approach. During this discussion we refer to the principle and particle motions regrading both the Stark and Zeeman deceleration process many times, which is consider to be similar in principle [122, 176]. In the section.4.3, the new approach towards the continuous Zeeman deceleration with genuine three dimensional trapping is discussed. We start with the development of the two different magnetic field sources (mainly differ in topology), capable of producing traveling magnetic waves and finally discuss the one used in the experiment. The section is finished with the discussion on the principle of the deceleration process. The experimental set-up is described in section.4.4. The section 4.5 is dedicated to the proof-of-principle experimental results, supporting simulations and discussions. Finally the conclusion is drawn in section.4.6.

4.2 Zeeman Deceleration: Conventional Approach

The demonstration of multi-stage Zeeman deceleration have been carried out very recently by Vanhaecke and Merkt [122] and subsequently by Raizen and co-workers [123], following the path paved by the development of Stark deceleration technique [180] which has been introduced about a decade ego. In the following, we shall make a brief discussion on multi-stage Zeeman deceleration to introduce the deceleration principle, motions of the atoms (or molecules) during the course of deceleration and the dynamics influencing the deceleration efficiency. Even though the Zeeman decelerator works with different mode of operation than that of Stark decelerator [129], there are common aspects such as the deceleration is achieved by the time dependent switching of the static inhomogeneous fields, the filed stages used for the deceleration, are also exploited to radially confine the atoms (or molecules). The various features of the Zeeman decelerator shall be discussed here also may be considered to be present in Stark decelerator unless mentioned explicitly.

The general principle of Zeeman deceleration is based on the gain in potential energy due to the Zeeman effect when the atoms (or molecules) in a LFS state (see Fig.4.1), enter an inhomogeneous magnetic field and flies to the higher field region. The gain in potential energy is compensated by the loss in kinetic energy (a decrease in velocity). If the magnetic field is sharply (in time) switched off before the atoms leave the magnetic field, the lost kinetic energy is not regained. By repeating this process, a substantial amount of kinetic energy can be extracted which finally leads to deceleration of the atomic beams [123, 176] and eventually bringing to a standstill [181] in the laboratory frame. This technique may be generalized to variety of atoms and molecules than the other existing deceleration technique (Stark deceleration) as it relies on the Zeeman energy shift due to the interaction between the magnetic dipole moment with the applied magnetic field. Because most atoms, radicals and molecules posses magnetic moment either in their ground state or in excited metastable states.

Considering a paramagnetic atom passes through an inhomogeneous magnetic field, $\vec{B}(z)$, it interacts with the magnetic field via Zeeman effect. As a result, the inhomogeneous magnetic field exerts a force $\vec{F}$ on the atoms, such as

$$\vec{F} = -\vec{\bigtriangledown}(-\vec{\mu}_{eff} \cdot \vec{B}(z)) \tag{4.1}$$

The $\vec{\mu}_{eff}$ is the quantum-state-specific effective magnetic moment, includes all the information about how the magnetic dipole precesses around and follows the external inhomogeneous magnetic field. An atom in a LFS state increases its potential energy due to the Zeeman shift (i.e., $E_z(z) = -\vec{\mu}_{eff} \cdot \vec{B}(z)$) as it moves towards the high magnetic field region and slows down. This is the way an inhomogeneous magnetic field exerts a force on the atom and pushes back towards the low field region. In some cases, such as argon

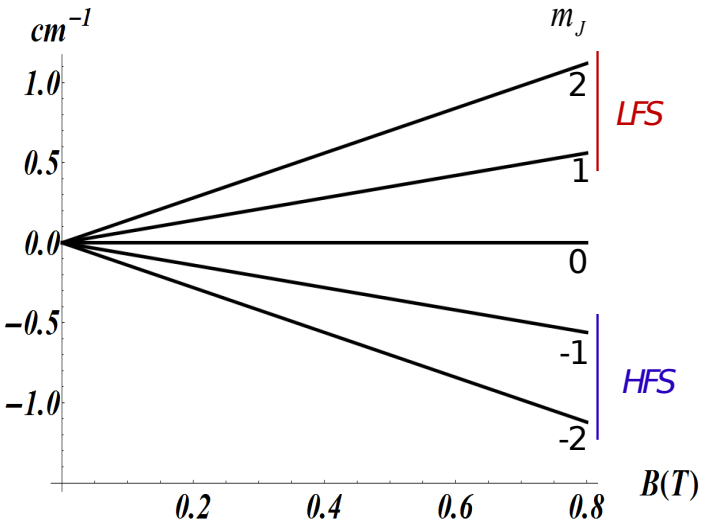

Figure 4.1: The figure shows the Zeeman sublevels of argon atom in $^3P_2$ quantum state. The sublevels (with different m_J values) which increase their Zeeman energy are referred to 'low-field-seeking' states (or as, LFS) and the sublevels which reduce their Zeeman energy are referred to the 'high-field-seeking' states (or as, HFS).

atom in $^3P_2$ state, the Zeeman shift is linear (see Fig.4.1) within the maximum magnetic field achieved in the experiment, which is $\sim 1T$ and the corresponding Zeeman shift is $\sim 1cm^{-1}$ while spin-orbit coupling constant is in the order of $600cm^{-1}$.

Let us consider a paramagnetic atom in a LFS state passing through a magnetic field stage which produces a longitudinally (along z) inhomogeneous magnetic field and has the field maximum at the middle of the stage, as shown in Fig.4.2. The atom increases its Zeeman potential as it moves towards the high field region and reduces its velocity (due to loss in kinetic energy). The maximum reduction in velocity occurs when it reaches the field maximum. But, if we let the atom move further and traverse the whole magnetic stage, it again gains exactly the same reduced velocity. Finally, there is no overall change in velocity. Instead, if we switch off the magnetic field very rapidly before the atom leaves the magnetic field stage, it stays with its instantaneous velocity prior to the time when the applied field is switched off. As it is shown in the Fig.4.2, the maximum loss in kinetic energy ($\triangle E_K^{max} = \triangle E_K^3$) is achieved by switching-off the magnetic field at a time (t_3) when the atom reaches the maximum field position. On the other hand, if we switched off the magnetic field before ($t_1 < t < t_3$) or after ($t_3 < t < t_4$) than for t_3, the loss in kinetic energy will be less ($\triangle E_K^{1,2} < \triangle E_K^3$).

In the multi-stage Zeeman deceleration experiments [122, 123], the magnetic field stages which are used to produce inhomogeneous magnetic field, are solenoids. A simplified scheme of Zeeman deceleration set-up is shown in Fig.4.3. It consists of a beam

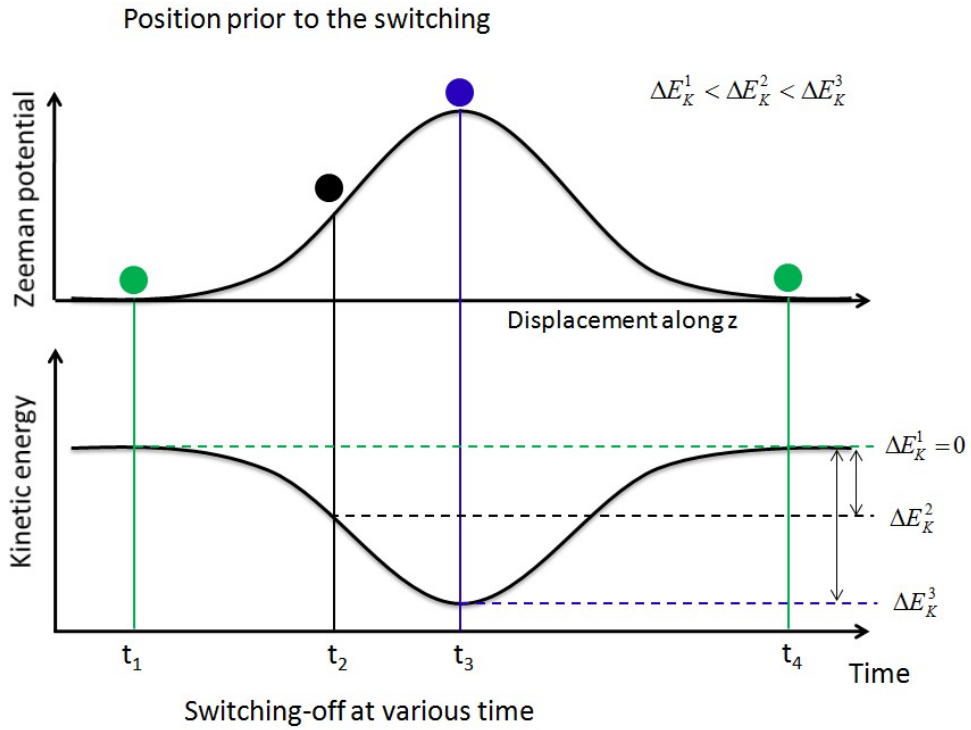

Figure 4.2: The change in kinetic energy of a paramagnetic atom in LFS state, while passing through a potential hill produced by longitudinally inhomogeneous magnetic field (from a solenoid), is shown. Depending on the moment at which the magnetic filed is sharply (in time) switched off when the atom passes through the magnetic field stage, the change in kinetic energy varies from $\triangle E_K^1 = 0$ (the case when we let the atom pass through the magnetic field stage without switching off the field) to the maximum $\triangle E_K^{max} = \triangle E_K^3$. The maximum change in kinetic energy $\triangle E_K^{max}$ occurs when the field is switched off at a time (t_3) when the atom reaches maximum filed position which is $\triangle E_K^3$ in the figure. If the field is switched before ($t_1 < t < t_3$) and after ($t_3 < t < t_4$) the time t_3, the change in kinetic energy is less. Essentially, the magnitude of change in velocity depends on the position of the atom in the magnetic field stage at the moment when the field is sharply switched off.

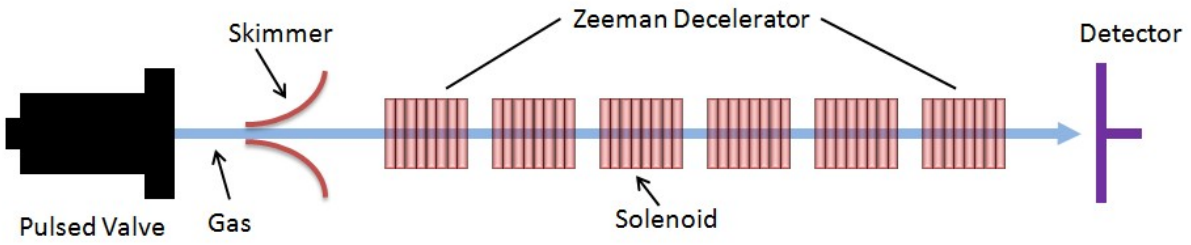

Figure 4.3: The schematic representation of a multistage Zeeman decelerator. The set-up consists of a source of a atomic and molecular (the pulsed valve), the array of magnetic field stages (the solenoids) and the detection apparatus.

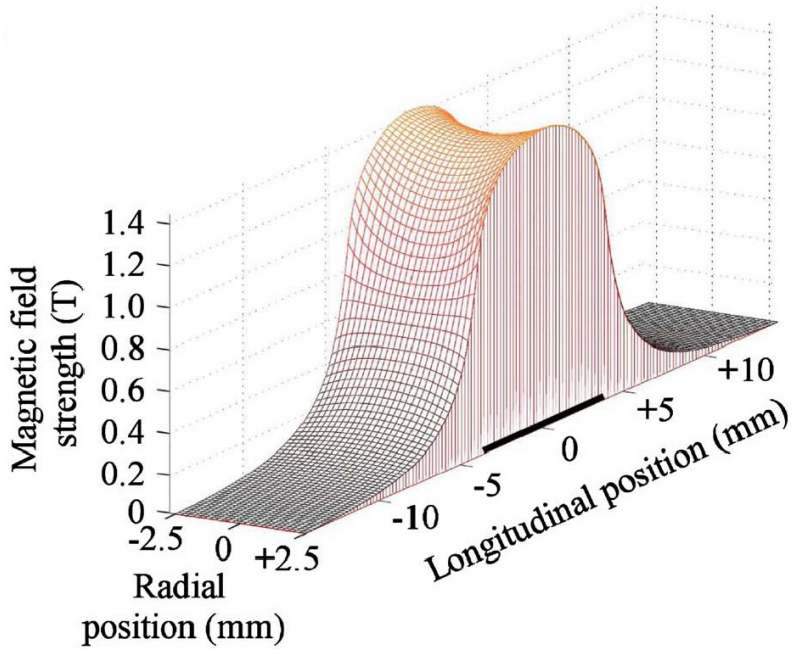

Figure 4.4: The magnetic field profile inside a solenoid with 250A current while the position of solenoid is indicated by the thick black line on the longitudinal position axis. For more details and the specifications of the solenoid, see [176].

machine to produce a supersonic beam, the magnetic field stages (the solenoids) and the detection apparatus. During the deceleration process, high pulsed current is driven in the solenoids which produces a high magnetic field . For example, in the Zürich-experiment [176], a magnetic field peak of $\sim 1.4T$ is achieved with $250A$ with rise and fall times of the magnetic field is $5\mu s$ and the length of the current pulse is few tens of microseconds. In the Texas-experiment, $\sim 5.2T$ magnetic field peak is achieved with $750A$ [124] and the exponential rise and decay of the magnetic field with the time constant are in the order of $17\mu s$ and the length of the current pulse is in the order of 100 microseconds. The magnetic field geometry inside the solenoid is presented in Fig.4.4 (a detailed discussion can be found in [176]). The solenoids (which are placed coaxially with the beam axis along the direction of propagation of the beam) are divided into two sets as *odd solenoids* (i.e., the first, third, fifth solenoid and so forth) and *even solenoids* (i.e., the second, fourth, sixth solenoid and so forth). The solenoids in each set are connected in series and are rapidly switched alternatively, during the deceleration process. A scheme of the Zeeman deceleration principle is shown in Fig.4.5.

When the atoms (in LFS) approach the decelerator, the *odd solenoids* are switched-on. Due to the positive Zeeman shift, the atoms continuously lose their kinetic energy as they enter the first solenoid. A certain time later, the *odd solenoids* are turned-off before the atoms reach the field maximum of the first solenoid. After $\triangle t$ time from the switching-off, the *even solenoids* are switched-on and again are switched-off before the atoms reach the field maximum of the second solenoid. The process is repeated until the atoms leave the decelerator. The amount of kinetic energy/stage can be extracted from the atoms depends on how long distance we let the atoms traverse the Zeeman potential which is essentially determined by the time at which the field is switched-off (see Fig.4.2). Eventually, by tunning the $\triangle t$ which is the time difference between the switching-off of the *odd solenoids* and the switching-on of the *even solenoid*, one can decide to decelerate, longitudinally guide and accelerate a bunch of atoms in a beam. In the case longitudinal guiding where mean velocity of the initially captured atoms in the decelerator, have the same mean velocity when they exit the decelerator. The time sequence of switching between the two set of solenoids is constant ($\triangle t = constant$) which does not vary with time. But in the case of deceleration (acceleration), the atoms pass through the solenoids and their velocity need to be reduced (risen) so, the time sequences of switching on and switching off between the two sets of solenoids change with time ($\triangle t = s(t)$, where $s(t)$ includes the time dependence including rising and falling time of the magnetic field [176, 182]). The time sequences are applied such that the particles loose a fixed amount of kinetic energy per field stage (the solenoid).

As we already mentioned, the amount of kinetic energy lost by an atom (in LFS) depends on its position along the beam axis prior to the time at which the magnetic field

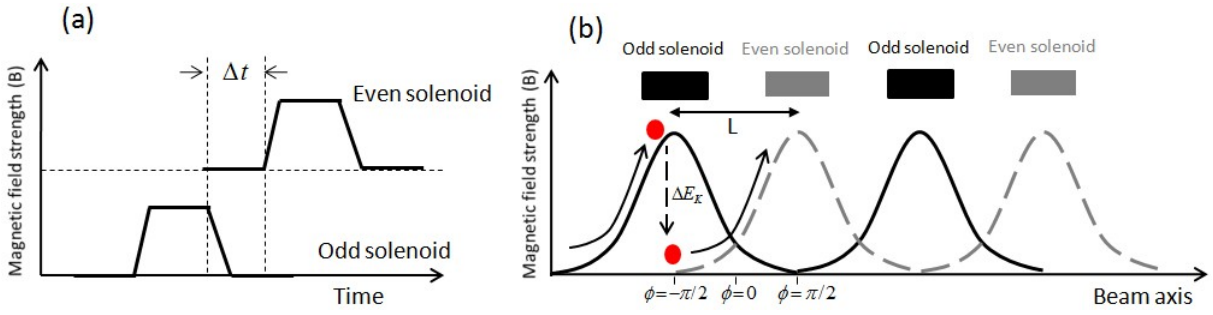

Figure 4.5: The figures represent the generalized principle of Zeeman deceleration. The figure on the left (a) shows the magnetic field pulse sequence (i.e., the current pulse sequence) during the deceleration and longitudinal guiding operation. The $\triangle t$ represents the time difference between switch-off of the *odd solenoids* and the switch-on of the *even solenoids*. The $\triangle t$ is constant for the case of longitudinal guiding (with $\phi_0 = 0$, see text) while it is time dependent during the deceleration (acceleration) process. The figure is adopted from [176]. The figure on the right (b) shows the variation of magnetic field strength when the current is flown in one set of solenoids with the other set switched-off and vice versa. The center-to-center distance between two adjacent solenoids is L. The position is designated with the phase angle ϕ. ϕ is defined to be zero at the position between two adjacent solenoids and $\phi = \pi/2$ ($\phi = -\pi/2$) corresponds to the center of the next (previous) solenoid where the magnetic field strength is maximum when it is active. The deceleration is carried out by rapidly switching the odd and the even solenoids with smoothly varying (increasing) the $\triangle t$ in time t. The amount of the kinetic energy $\triangle E_K$ removed from an atom depends on its position ($\phi = \phi_0$, see text) at the time when the field is rapidly switched off.

is switched-off. Due to the spatial periodicity of the decelerator and the periodicity of the deceleration process, this position is expressed in terms of a phase angle ϕ [176, 182, 183] rather than a spatial coordinate. As has been shown in the Fig.4.5, the position at the middle of two adjacent solenoids is denoted with $\phi = 0$ and a phase angle $\phi = \pi/2$ ($\phi = -\pi/2$) corresponds to center the next (previous) solenoid where the magnetic field strength is maximum when it is active. The switching sequence for a deceleration process are calculated by defining an equilibrium phase angle ϕ_0 and an initial velocity v_0 corresponding to a synchronous atom which keeps its phase angle ϕ_0 unchanged at a moment each field stage is switched-off throughout the deceleration process. If we assume that the current flowing in the solenoids are identical and they can be switched instantaneously, the synchronous atom always travels an equal distance L (which is the distance between adjacent solenoids) and consequently reduces equal amount of kinetic energy within the time interval between the switching-off of the adjacent solenoids. With this approxima-

tion, the kinetic energy lost per stage $\triangle E_k(\phi_0)$ (see Fig. 4.7) by a synchronous atom is the potential energy difference which is $E_z(\phi_0) - E_z(\phi_0 - \pi)$. The $E_k(\phi_0)$ is the Zeeman energy at the axial position corresponds to $\phi = phi_0$. The $\triangle E_k(\phi_0) \approx E_z(\phi_0)$ to a good approximation [129]. When the change in velocity is small compared to the v_0, the loss in kinetic energy of the synchronous atom can be considered as is due to the execution of a continuously acting average force $\bar{F} = -E_z(\phi_0)/L$.

As the average kinetic energy/stage can be extracted from a synchronous atom (molecule) is very small ($\triangle E_k(\phi_0) \sim 1cm^{-1}$) due to small shift in Zeeman energy while the typical order of the kinetic energy in a beam is $\sim 100cm^{-1}$, an efficient deceleration and stopping of an atomic (molecular) species demands a large number of magnetic field stages. The required number of field stages is determined by $mv^2/(2\triangle E_k(\phi_0))$ where m and v are the mass and initial velocity of the atom, respectively. For instance, the deceleration of H atom from 520m/s ($11.3cm^{-1}$) to 100m/s ($0.4cm^{-1}$) has been demonstrated using $\phi_0 = 50°$ with 12-stage decelerator [126] while for oxygen molecules, to reduce the velocity from 389m/s ($202.4cm^{-1}$) to 83m/s ($9.2cm^{-1}$) using $\phi_0 = 63.2°$, it requires 64 magnetic field stages [125].

For a supersonic beam, there exists non-zero velocity spreads both along the longitudinal and the transverse (radial) directions (along with a finite spatial spread). So, one needs to care for the radial confinement during the course of deceleration. The efficiency of the deceleration depends on the ability to keep bunch of the atoms (or molecules) radially confined and repetitively extract the kinetic energy as they pass through the field stages. This is well described by phase stability of the process as has been introduced for charge-particle accelerator[184], Stark decelerator [182] and Zeeman deceleration [129].

4.2.1 Longitudinal Motion and 1D Phase Stability

A synchronous atom keeps its phase ϕ_0 unchanged when each field stage is switched-off as it moves through the decelerator. But, for a non-synchronous atom having initially same phase angle but slightly higher (lower) velocity than the synchronous atom's velocity (v_0) will move further (lag behind) into the solenoid than the synchronous atom prior to the time when the field is switched-off and gets decelerated more (less) than the synchronous atom. And, continue to increase (decrease) its phase angle, over one or several field stages, until it reduces (increases) it velocity to v_0. Then the atom will start loosing (gaining) its phase angle relative to the synchronous atom until it reaches the ϕ_0, but this time the velocity will be lower (higher) than the synchronous atom and the reverse process will take place. So, the atoms with slightly different phase angles and velocities than ϕ_0 and v_0, respectively, oscillate both in phase and velocity around ϕ_0 and v_0. These atoms are called to be trapped in the frame moving with the velocity of the synchronous atoms.

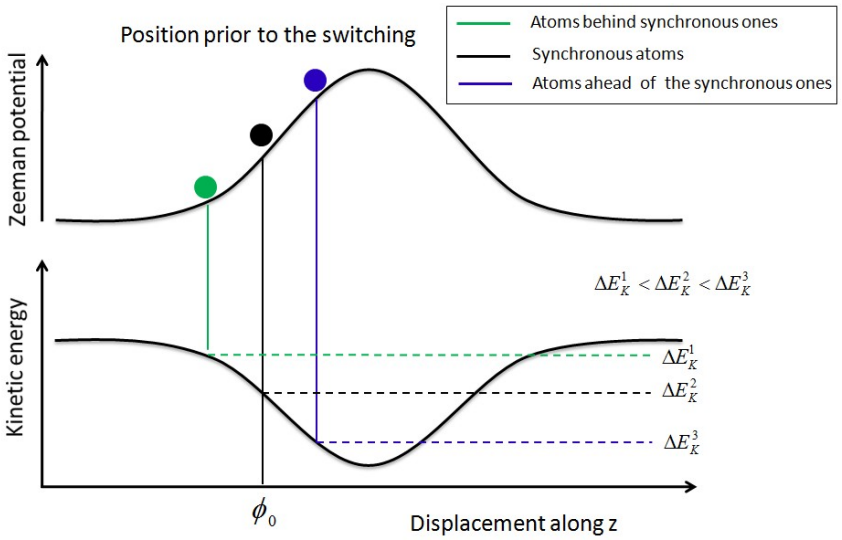

Figure 4.6: A synchronous and non-synchronous atoms moving on a Zeeman potential hill produced by a longitudinally inhomogeneous magnetic field $B(z)$. The atoms which are ahead and behind (in blue and green) than the synchronous atom (in black) loss more and less kinetic energy, respectively and results in longitudinal focusing.

These are well explained with the help of phase-space as described in charged-particle accelerators [184], in Stark decelerator [180, 185] and in multi-stage Zeeman decelerator [129] where the trapped particles shall evolve in time with the trajectories which always stays inside the phase stable area, determined by the last closed equipotential trajectory which is also called the *'separatrix'* [175]. The acceptance in velocity of the decelerator depends on the potential depth, also called the trap depth such that the particle with these velocities can oscillate around the synchronous particles without being lost from the decelerator.

For a non-synchronous atom with a phase $\phi(t) = \phi_0 + \delta\phi(t)$ and the velocity $v(t) = v_0 + \delta v(t)$ (where ϕ_0 and v_0 are the phase angle and the velocity of the synchronous atom, respectively), the loss in kinetic energy per stage can be written as $\triangle E_z(\phi) = \triangle E_z(\phi_0 + \delta\phi)$ as long as $\delta v \ll v_0$. Then the equation of motion of the non-synchronous atoms relative to the synchronous atom becomes,

$$\frac{mL}{\pi}\frac{d^2\delta\phi}{dt^2} + \frac{1}{L}\left[\triangle E_z(\phi_0 + \delta\phi) - \triangle E_z(\phi_0)\right] = 0 \tag{4.2}$$

with m is the mass of the atom and the L is the distance between two adjacent solenoids.

Using this equation of motion, a phase space plot can be carried out to see that non-synchronous atoms can follow the stable oscillations around the synchronous atoms, provided with the condition that the kinetic energy of the atoms are not greater than the height of the Zeeman potential well [175]. In the Fig.4.7 the phase stability diagrams (the

details of the calculation are given in [129]) of a multi-stage Zeeman deceleration of D atom is shown for various equilibrium phase angles.

From the Fig.4.7 it can be noticed that, by rising the equilibrium phase angle for deceleration from $\phi_0 = 0$ to $\phi_0 = \pi/3$ the phase-space accepted area (defined by the separatrix) is lowered. Similar as in charged particle accelerator [184, 186] and Stark decelerator [175], more is the equilibrium phase angle used for the deceleration less will be the acceptance in phase-space. So, one has to make a compromise between the phase angle used for the deceleration and the phase-space acceptance of the decelerator. For instance, in the Zeeman deceleration experiment of H atom [176] a phase angle of 55° has been used with maximal current of 250A, which is capable to reduce $0.63cm^{-1}$ average kinetic energy per stage while in the Zeeman deceleration of molecular oxygen [125] experiment, a phase angle of 63.2° has been introduced to decelerate from 389m/s to 83m/s using 64 magnetic field stages.

4.2.2 Transverse Motion and 3D Phase Stability

In a supersonic beam of atoms (or molecules), there always exists a transverse velocity spread. Since the magnetic field inside the solenoid (which is cylindrically symmetric in the radial direction) is maximum close to the inner surface of the solenoid, the field pushes the atoms (in LFS) toward the beam axis which results in a transverse oscillatory motion around the beam axis z, which leads to the effective radial confinement during the deceleration process. The magnetic field geometry resulting from a solenoid is shown in Fig.4.4. For a given longitudinal position, the on-axis field strength has the smallest value inside the solenoid while the on-axis field strength has the highest value outside the solenoid. The radial focusing force varies for different given longitudinal positions. For the atoms, inside the solenoid, located off-axis but closer to the center of the solenoid, are tightly focused than the atoms located off axis but far from the center of the solenoid. Even, the atoms are slightly defocused in the radial direction outside the solenoid [176]. So, the actual transverse force exerted on the atoms depends on its position and time as well as on the equilibrium phase angle used for the deceleration and can be expressed in terms of an averaged force which is obtained by integrating over one period of the decelerator.

The effect of the transverse motion in the deceleration process, considering the variation of the radial focusing force along the longitudinal direction, in the decelerator, can be seen from the middle column of the Fig.4.7. In the phase-space correspond to the low ϕ_0 value, there appears unstable regions in the phase-space centering around the synchronous atom as well as in an almost closed ring which is located immediately inside the separatrix. The non-accepted area in the phase-space however, decreases with the

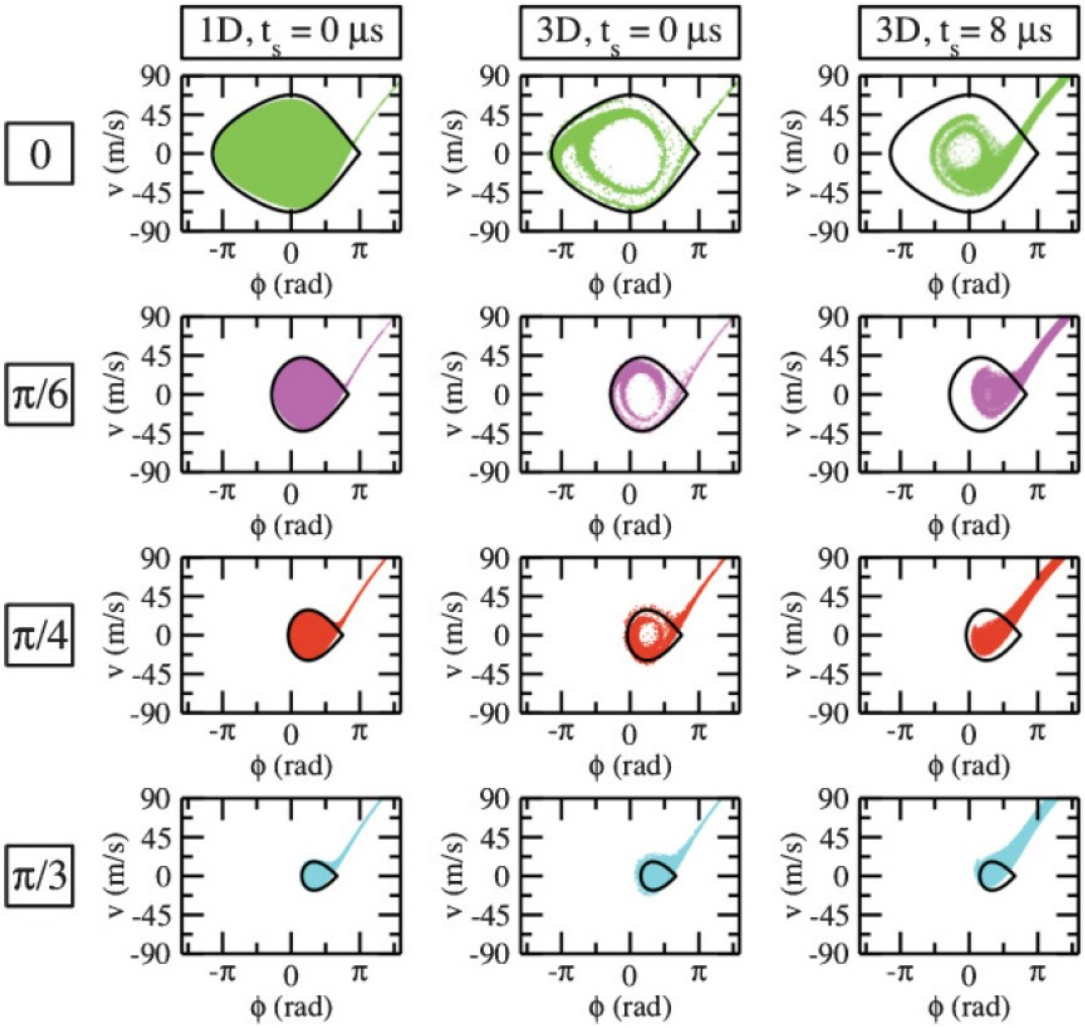

Figure 4.7: The simulated phase-space diagrams for multi-stage Zeeman decelerator with various equilibrium phase angle ϕ_0, adopted from [129]. The phase-space diagrams corresponds to selected values of ϕ_0 as indicated in left insets (increasing from top to the bottom) and the bold line in each diagram shows the separatrix calculated from Eqn.4.2. The diagrams in the left column are correspond to one-dimensional (longitudinal) particle trajectory simulations which assumes instantaneous switch-off of the current (i.e., $t_s = 0$ where $t - s$ is the switch off time). The diagrams in the middle column represents the three-dimensional trajectory simulations which also assumes $t_s = 0$. In the right column, the diagrams represent the three-dimensional trajectory simulations but with $t_s = 8\mu s$ (see text).

increase in ϕ_0 value. At the low value of ϕ_0, the appeared non-accepted area near to the synchronous atom is because of the fact that the atoms moving off-axis but close to the synchronous atom hardly experience any radial focusing force (even can experience a radial defocusing force due to the convex shape of the transverse magnetic field distribution outside the solenoid). The non-accepted area immediate inside the separatrix arises because the atoms which are located close to the high-phase-angle turning point (which is near to the center of the active solenoid) experience a strong transverse focusing force. As a result, they acquire a transverse velocity which is too large to be compensated any more and finally are lost from the decelerator.

With the increase in equilibrium phase angle ϕ_0, the synchronous atom is moved further inside the solenoid where the transverse force is higher than that of $\phi_0 = 0$. So, the minimum phase angle difference to the synchronous atom which is required to compensate the transverse motion, reduces. As a result, the non-accepted phase space area centering the synchronous atom decreases with the increase in equilibrium phase angle ϕ_0, even it completely disappears for $\phi_0 > \pi/4$.

In the case of Stark decelerator, the effect of transverse motions are extensively studied [185] and has been found that at low ϕ_0 value the molecules which closely oscillate around the synchronous molecule are underfocused due to insufficient radial confining force, resulting in the non-acceptable area centering the synchronous molecule. A non-accepted phase space area close to the separatrix (often called 'halos' [187]) also has been observed in Stark decelerator, is because of the parametric amplification (see Fig.4.8) resulting from coupling between the longitudinal and transverse motion. The oscillation frequency both for the longitudinal and the transverse motions of the molecule depends on the initial longitudinal position in phase space (see Fig.4.8). The longitudinal oscillation frequency is maximal near to $\phi = 0$ and reduces to zero on the separatrix, while the transverse oscillation frequency is minimal at $\phi = 0$ and increases with the increase in phase angle. When the longitudinal and transverse oscillation frequencies become close, the parametric amplification occurs and that leads to an unstable operation of the decelerator.

4.2.3 Finite Switching Time and 3D Phase Stability

The effect of the finite switch-off time ($t_s \sim 8\mu s$) of the current in the solenoids has significant effect in the multi-stage Zeeman deceleration (the effect is negligible for Stark decelerator [112] as the $t_s \sim 100ns$), as has been shown in the right column of the Fig.4.7. As in the Zeeman deceleration, the equilibrium phase angle, ϕ_0 is considered at the moment when the current switch-off process is initiate, even though the atoms continue to experience a field gradient and decelerated during the switching-off process and experience a higher (effective) phase angle. That is why, the decelerated atoms results

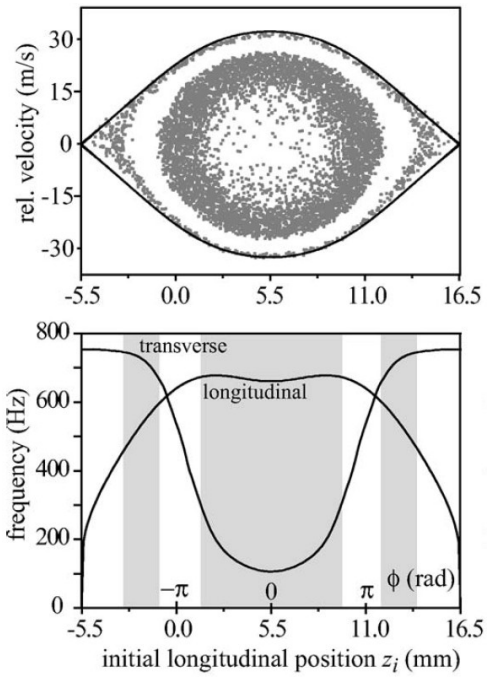

Figure 4.8: The longitudinal and transverse oscillation frequency of OH radical in $X^2\Pi_{3/2},\ v = 0,\ J = 3/2,\ M_J\Omega = -9/4$ state as a function of the initial longitudinal position z_i in the first electric field stage of the Stark decelerator, adopted from [187]. The decelerator is operated at $\phi_0 = 0$ (longitudinal guiding). The upper figure represents the phase space acceptance while the lower figure shows the variation oscillation frequency. The indicated gray area in the lower figure corresponds to the initial longitudinal phase space positions that lead to the stable trajectories in the decelerator. The white area, in the lower figure, indicates the region where the transverse and longitudinal frequency become close, leads to parametric amplification and results an empty space (or the halo) near the separatrix as shown in the upper figure.

a smaller phase space accepted area (at least for three lower phase angle in Fig.4.7) and smaller non-accepted area centering the synchronous atom due to the transverse motion, compared to the case which considers $t_s = 0$.

4.2.4 Remarks

All these effects discussed above are responsible to lower the deceleration efficiency of the decelerator. That is why, various different modes of operation of the multi-stage deceleration are proposed and some of them are being used for both Stark [127] and Zeeman decelerators [129] to increase the efficiency. The other important point is that the decelerated atoms (or molecules) cannot be trapped (in the laboratory frame) inside the decelerator itself as it does not provide a real 3D-trap. The atoms (or molecules) are generally trapped in a magnetic or electric trap after the deceleration is done where the trap is installed at a distance from the decelerator. That may introduce a phase space mismatch between the bunch of decelerated atoms and the trap due to the free flight of the atoms from the end of the decelerator to the trap. This also leads to a loss of atoms. In the Zeeman decelerator, during the switch-off of the solenoids, the magnetic field can pass through a near-zero value (which mainly depends on $\triangle t$). The atoms pass through the near-zero magnetic field are redistributed into various Zeeman sublevels (e.g., for H atoms, the population redistributed over m_F sublevels of $F = 1$ hyperfine state) with the probability which varies with the $\triangle t$, due to the Majorana transition [176]). Nevertheless, the non-zero magnetic field can be maintained by imposing a temporal overlap in the field pulses between the adjacent solenoid.

These above mentioned difficulties are present in both the Stark and Zeeman decelerators as they arises because of two reasons, (a) the field stages that are used for deceleration, are also used for the radial confinement and, (b) the deceleration operation is carried out by time dependent (or time independent, in the case longitudinal guiding) switching of the static inhomogeneous fields.

To get rid of these inevitable difficulties, one has to consider a different deceleration method with different field source where first, the fields responsible for manipulating the longitudinal and the transverse motions are decoupled and second, the field can be varied in a continuous fashion, on which the discussion will be made in the next section.

4.3 Zeeman Deceleration: Our Approach

Since the observation of the constraints on the deceleration efficiency of Stark decelerator (and in Zeeman decelerator as well) depending on various technical and systematic reasons [127, 185, 187], few approaches have been made towards the new generation decelerators, to improve the deceleration efficiency. For example, a Stark decelerator has been demonstrated which is operated in a different mode to reduce the loss of molecules due to the transverse motional coupling with the longitudinal motion, by introducing additional transverse focusing stages [127]. With this operation mode, a higher phase space acceptance of the decelerator can be achieved. Another significant development has been made on Stark decelerator, very recently, which uses traveling electric potential [128] by extending the idea of previously demonstrated chip decelerator [179].

Similarly in the case of Zeeman decelerator, an improved version has recently been demonstrated in our laboratory which is capable of decelerating paramagnetic atoms (and molecules) using genuine traveling magnetic waves. The atoms are confined in a real movable three-dimensional trap throughout the deceleration process which is expected to provide a higher acceptance than the currently operating Zeeman decelerators [122, 123]. The major improvement has been made by introducing a magnetic field source which is able to produce traveling magnetic waves. In this section, we thoroughly discuss the development of such a kind of magnetic coils as have been carried out in the laboratory.

4.3.1 The Helical Wire-Geometry

As the first step towards the new magnetic field source, one can think of a coil which is a manipulated solenoid. If one pulls the two edges of a solenoid, the resulting coil is called the helical coil. Let us consider such a helical coil with radius r and the periodicity λ as is shown in the left panel of the Fig.4.9. A wire can have positive (negative) helicity if it rotates anti-clockwise (clockwise) with the displacement along the positive z-axis. Throughout this discussion we consider the direction of the current flow is (negative) positive if and only if it has a current component along the (negative) positive z-direction. Following the geometry, the radial components (x and y) of the magnetic field on the coil axis (z) are expected to be periodic along z-axis while the on-axis field vector along z acquires a constant value.

4.3.1.1 One wire helical coil

For a helical coil made up of one wire (let say *wire 1*) with the parametric equations $x = rcos\theta$, $y = rsin\theta$ *and* $z = \lambda\theta/2\pi$ the field components can be calculated using Biot-Savart law as,

$$b_x(x,y,z) = \frac{\mu_0 I}{4\pi}\int d\theta \frac{\lambda y/(2\pi) + rzcos\theta - (r\theta\lambda cos\theta)/(2\pi) + (r\theta\lambda sin\theta)/(2\pi)}{[(z-\theta\lambda/(2\pi))^2 + (x-rcos\theta)^2 + (y-rsin\theta)^2]^{3/2}} \tag{4.3}$$

$$b_y(x,y,z) = \frac{\mu_0 I}{4\pi}\int d\theta \frac{\lambda x/(2\pi) + rzsin\theta - (r\theta\lambda sin\theta)/(2\pi) - (r\theta\lambda cos\theta)/(2\pi)}{[(z-\theta\lambda/(2\pi))^2 + (x-rcos\theta)^2 + (y-rsin\theta)^2]^{3/2}} \tag{4.4}$$

$$b_z(x,y,z) = \frac{\mu_0 I}{4\pi}\int d\theta \frac{(rcos\theta)^2 - rxcos\theta - rysin\theta + (rsin\theta)^2}{[(z-\theta\lambda/(2\pi))^2 + (x-rcos\theta)^2 + (y-rsin\theta)^2]^{3/2}} \tag{4.5}$$

where $\mu_0 = 4\pi \times 10^{-7}\ N.A^{-2}$, is the vacuum permeability and I is the positive current flowing in the coil. The magnetic field has been calculated with the parameters, $r = 1.5mm$, $\lambda = 11.6mm$ and current $I = 300A$ and shown in the right panel of the Fig.4.9.

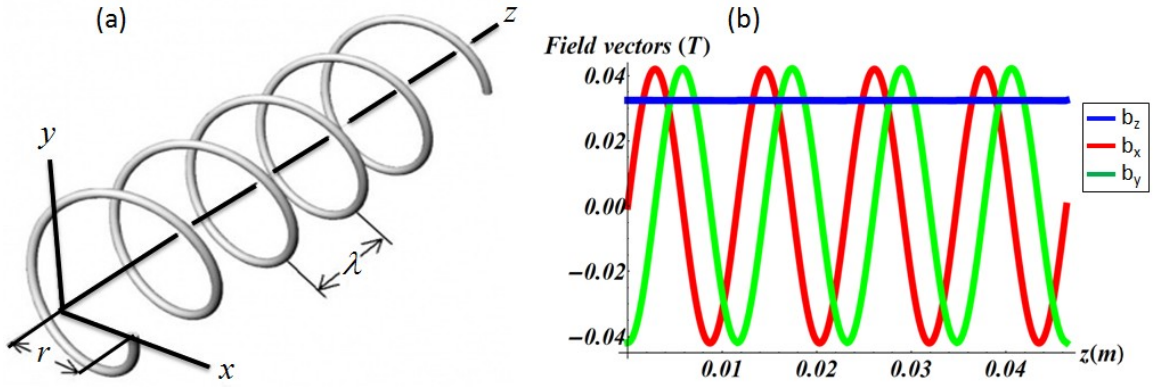

Figure 4.9: On the left panel of the figure, (a) represents a helical coil (with radius r, and periodicity λ) which can be realized by stretching a solenoid along its axis. On right panel, (b) the three magnetic field components on the coil axis, along x, y and z axis, have been calculated with $r = 1.5mm$, $\lambda = 11.6mm$ and current $I = 300A$. The component along z, acquires a constant value (0.032 T) while the components along x and y are sinusoidal with the amplitude of 0.042T. One must note that, the x and y-components of the field are calculated in (x,0,z) and (0,y,z)-planes, respectively.

We are mainly interested in the field geometry inside a small cylindrical volume with radius $0.6mm$ which is coaxial with the coil, as we intend to use the field inside a glass tube of this dimension, as will be clear later. Hereafter, we shall present the calculations which contains the informations of the fields only in this small volume.

The variation magnetic field vector b_z in the (0,y,z)-plane is shown in the Fig.4.10. Far from the coil axis the z-component oscillates periodically and the amplitude increases with the distance far from the coil axis. It can be understood as follows. As seen from the coil

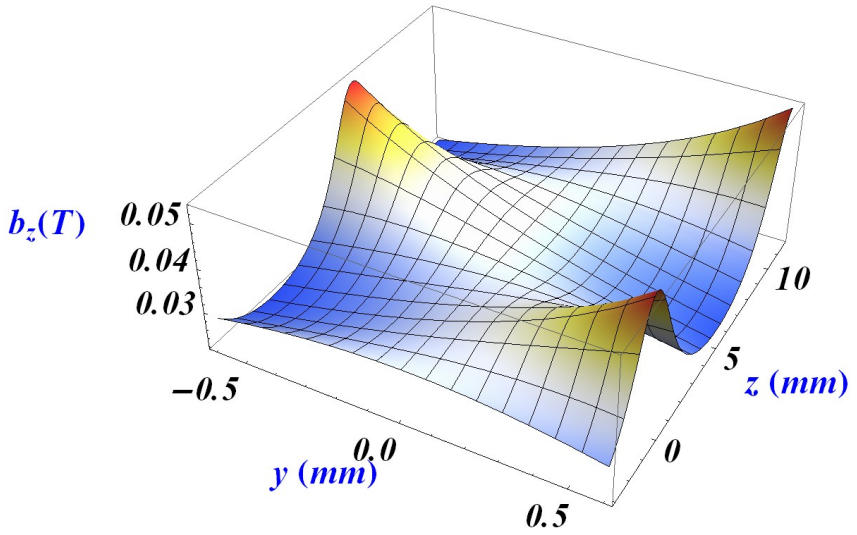

Figure 4.10: The figure shows the variation of the magnetic field component b_z along z, in (0,y,z)-plane. The field has been calculated with $r = 1.5mm$, $\lambda = 11.6mm$ and current $I = 300A$. In (0,y,z)-plane b_z acquires a constant value (0.32 T) on the z-axis while far from the axis, it oscillates.

axis, the differential element of the wire revolves around the axis with a constant radius (r) and the direction of the conventional current (the tangent) has always, a constant angle (which in fact, is defined by λ) with the coil-axis. So, the contribution to the field b_z on the axis averaged out properly and becomes constant (nearly constant for a finite coil) which is not the case far from the coil axis. In the Fig.4.11, the variation of the x-component of the magnetic field vector (b_x) in (0,y,z) and (x,0,z)-planes, are shown.

The field vector components (b_x, b_y *and* b_z) can be imagined in the other planes containing the coil axis, as they are inter-related through joint operations by translation and rotation in the radial plane. For example, $b_z(0, y, z)$ is same to the field $b_z(-x, 0, z + \lambda/4)$ with a rotation of $\pi/2$, can be summarized along with the other components as,

$$b_z(-x, 0, z + \lambda/4) \xrightarrow{\pi/2} b_z(0, y, z) \tag{4.6}$$

$$b_y(0, y, z + \lambda/4) \xrightarrow{\pi/2} b_x(x, 0, z) \tag{4.7}$$

$$b_y(-x, 0, z + \lambda/4) \xrightarrow{\pi/2} b_x(0, y, z) \tag{4.8}$$

A helical coil can be made up of two or more wires each having the helical geometry, instead of one wire (see for example, Fig.4.12). By doing this, an on-axis sinusoidal magnetic field can be produced.

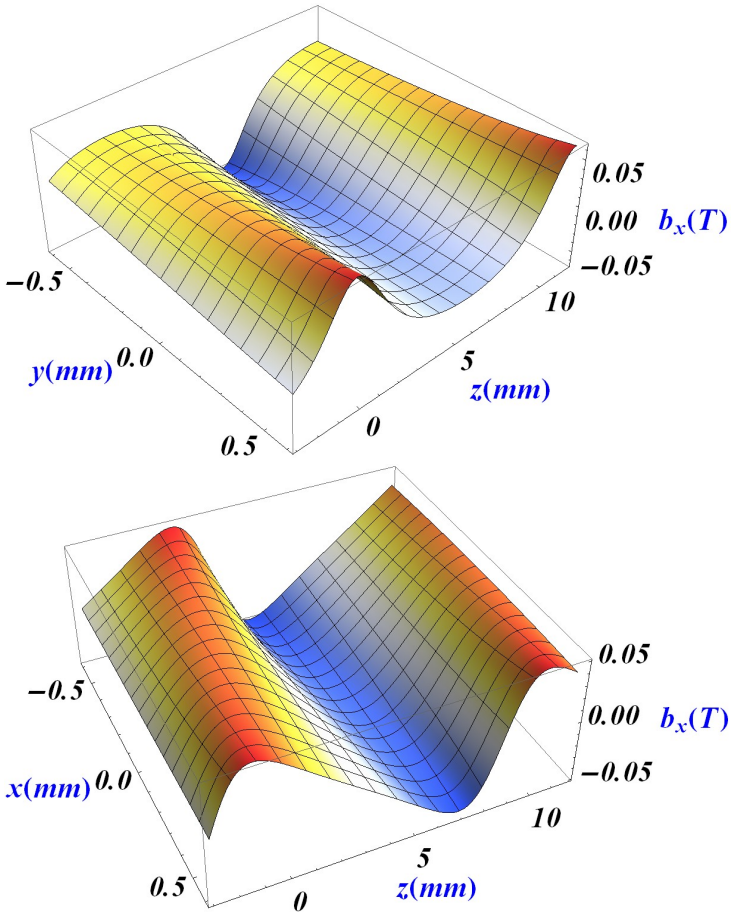

Figure 4.11: The figure on the upper panel shows the variation of the magnetic field component b_x, in (0,y,z)-plane and the figure on the lower panel shows the variation of the same vector in (x,0,z)-plane. The field has been calculated with $r = 1.5mm$, $\lambda = 11.6mm$ and current $I = 300A$. In both plane b_x is perfectly sinusoidal on the z-axis while it is distorted (still periodic) far from the z-axis.

4.3.1.2 Two wire helical coil

Let us consider a helical coil, which is made up of two wires (both having helical geometry and identical axis). To clearly understand, we designate two wires as *wire 1* (follows equations $x = rcos\theta,\ y = rsin\theta,\ z = \lambda\theta/2\pi$) and *wire 2* (follows equations $x = -rcos\theta,\ y = rsin\theta,\ z = \lambda\theta/2\pi$).

In this arrangement and with the positive current in both the wires , the x-component of the magnetic field, B_x becomes sinus on the z-axis both in (x,0,z)-plane and (0,y,z)-plane but far from the z-axis it is not sinus in both these planes. The y-component of the magnetic field, B_y is zero on the coil axis. Far from the coil axis, B_y is zero throughout in the yz-plane while it acquires sinusoidal behavior far from the coil-axis in (x,0,z)-plane. The z-component of the magnetic field B_z in this case, is zero on the coil axis as well as

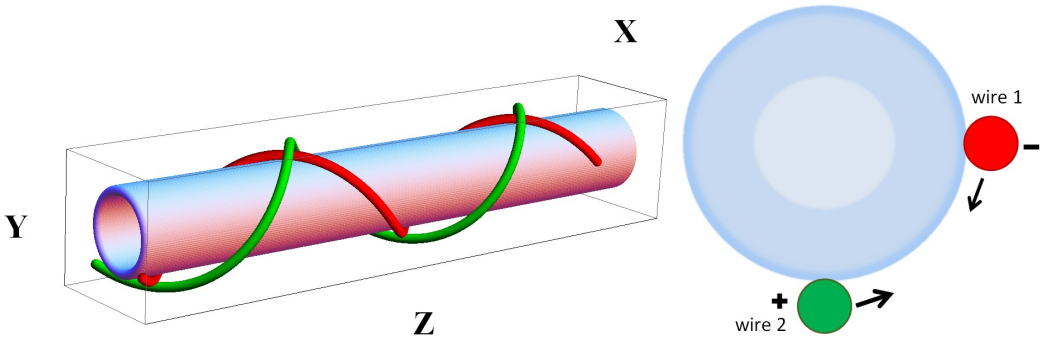

Figure 4.12: The figure on the left shows the three dimensional arrangement of the wires in a helical and the figure on the right shows the front view of the helical coil in two wire geometry. The wires are designated with various colors, signs representing the helicity and the names like, *wire 1, wire 2* which are also followed in table4.1. The arrows in the right figure indicates the rotation of the wire along the positive z-axis.

in the (0,y,z)-plane but it does oscillate (not sinus) far from the coil-axis in the (x,0,z)-plane. The resulted magnetic field strength B is shown in Fig.4.13. In the (x,0,z)-plane B takes a shape which looks like a chain of magnetic wells (we also refer as magnetic hills, sometime) along z while, B in the (0,y,z)-plane is rather distorted which can be minimized with the inclusion of two more wires (helical coil with four wires) and a stronger magnetic field strength can be achieved.

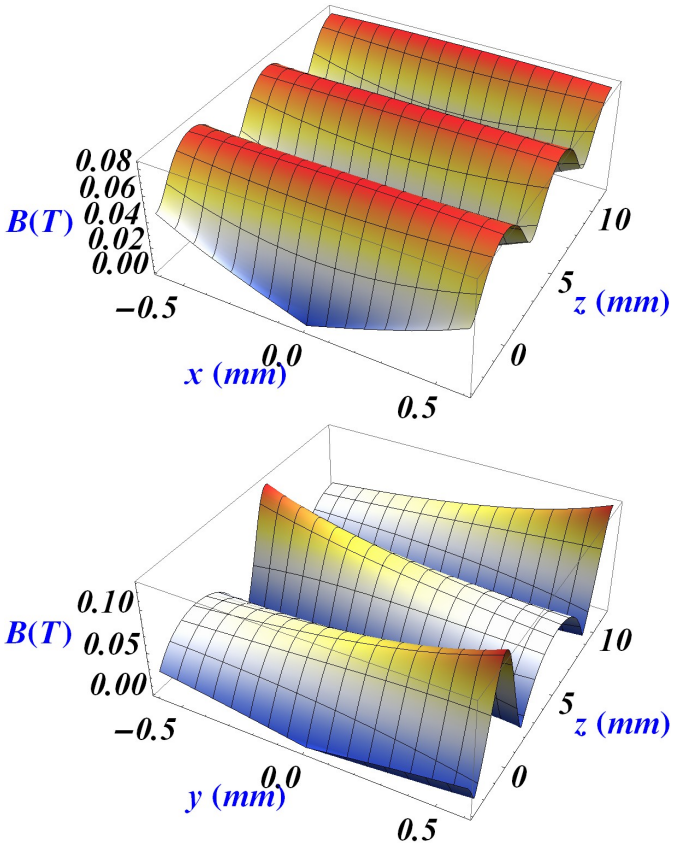

Figure 4.13: The figure on the upper panel shows the variation of the magnetic flux density (B) in the xz-plane containing the coil axis. The field is nicely patterned like a chain of magnetic well along the z-axis. The figure on the lower panel represents the variation of B in yz-plane containing the z-axis which is different from the same in xz-plane. The field has been calculated with $r = 1.5mm$, $\lambda = 11.6mm$ and current $I = 300A$ with the current flowing in the positive direction in both *wire 1* and *wire 2*.

4.3.1.3 Four wire helical coil

Let us introduce two more wires, they are *wire 3* (follows $x = -rcos\theta$, $y = -rsin\theta$, $z = \lambda\theta/2\pi$) and *wire 4* (follows $x = rcos\theta$, $y = -rsin\theta$, $z = \lambda\theta/2\pi$). The details of all four wires with the inter-relations between their generated fields with the positive current flowing through all the wires, are enlisted in Table4.1. For visualization, we introduce the Fig.4.14 showing the 3D-arrangement of the wire forming the helical coil.

The field, generated inside this helical coil (where in all the wires the positive currents are flowing) with this geometry, are much regular. The y-component of the magnetic field B_y is zero both in (x,0,z) and (0,y,z)-planes. The z-component of the magnetic field, B_z is zero in (0,y,z)-plane but it starts oscillating far from the coil-axis in the (x,0,z)-plane (similar to the case of two wire geometry except a difference in amplitude). The major

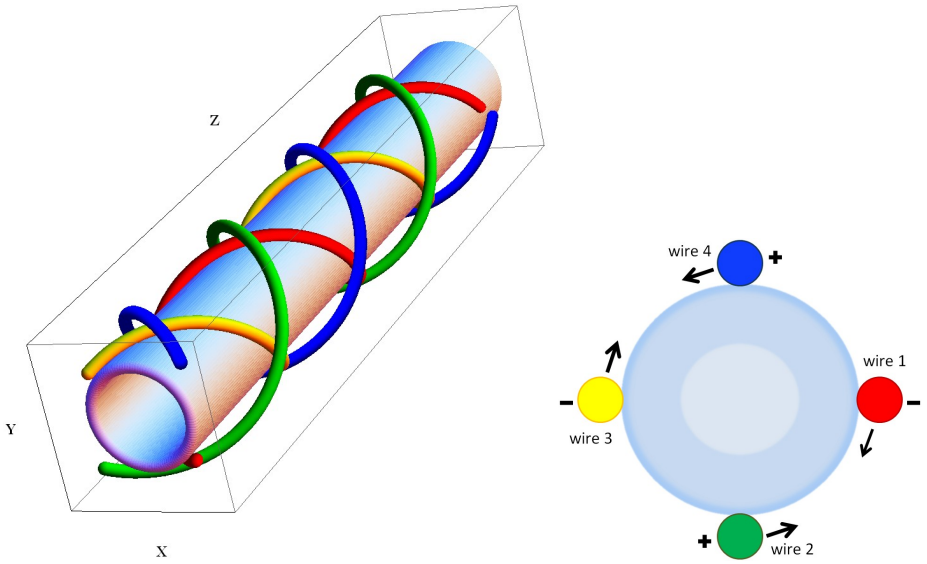

Figure 4.14: The figure on the left shows the three dimensional arrangement of the wires in a helical and the figure on the right shows the front view of the helical coil in four wire geometry. The wires are designated with various colors, signs representing the helicity and the names like, *wire 1, wire 2, wire 3 and wire 4* which are also followed in table4.1.

contribution to the total field comes from the x-component B_x, which much regular than the previous cases. The resulted magnetic flux density is shown in Fig.4.15.

As we already have mentioned, the field strength in both the (x,0,z) and (0,y,z)-plane are nicely patterned in a chain of magnetic hills along the coil axis. The maximum available field strength also increases than that of two wire geometry. One most important feature is that, on the coil axis the only magnetic field component is B_x (which is a sinus) while the others (B_y and B_z) are zero, which is advantageous if one considers to use the magnetic field for deceleration.

By perfectly choosing the positions of the wires and the combinations of the current directions in the wires one ends up with a magnetic field on the coil axis which has only one component along either axis. Once the one dimensional magnetic wave is produced, they can be used for Zeeman deceleration. Especially, there are huge advantages to have a magnetic wave which has only component along the z-axis (the coil axis). This magnetic wave can be used to manipulate the particles motions along the z-axis (deceleration or longitudinal guiding) while an independent inclusion of a transverse field (for example, quadrupole guiding field) can take care of the transverse motions of the particles.

Till now, we have seen how to produce one dimensional static magnetic waves. But, from the experimental point of view, implementation of the helical coils in the form of Zeeman decelerator, are extremely difficult. The reasons behind it are presented in the following. To decelerate considerably or to stop the paramagnetic atoms we need to have

Wire	Parametric Eqn.	Helicity	Field Vectors
wire 1	$x = rcos\theta$ $y = rsin\theta$ $z = \lambda\theta/2\pi$	$-$	$B_{1x}(x,y,z) = +b_x(x,y,z)$ $B_{1y}(x,y,z) = +b_y(x,y,z)$ $B_{1z}(x,y,z) = +b_z(x,y,z)$
wire 2	$x = -rcos\theta$ $y = rsin\theta$ $z = \lambda\theta/2\pi$	$+$	$B_{2x}(x,y,z) = +b_x(-x,y,z)$ $B_{2y}(x,y,z) = -b_y(-x,y,z)$ $B_{2z}(x,y,z) = -b_z(-x,y,z)$
wire 3	$x = -rcos\theta$ $y = -rsin\theta$ $z = \lambda\theta/2\pi$	$-$	$B_{3x}(x,y,z) = -b_x(-x,-y,z)$ $B_{3y}(x,y,z) = -b_y(-x,-y,z)$ $B_{3z}(x,y,z) = +b_z(-x,-y,z)$
wire 4	$x = rcos\theta$ $y = -rsin\theta$ $z = \lambda\theta/2\pi$	$+$	$B_{4x}(x,y,z) = -b_x(x,-y,z)$ $B_{4y}(x,y,z) = +b_y(x,-y,z)$ $B_{4z}(x,y,z) = -b_z(x,-y,z)$

Table 4.1: The details of a helical coil in the four-wire geometry and the dependencies of the magnetic field resulting from each wire (follows the Fig.4.14). The direction of the current flow is considered to be positive in all the wires.

a long decelerator ($\sim 1m$) as the magnetic force exerted on the atoms are very small in general. It requires long helical coil which is very much demanding from driving power as well as power dissipation. Again, we cannot do the fragmentation of the coil along the coil axis. Since, there will always be a gap between the segments because of the wire connections which will inevitably lead to phase mismatch between the magnetic waves from one segment to the other. This limitation will lead to a considerable particle losses for a long decelerator. If we consider not to fragmentize the coil then it will be extremely hard driving current to the coil as it needs a huge power and an efficient heat dissipation. Third, to produce a moderate magnetic field on the coil axis we need to have a very small coil radius. In general the coil is wrapped around a long tube made up of non-magnetic material. As expected, there will be a vacuum problem inside the tube as the tube is not accessible for differential pumping other than its two ends. Fourth, the torsion, produced from all the wires wrapped around the tube, makes it extremely fragile to handle.

To get rid of these above mentioned disadvantages we need to find another way to produce magnetic waves which we are going to discuss in the following Subsection.

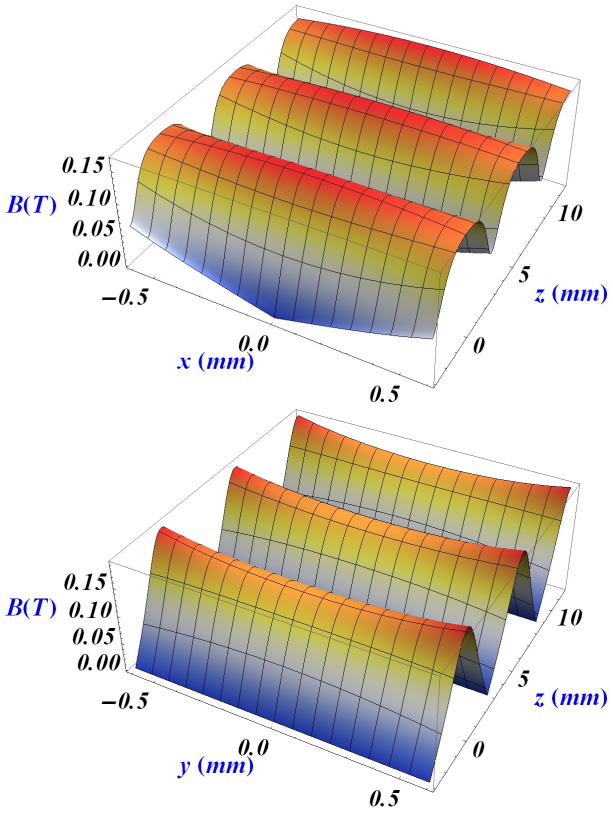

Figure 4.15: The figure on the top panel shows the variation of the magnetic flux density (B) in the xz-plane containing the coil axis. The field is nicely patterned like a chain of magnetic hills along the z-axis. The field increases far from the z-axis in the same plane. The figure on the bottom panel represents the variation of B in yz-plane containing the z-axis also looks like magnetic hills along the z-axis with a little difference as the field does not increases much far from z-axis in the same plane. The field has been calculated with $r = 1.5mm$, $\lambda = 11.6mm$ and current $I = 300A$ with the current flowing in the positive direction in all *wire 1, wire 2, wire 3 and wire 4*.

4.3.2 The Planner Wire-Geometry

On a search for an improved geometry to the helical coil which has all the good properties but easy to implement experimentally, has to have a planner geometry. Here we discuss the coil of that kind. Since our goal is to find a source of magnetic field which can be used for Zeeman deceleration, we are specially interested in an on axis one-dimensional magnetic wave with the magnetic vector along z-axis.

Let us consider, a coil made up of four wires as is depicted in Fig.4.16. These four wires are in two sets with each having two wires. The two wires in each set are wrapped around each other and forms a flat surface. Then, these two sets are placed in (x,r,z) and (x,-r,z)-plane. By introducing a DC current flowing in a particular direction in each wire

(positive or negative depending on whether the current vector has a positive or negative component along z-axis) as shown with arrowheads in Fig.4.16, a periodic magnetic field can be produced along the z-axis which has only z-component (B_z). The direction of the current at a wire-crossing-point (let say, at z=0) is reversed to the next wire-crossing-point (at z=λ/2) moving along z-axis. The resulted on axis B_z takes a shape of static sinus magnetic wave. The field vector, B_z on z-axis is represented by the bold arrows, indicates a periodicity (with λ) with the value depending on the geometry of the coil.

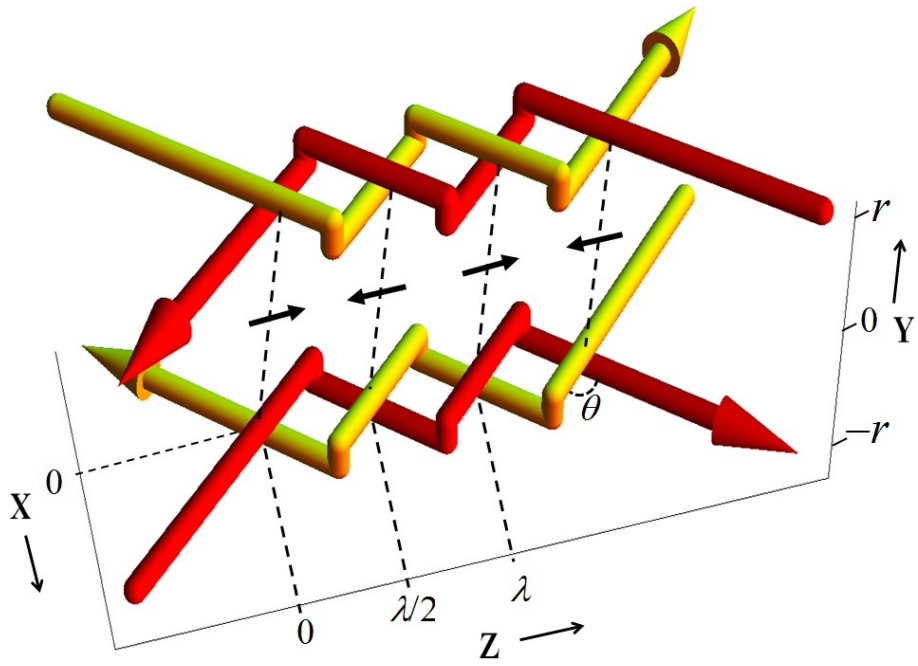

Figure 4.16: The schematic representation of a planner coil which is made out of four wires. Two sets of two wires (red and yellow) are place in the (x,r,z) and (x,-r,z)-plane which are folded around each other as shown in the figure. The arrowheads represent the direction of the flow of the currents in the wires. The z-component of the magnetic field on the z-axis inside the coil is indicated by the bold arrows (in black).

The magnetic fields, calculated using Biot-Savart law are discussed in the following. The calculations are carried out with $r = 1.5mm$, $\lambda = 11.6mm$, $\theta = 35.75°$, the diameter of the wire $d = 0.345mm$ and 300A current in each wire. As one expects from the wire geometry, the z-component of the magnetic field B_z (see Fig.4.17) in (x,0,z)-plane regularly oscillates and in fact, the field amplitude stays nearly constant for a given value of z in the (x,0,z)-plane. In the (0,y,z)-plane, the B_z also oscillates regularly but the field amplitude rises far from z-axis for a given value of z, simply because the field is stronger near to the wires. The maximum amplitude of the x and y-components (B_x and B_y) of the magnetic field is smaller ($\sim$ 20 times for B_x and $\sim$ 5 times for B_y) than B_z (which is $\sim 0.1T$) within a 1.2mm diameter cylindrical volume which is coaxial with the z-axis.

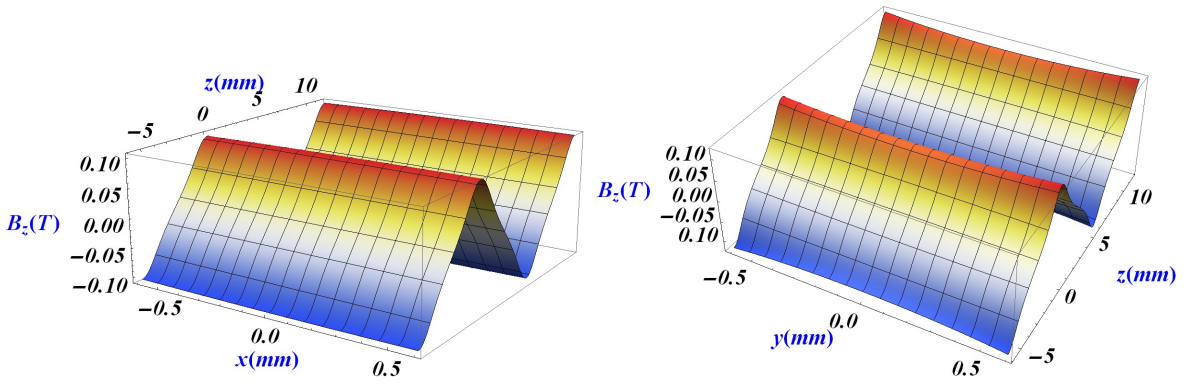

Figure 4.17: The figures represent the variations of the z-component of the magnetic field, B_z in various planes containing the z-axis, calculated using $r = 1.5mm$, $\lambda = 11.6mm$, $\theta = 35.75°$, the diameter of the wire $d = 0.345mm$ and 300A current in the wire following Fig.4.16. The *figure on the left panel* shows the variation of B_z in (x,0,z)-plane. The B_z oscillates along z-axis with the amplitude of $\sim \pm 0.1T$ and it is homogeneous along the x-axis for any given value of z. The *figure on the right panel* represents the variation of B_z in (0,y,z)-plane. It oscillates with the amplitude $\sim \pm 0.1T$ on the z-axis but the amplitude increases slowly far from the z-axis (with a maximum value $\sim \pm 0.12T$).

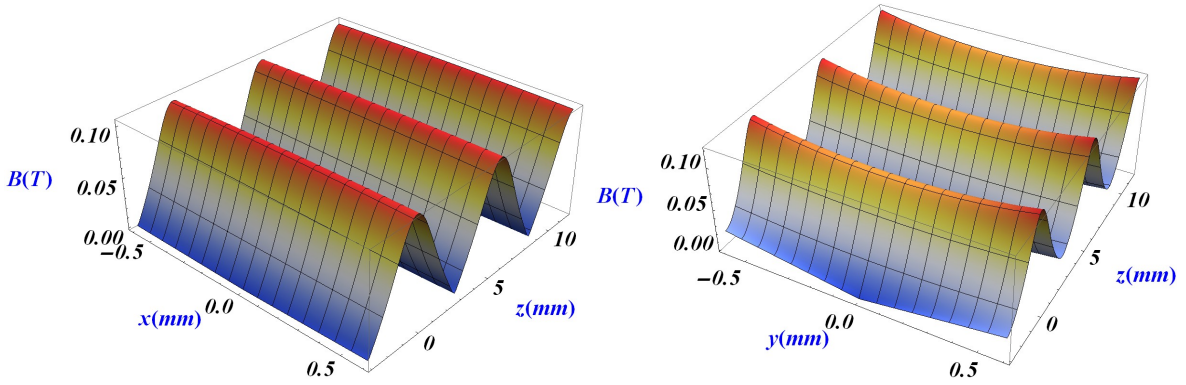

Figure 4.18: The figures represent the variations of the magnetic field strength, B in various planes containing the z-axis, calculated using $r = 1.5mm$, $\lambda = 11.6mm$, $\theta = 35.75°$, the diameter of the wire $d = 0.345mm$ and 300A current in the wire as shown in Fig.4.16. The *figure on the left panel* shows the variation of B in (x,0,z)-plane. The B_z oscillates along z-axis with the amplitude of $\sim \pm 0.1T$ and it is nearly homogeneous along the x-axis for any given value of z. The *figure on the right panel* represents the variation of B in (0,y,z)-plane. It oscillates with the amplitude $\sim \pm 0.1T$ on the z-axis but the amplitude increases slowly far from the z-axis (with a maximum value $\sim \pm 0.12T$).

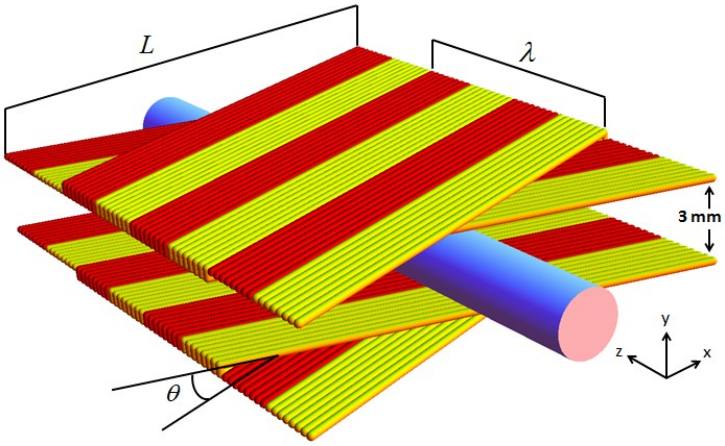

Figure 4.19: The schematic representation of the planner-coil with eight wire geometry encapsulating a glass tube of 3mm outer-diameter, is used to produce on-axis one-dimensional (z) magnetic wave. If the red-set of wires is considered to produce a sine-wave then yellow-set produces cosine-wave. The wave length (λ) is determined by the diameter of the wire (d) and the angle θ.

The B_y acquires zero value throughout the (x,0,z)-plane due to the complete cancellation of the y-component while it oscillates (with maximum amplitude $\sim 0.022T$ at the edge of the cylinder which is $0.6mm$ far from the coil-axis) in (0,y,z)-plane. The B_x component has a smaller value ($\sim 0.005T$) and oscillates both in (x,0,z) and (0,y,z)-plane. The resulting magnetic field strength (B) with its variation in both (x,0,z) and (0,y,z)-plane is shown in Fig.4.18.

4.3.3 The Decelerator

By using more wires instead of one, we can increase the field strength inside the coil. For example, use of eight wires (in the same plane which finally looks like a wire-strap) in place of one-wire as we mentioned in the previous subsection, we can increase the field strength (~ 8 times), which can be used for the deceleration.

Once the chain of magnetic hills, which can be considered as it has been resulted from the sinus magnetic wave, is in hand, it is easy to produce another field (also a chain of magnetic hills which can be considered as it from cosine-magnetic wave) just by adding a similar coil with the same geometry but shifted by $\lambda/4$ along the z-axis. A schematic representation of this coil is shown in Fig.4.19. If the red wires are denoted to generate a sin-wave then, the yellow set of wires generates a cosine-wave of magnetic field.

The decelerator used in the experiment, consists of two different magnetic coils (see Fig.4.34, for details). One is dedicated to manipulate the transverse motion of the atoms

(to focus and guide in transverse directions) while, the other one is dedicated to manipulate the longitudinal motion (like, longitudinally guiding and deceleration of the atoms). The transverse confinement and the guiding is carried out with the quadrupole guide, we have discussed in the previous chapter. The longitudinal guiding and the deceleration are performed with the planner-coil. To quantify the field geometry we have calculated the field in the eight wire geometry with the parameters $\lambda = 11.6mm$, $\theta = 35.75°$, $I = 300A$ (with the current directions such that it produces a magnetic wave on the axis which has only z-component) and with the diameter of the wire $d = 0.345mm$. The variation of the on axis magnetic field vectors (B_x, B_y and B_z) along z are shown in Fig.4.20.

The field geometries produced only from the planner coil for the cosine-field, are presented in the Fig.4.21. Similarly as we already have noticed in the previous subsection, the field strength B in (x,0,z)-plane forms a chain of magnetic hills along the z-axis. The field strength B varies from 0T to 0.695T on the z-axis and stays nearly constant for a given value of z along x-axis at the top of the magnetic hill in the (x,0,z)-plane while the field increases to $\sim 0.02T$ at the position 0.6mm far from z-axis at the bottom of the hill. The B in the (0,y,z)-plane also increases as one goes along y-axis and reaches 0.75T from 0.69T at the top of the magnetic hill while reaches 0.2T from 0T at the bottom of the magnetic hill.

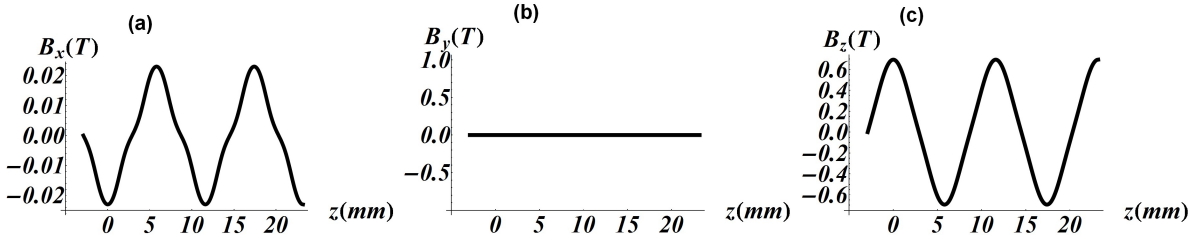

Figure 4.20: The variations of the field vectors (a) B_x, (b) B_y and (c) B_z along the coil axis, z.

The addition of a quadrupole guiding coil introduces an independent radial magnetic field. The field has been calculated with the previous parameters for the planner coil along with 100A current in the quadrupole guide and presented in the Fig.4.22. The dimensions and other parameters associated with the quadrupole magnetic guide are same as described in the previous chapter. On the z-axis the field remains the same as of the previous case but the field far from the z-axis becomes modified. When DC current in the planner coil, the field vectors change their sign in each $\lambda/2$ distance. With DC current flowing both in the planner coil and the quadrupole guide coil, a field oscillation with a periodicity of λ is expected. Because, at a position the field vectors (from the quadrupole guide and the field from the planner-coil) add up constructively while they add up destructively at other positions located $\lambda/2$ far along the z-axis. The field oscillation

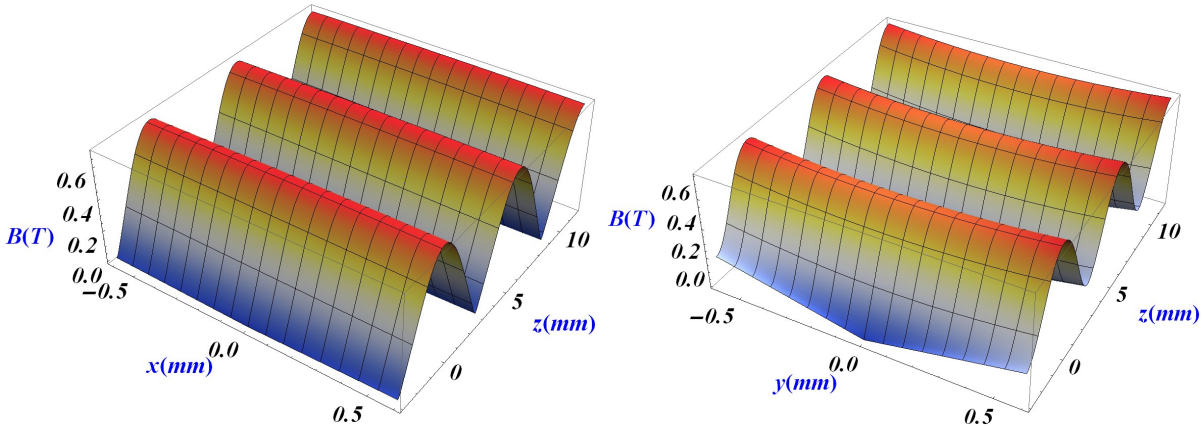

Figure 4.21: The variation of the magnetic field strength, B generated from a planner-coil with eight wire geometry. The field has been calculated with the parameters $\lambda = 11.6mm$, $\theta = 35.75°$, $I = 300A$ (with the current directions such that it produces a magnetic wave on the axis which has only z-component) and with the diameter of the wire $d = 0.345mm$. The *figure on the left panel* represents the variation of B in (x,0,z)-plane. On the z-axis, the B varies from 0T to 0.695T. At the bottom of the magnetic hill, B (from x=0 to x=0.6mm) increases to 0.02T from 0T while at the top of the magnetic hill, B slowly decreases to 0.69T from 0.695T. The *figure on the right panel* shows the variation of B in (0,y,z)-plane. At the bottom of the magnetic hill, B (from y=0 to y=0.6mm) increases to 0.2T from 0T while at the top of the magnetic hill, B increases to 0.75T from 0.695T.

far from the z-axis due to the presence of the quadrupole guide is shown in Fig.4.23. At x=0.6mm in the (x,0,z)-plane, the B oscillates between 0.03T to 0.07T at the bottom of the magnetic hill and 0.690T to 0.693T at the top of the magnetic hill. Similarly, at y=0.6mm in the (0,y,z)-plane, B oscillates from 0.14T to 0.26T at the bottom of the magnetic hill while it stays nearly constant with 0.75T at the top of the magnetic hill.

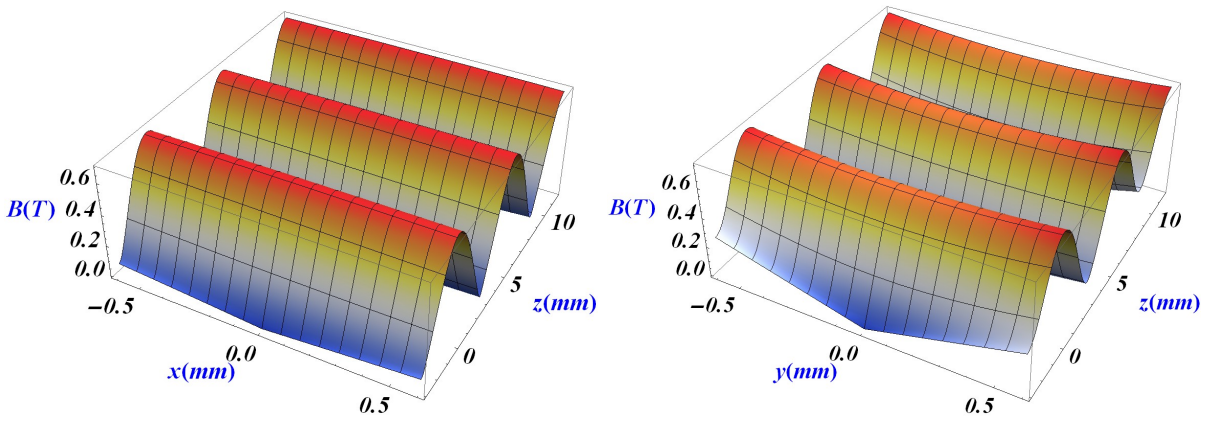

Figure 4.22: The variation of the magnetic field strength, B generated from a planner-coil with eight wire geometry and additional quadrupole guide. The field has been calculated with the parameters $\lambda = 11.6mm$, $\theta = 35.75°$, $I = 300A$ (with the current directions in the planner-coil such that it produces a magnetic wave on the axis which has only z-component), the diameter of the wire $d = 0.345mm$ and $100A$ in the quadrupole guide. The *figure on the left panel* represents the variation of B in (x,0,z)-plane. The *figure on the right panel* shows the variation of B in (0,y,z)-plane. On the z-axis, the B varies from 0T to 0.695T but far from z-axis the B oscillates differently (see Fig.4.23).

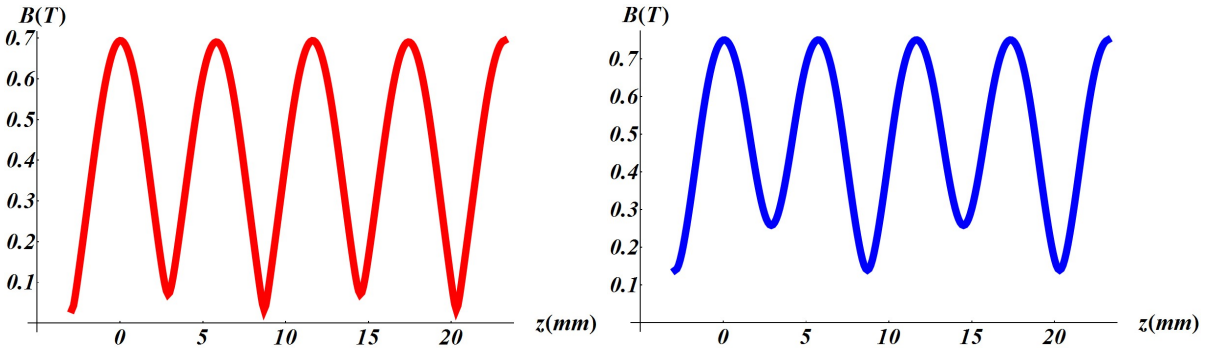

Figure 4.23: The variation of the off-axis magnetic field strength B along z, generated from a planner-coil with eight wire geometry and additional quadrupole guide. The field has been calculated with the parameters $\lambda = 11.6mm$, $\theta = 35.75°$, $I = 300A$ (with the current directions in the planner-coil such that it produces a magnetic wave on the axis which has only z-component), the diameter of the wire $d = 0.345mm$ and $100A$ in the quadrupole guide. The *figure on the left panel* shows the oscillations of B at (x=0.6mm, y=0mm) along z. The top and bottom of the magnetic hill varies from 0.690T to 0.693T and 0.03T to 0.07T, respectively. The *figure on the right panel* shows the oscillations of B at (x=0mm, y=0.6mm) along z. The top of the magnetic hill stays constant with 0.75T while the bottom of the magnetic hill varies from 0.14T to 0.26T.

4.3.4 Deceleration using Traveling Magnetic Waves: The Principle and the Motions in the Decelerator

The principle of the operation is better understood by picturing the static magnetic potential to be sinus on the coil axis (z) which is produced by the red and yellow set of wires (see Fig.4.19), connected to the DC current. On the coil axis, the longitudinal field is zero at the nodes while has the maximum value at the saddle points of the sine wave as,

$$B(z) = B_0\ cos(kz) + B_0\ sin(kz) = \sqrt{2}B_0\ sin(kz + \pi/4) \tag{4.9}$$

where $k = 2\pi/\lambda$ and λ is the wavelength of the wave, is determined by the geometry of the coil. The potential energy varies as a paramagnetic atom (in LFS states) moves along the z-axis as,

$$E(z) = -\mu_{eff}.|B(z)| = E_0\ \sqrt{sin^2(kz + \pi/4)} \tag{4.10}$$

where $E_0 = -\mu_{eff}.\sqrt{2}B_0$. So, if we let an atom pass through the static potential it will change its velocity but the overall change in velocity will be zero since the gain and loss in velocity will exactly be same.

The situation will be different once we introduce a time dependence in the sinus magnetic field (also the potential) by driving the red and yellow set of wires with AC currents (with a particular phase difference). In fact by independently driving both the set of wires with an alternative current (AC) of angular velocity ω and a phase difference of $\pi/2$, we introduce a time dependence resulting in a traveling-magnetic-wave which can be expressed as,

$$B(z,t) = B_0\ sin(kz)cos(\omega t) - B_0\ cos(kz)sin(\omega t) = B_0\ sin(kz - \omega t) \tag{4.11}$$

The direction of propagation of the magnetic wave depends on the relative phase of the AC current, we choose. The velocity of the wave directly dependent on the driven frequency of the AC current since, the wavelength (λ) of the wave is fixed by the geometric constraint of the magnetic-coil. The velocity of the wave with a frequency $\nu = \omega/2\pi$, is $v = \omega/k = \lambda{\cdot}\nu$.

4.3.5 Longitudinal Guiding

In the case of a constant driving frequency, the velocity of the magnetic-wave stays constant. The resulting Zeeman potential is written as,

$$E(z,t) = E_{max}\ \sqrt{sin^2(kz - \omega t)} \tag{4.12}$$

where $E_{max} = -\mu_{eff} \cdot B_0$. It may be considered as the chain of potential wells moving along the longitudinal axis with the constant velocity $v = \omega/k = \lambda{\cdot}\nu$. For an atom in LFS

state, the potential forms a chain of moving traps where the center of the trap coincides with the bottom of the potential well and a trap depth E_{max}, as shown in Fig.4.24. In a beam of atoms, there present both the velocity and the position spreads. The motions of the atoms during the longitudinal guiding are considered in the following.

4.3.5.1 Longitudinal Motion inside the Trap

Let us consider only the longitudinal motion (1D). A synchronous atom can be defined to have exactly the same velocity and the position which exactly coincides with the bottom of the trap (see Fig.4.24) and always stays in the same position in a potential-well. In a frame moving with the velocity of the magnetic wave the synchronous atom does not feel the presence of the potential while a non-synchronous atom sees the potential. In the moving frame the potential becomes static and can be written as,

$$E(z) = E_{max}\ \sqrt{sin^2 kz} \tag{4.13}$$

To understand the motions of the non-synchronous atoms in the frame moving with the trap, let us consider an atom starts its flight from an initial position which coincides with the position of the potential minimum (we refer it as the *center of the trap*) in the moving-frame and has a positive initial relative velocity.

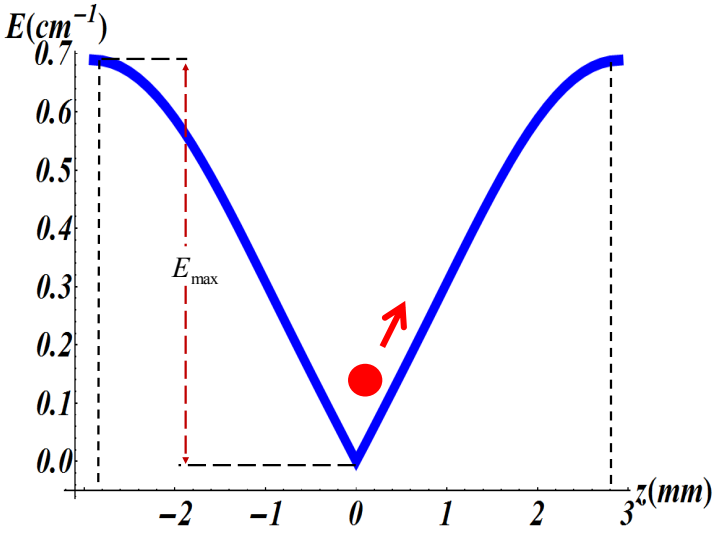

Figure 4.24: The potential well (trap) seen by a co-moving argon atom in $^3P_2$, $m_J = 2$ quantum state with $300A$ AC current in the decelerator. Here the center of the trap is chosen to be at z=0.

So, the atom will start climbing up the potential hill with time. It will acquire more and more potential energy and consequently, reduce its velocity corresponding to the

decrease in kinetic energy. The atom with more velocity will lose its kinetic energy more as it moves higher in the potential well than the atoms with lower velocities. If the total energy (corresponds to the kinetic energy due to the relative velocity and the potential energy due to its position in the potential well) of the atom, in the moving frame, is less than the trap depth E_{max} (see Fig.4.24), it will change its direction and travels down the potential hill. It will acquire exactly the same but negative initial relative velocity when it will arrive at the position of the synchronous atom and the reverse process will take place. So, the atom will oscillate around the synchronous atom. Similarly, the atom with same initial velocity but different initial position also will oscillate around the synchronous atom. The atom will stay inside the potential well if the total energy of the atom in the moving frame is less than or just equal to the maximum possible change in potential energy (which is the trap depth, E_{max}) inside the trap, as it moves. So, the atom will be *confined* inside the potential well. On the other hand if the total energy is more than the trap depth E_{max}, it will be lost from the trap.

It is noted that a maximum change in potential energy (as well as kinetic energy) is possible if and only if the atom starts its flight from the center of the trap for a particular velocity in the moving frame. For the trap, that determines highest limit in the velocity of a particle can be captured in the potential well (the *velocity acceptance* of the trap). For an atom inside the potential well, the maximum change in potential energy is

$$\Delta E_{max} = \left[E_{max}\ \sqrt{sin^2(kz)}\right]_{z=0}^{z=\lambda/4} = E_{max} = \frac{1}{2} m_p v_{trap}^2 \tag{4.14}$$

where the m_p is the mass of the atom (or molecule) and the v_{trap} is the maximum velocity of an atom in the moving frame which can be trapped inside the potential well. To look into the evolution in velocity and position with time we need to see the phase-space diagram. Here we consider the 1D motion (longitudinal) of the atoms in the reference frame moving with the velocity of the traveling well (which is also the velocity of the synchronous atom), with the equation of motion:

$$m\frac{d^2z}{dt^2} = -\nabla_z E(z) = -\frac{2\pi E_{max}}{\lambda}\ Sign\left[sin\left(kz\right)\right]\ cos\left(kz\right) \tag{4.15}$$

This equation the gives the motion of the non-synchronous atoms with respect to the synchronous ones in the laboratory frame. The corresponding phase-space diagram due to above equation of motion, is presented in Fig.4.25. The red highlighted trajectory in the figure is the separatrix, indicates that any phase-space point in the area enclosed by the separatrix will follow a closed trajectory.

The separatrix determines the upper bounds of velocity and position of the trapped particles. The phase-space diagram has been calculated with the 300A of AC current driven in the planner coil and the 100A of DC current driven in the quadrupole guiding

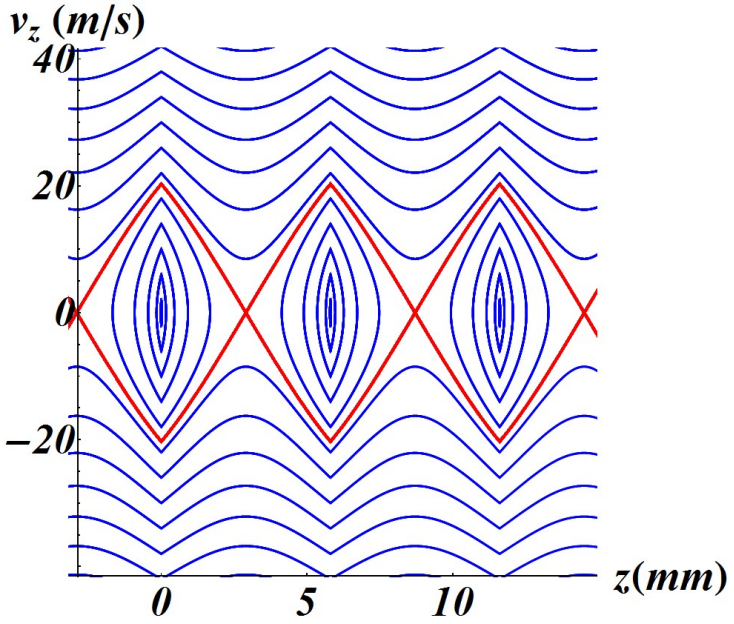

Figure 4.25: The isoenergic trajectories in phase-space for argon atoms in $^3P_2,\ m_J = 2$ quantum state with $300A$ AC current in the decelerator. The center of the trap is chosen to be at $z = n\lambda/2$ with n=0,1,2 etc. In this case the velocity of the magnetic-wave is considered to be constant. The highlighted red-line shows the separatrix. The trajectories are closed only in the inner region of the separatrix.

coil. The resulting trap has a size of $\lambda/2 = 5.8mm$ along the longitudinal direction and the longitudinal velocity acceptance of 20m/s for the argon atoms in $^3P_2,\ m_J = 2$ state.

In the Fig.4.26 the trajectories during the course of longitudinal guiding with $464m/s$ for the argon atoms in $^3P_2,\ m_J = 2$ state are presented. The figure on the upper panel (a) of Fig.4.26, represents trajectories for a bunch of argon atoms with the same velocity but has a longitudinal position distribution. The calculation has been done with the considerations that the magnetic potential starts at 5cm and ends at 33cm. As the atoms enter, the potential region and the magnetic field is switched-on, experience the trapping force and that introduces a velocity spread which is distributed in the atoms. Since the initial velocity of the atoms are equal to the velocity of the potential well, the atoms with this velocity spread (due to the potential only) are still trapped throughout the process. The figure on the lower panel (b) of Fig.4.26, illustrates the trajectories during the course of longitudinal guiding at $464m/s$ for the argon atoms in a beam with the spreads both in longitudinal position and velocity. The trajectories of the guided atoms are the ones with the initial velocities from 444m/s to 484m/s (accepted velocity).

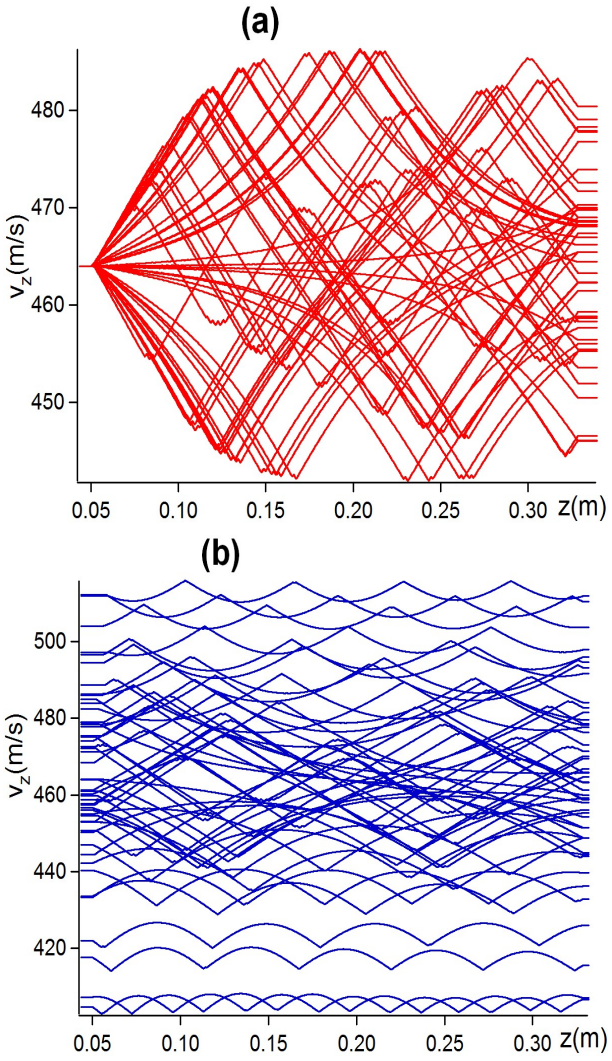

Figure 4.26: The figures represents the simulated trajectories of the particles moving through the decelerator during longitudinal guiding considering only the position and velocity spreads along longitudinal direction. The simulations have been performed for argon atoms in $^3P_2$, $m_J = 2$ state and 300A AC current in the decelerator. The decelerator starts at 5cm and ends at 35cm along z. The figure (a) shows the trajectories corresponding to the particles with position spread but do not have a longitudinal velocity spread. The figure (b) shows the trajectories for atoms with a spread in both position and velocity, respectively.

4.3.6 Deceleration

As the magnetic wave's velocity depends on the instantaneous driving frequency of AC current, we can modulate the velocity as is required. The velocity of the magnetic-wave at an instant t is,

$$v(t) = \lambda \left(\nu(t) + \frac{d\nu(t)}{dt} t \right) \tag{4.16}$$

The $\nu(t)$ is the instantaneous frequency of the AC current, determined by the electronics which is driving the current and can be increased or decreased continuously. $d\nu/dt$ is the rate frequency sweep. So, we can gradually change the velocity of the magnetic-wave by sweeping the driving frequency. In the case of deceleration where the driving frequency decreases with a constant rate $-\frac{d\nu(t)}{dt} = -a$, the rate of change in velocity (in the laboratory frame) of the traveling wave becomes,

$$-\frac{dv}{dt} = -2\lambda a \tag{4.17}$$

4.3.6.1 Longitudinal Motion inside the Trap

To see the motions of the atoms inside the potential well, we need to choose a decelerated frame that is moving with the instantaneous velocity of the magnetic wave. A constant rate of change in driving frequency (the sweeping rate a) of the magnetic wave corresponds to a uniform drift in velocity of the wave. That is linear in time and the magnetic wave is stationary in the decelerated frame. Due to the deceleration of the periodic potential, the atoms thus experience a constant inertial force in addition to the force from the periodic potential in the decelerated frame as,

$$F = 2m_p \lambda a \tag{4.18}$$

Due to that, in the decelerated frame the potential will be deformed from the non-decelerated one (in case of deceleration) and seen by the atoms as,

$$E(z) = E_{max} \sqrt{sin^2(kz)} - 2m_p \lambda a z \tag{4.19}$$

The force applied to the system depends on the rate of frequency sweeping. Similarly, the deformation of the potential depends on the it. In particular to see the deformation and the deceleration ability, let us consider the applied deceleration force F in terms of the E_{max} as,

$$F = 2m_p \lambda a = \epsilon \cdot \frac{2\pi}{\lambda} E_{max} \tag{4.20}$$

The E_{max} is constant for an AC current with a fixed amplitude and ϵ, a parameter varies from 0 to 1, is to define the strength of the deceleration force. As we have mentioned

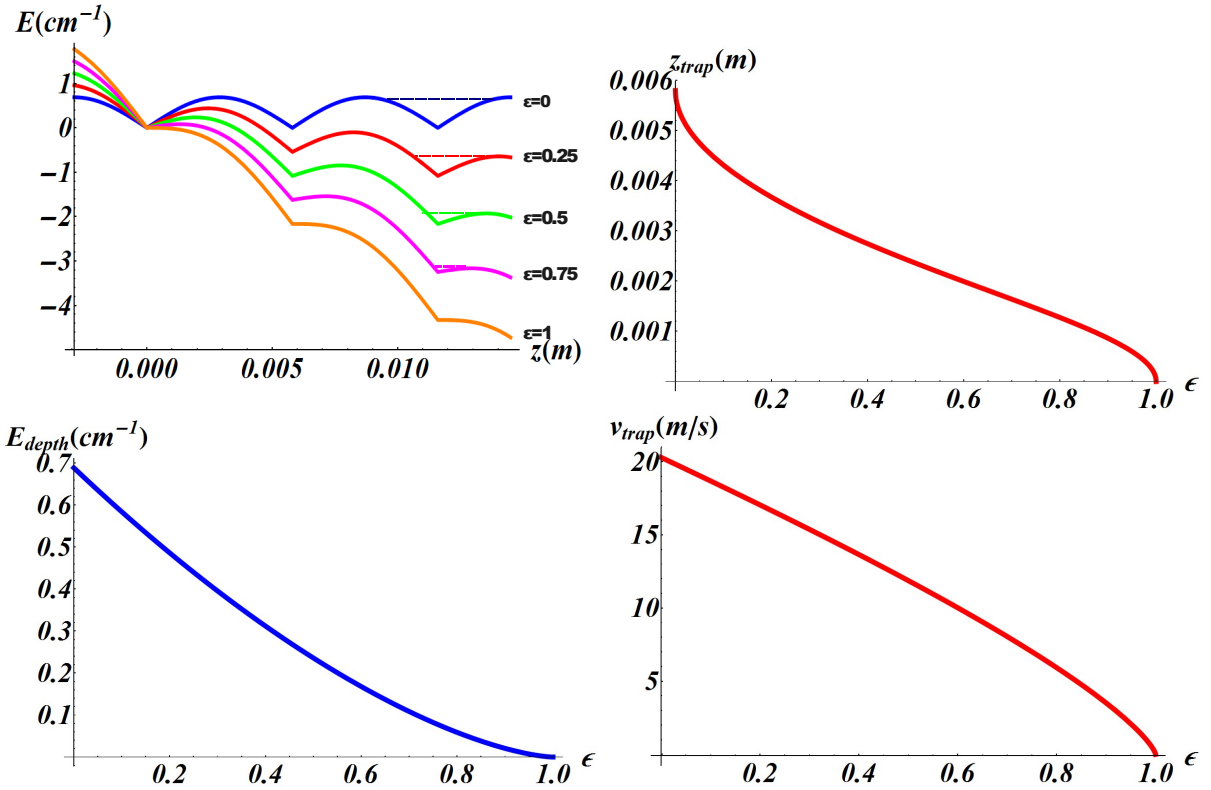

Figure 4.27: The *left figure on the top panel* shows the deformation of the Zeeman potential (E) with various strength of deceleration parameterized by ϵ. The first trap center is chosen to be at $\lambda/4$ from the origin along z. The *right figure on the top panel* indicates the change in trap size, z_{trap} (along longitudinal direction) with ϵ. The *left figure on the bottom panel* represents the variation of the trap depth (E_{depth}) with ϵ and the *right figure on the bottom panel* shows the variation of the velocity acceptance (v_{trap}) of the trap with ϵ. The calculations are carried out for argon atoms in $^3P_2$, $m_J = 2$ quantum state and 300A AC current in the decelerator.

before, the atoms are longitudinally confined during the process and this confinement depends on the trap depth. During the longitudinal guiding (which is for ϵ) the trap depth, $E_{depth} = E_{max}$. But, that will not be the case when $\epsilon > 0$. The depth of the magnetic potential is reduced with the application of the deceleration force and higher the deceleration force lower is the potential depth (E_{depth}), can be written as,

$$E_{depth} = E_{max}\left[\left(\sqrt{sin^2\left[cos^{-1}(\epsilon)\right]} - \epsilon cos^{-1}(\epsilon)\right)\right] \tag{4.21}$$

It determines the velocity acceptance, v_{trap} (as we did for longitudinal guiding, Eqn.4.14).

Again, the trap size (length along the longitudinal direction) changes with the ϵ. When $\epsilon = 0$ (for longitudinal guiding), the trap size is $\lambda/2$. But, it is reduced in the

presence of deceleration force ($\epsilon > 0$) and reduces to zero with $\epsilon = 1$. More is the rate of deceleration smaller is the size of the trap.

The deformed potential has been calculated for argon atom in $^3P_2,\ m_J = 2$ quantum state with the driving current of 300A in the decelerator, is shown in the Fig.4.27. This also illustrates the variation of the trap depth (E_{depth}), the velocity acceptance (v_{trap}) and the trap size (z_{trap}) with ϵ which defines the strength of the deceleration force F.

A synchronous atom always stay at the position of the center of the potential well (at the potential minimum) in the accelerated frame and experiences a constant force (following Eqn.4.20) during the deceleration. For the atoms having slightly different position and velocity in the potential well than the synchronous atoms oscillate around the synchronous atoms. The dynamics of the atom inside the trap during deceleration is expressed by the equation:

$$m\frac{d^2z}{dt^2} = -\frac{2\pi E_{max}}{\lambda}\ Sign\left[sin\left(kz\right)\right]\ cos\left(kz\right) + \epsilon \cdot \frac{2\pi E_{max}}{\lambda} \tag{4.22}$$

The isoenergic trajectories in phase space are presented in Fig.4.28, are calculated for the argon atoms in $^3P_2,\ m_J = 2$ quantum state and with 300A AC current in the decelerator. In comparison to the case for longitudinal guiding where the atoms longitudinally oscillate symmetrically (with respect to the center of the potential well) inside the trap. In the case of deceleration, this symmetry will break as a biased potential is present due to the additional deceleration force. The resulted separatrix with various strength of decelerations are shown in Fig. 4.29.

In the Fig.4.30 the trajectories during the course of deceleration from 400m/s to 370m/s for the argon atoms in $^3P_2,\ m_J = 2$ state are shown. The figure (a) represents the trajectories for a bunch of metastable argon atoms with the same velocity but with a longitudinal position distribution. The calculation has been done with the considerations that the magnetic potential starts at 5cm and ends at 33cm along z. The atoms, as the magnetic field is switched-on, experience the trapping force which introduce a velocity spread in the atoms. The atoms which are initially behind the position of the center of the trap get an acceleration and increase their velocity in the forward direction. As the velocity of the magnetic potential decreases with time, some of these atoms with enough kinetic energy (in the decelerated frame) leave the potential well. While, the atoms which are initially in front of the position of the center of the potential well are trapped throughout the process. The figure (b) illustrates the trajectories during the course of deceleration from 400m/s to 370m/s for the argon atoms in a beam having spread both in the longitudinal position and the velocity. The atoms with the position and velocity laying inside the range of the phase space accepted area, are longitudinally focused and stay together during the course of deceleration as shown in Fig.4.31.

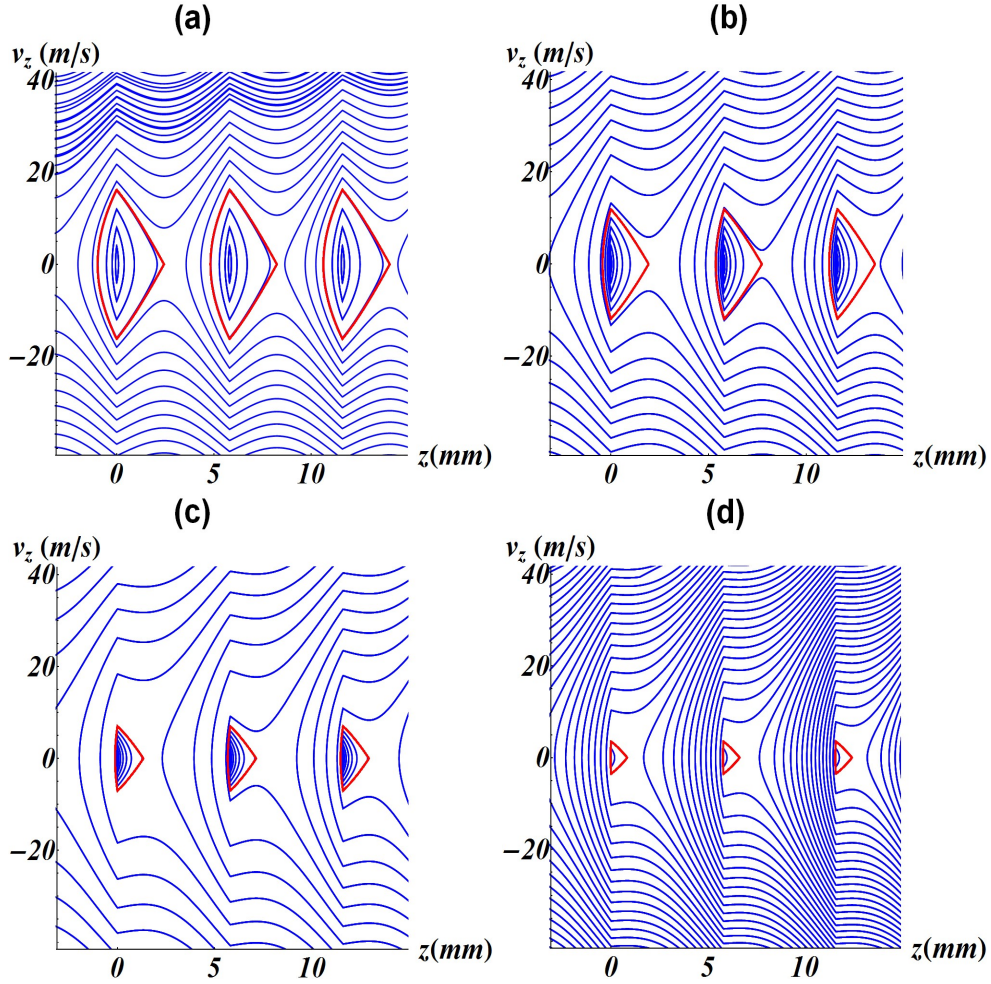

Figure 4.28: The 1D phase stability diagram for various rate of deceleration. The calculation is carried out using the Eqn.4.22 for argon atom in $^3P_2$, $m_J = 2$ quantum state and $300A$ AC current in the decelerator. The inside space of the highlighted red-line show the phase stable region during the course of deceleration. The velocity acceptance (v_{trap}) inside the trap changes with the rate of deceleration. Diagram (a) corresponds to $\epsilon = 0.25$ (with $v_{trap} = 16.2m/s$), (b) corresponds to $\epsilon = 0.5$ (with $v_{trap} = 12m/s$), (c) corresponds to $\epsilon = 0.75$ (with $v_{trap} = 7m/s$) and (d) corresponds to $\epsilon = 0.9$ (with $v_{trap} = 3m/s$).

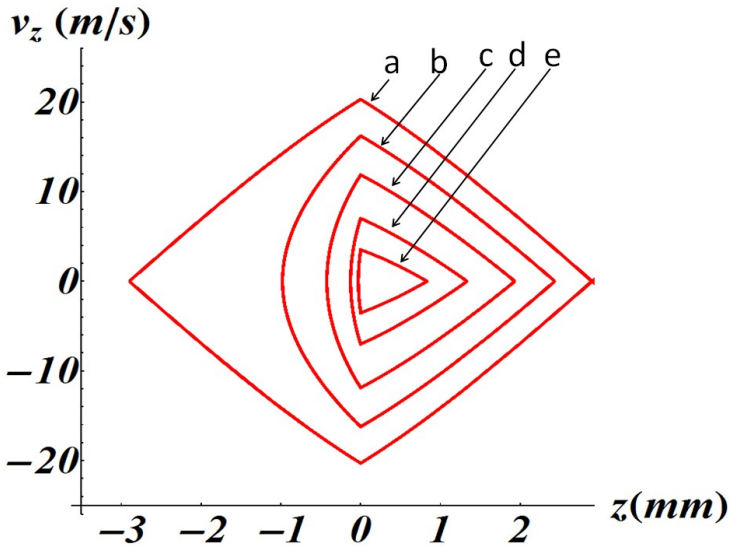

Figure 4.29: The calculated acceptable areas (defined by the enclosed area of the separatrix) in phase space with various strength of deceleration forces for the argon atoms in $^3P_2$, $m_J = 2$ quantum state and with 300A AC current in the decelerator. The separatrix (a), (b), (c), (d), (e) and (f) are correspond to the deceleration forces with $\epsilon = 0$, $\epsilon = 0.25$, $\epsilon = 0.5$, $\epsilon = 0.75$ and $\epsilon = 0.9$, respectively.

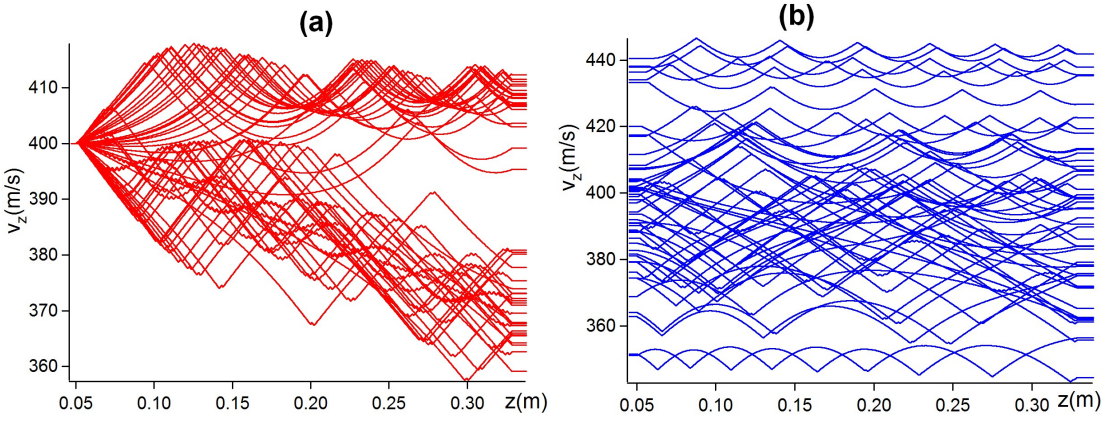

Figure 4.30: The figures represents the trajectories from 3D-trajectory simulations of the atoms moving through the decelerator during deceleration (from $400m/s$ to $370m/s$) considering only the position and velocity spreads along longitudinal direction. The simulations have been carried out for argon atoms in $^3P_2$, $m_J = 2$ quantum state with 300A AC current in the decelerator. The figure (a) shows the trajectories corresponding to the particles with position spread but no longitudinal velocity spread. The figure (b) shows the trajectories for particles with a spread in both position and velocity.

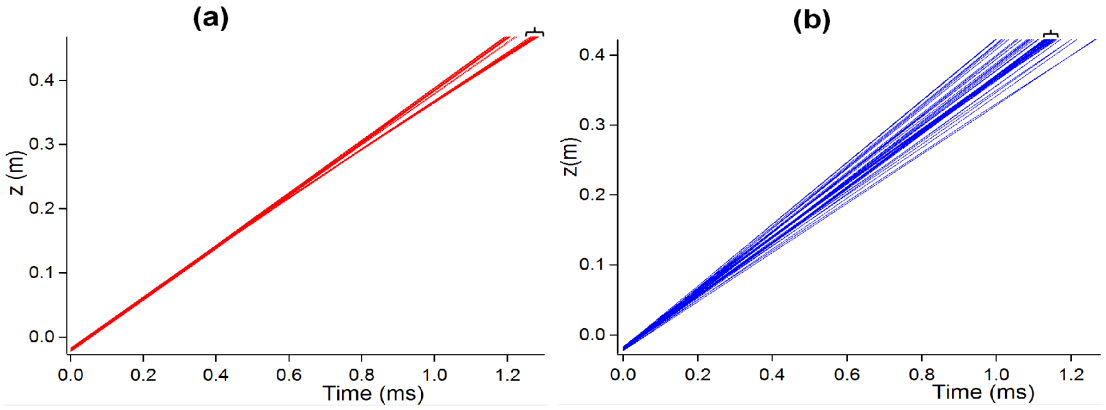

Figure 4.31: The evolution of the argons atoms in time during the course of deceleration from 400m/s to 370m/s. The calculations are done with argon atoms in $^3P_2$, $m_J = 2$ quantum state with 300A AC current in the decelerator. The figure (a) corresponds to the argon beam only having the longitudinal position distribution while figure (b) corresponds to the argon beam having both the position and velocity spreads. The atoms which are trapped and decelerated, are indicated with the solid brackets (in black).

4.4 Experimental Set-Up

To make the first demonstration of the deceleration, the experiments have been carried out with metastable argon atoms in a supersonic beam. The experimental set-up can be divided into two parts as follows. First, the production and the detection of the supersonic beam of metastable argon atoms. Second, the decelerator coil and the electronics to drive it. The experimental set-up is schematically depicted in Fig.4.32

The experimental section dedicated to the supersonic beam involves three major sections as we have described in the previous chapters. The first section consists of supersonic beam machine with the *valve* for supersonic expansion placed inside the vacuum chamber (with an inside pressure $\sim 10^{-6} mbar$), pumped by a turbo-molecular pump. The supersonic expansion is carried out by letting the gas expand from a high pressured ($\sim 2bar - 4bar$) gas container to the vacuum through the valve. The typical duration of the valve pulse is $\sim 180\mu s$. At the exit of the valve there are two electrodes which are installed to discharge (by electric-glow-discharge) the expanding argon gas to achieve a metastable ($^3P_2$) quantum state. For the argon beam, the voltage difference between the electrodes is $\sim 800V$ with a discharge pulse length of $\sim 15\mu s$. The supersonic expansion is occurred right after the electrodes. For a supersonically expanded beam, the translational temperatures and velocities are determined by the temperature of gas container from which it has expanded (in our case it is the valve). By pre-cooling the valve itself, we can achieve a colder supersonic beam with lower mean velocity which is the case for

our experiment. The valve is encapped with a small *Liq.* N_2 chamber. To modulate the temperature of the valve we control the flow of *Liq.* N_2 inside the *Liq.* N_2 chamber by using feed-back loop (see previous chapters). By this way a valve temperature of 158K is achieved in the experiment. Once the cold beam of metastable argon gas is produced, they are passed through a 2mm diameter skimmer installed $2cm$ downstream from the exit of the valve, to collimate and filter out the most intense, central part of the beam. Also, the beam direction is defined by the skimmer. After the skimmer, a long and narrow glass-tube (43cm long and with 1.2mm and 3mm inner and outer diameter, respectively) is introduced. The glass tube ends at the experimental chamber where the MCP (Micro-Channel-Plate) detector is mounted. The two-stage MCP (*HAMAMATSU, F1552-07*4 with $0.3mm$ thickness and $7.5\mu m$ channel diameter) set-up and its working principles are the same as we mentioned in the second chapter. The voltage difference is applied between the MCP plates is $2kV$. The produced electrons, as the excited atoms impinge on the surface of the MCP, are collected to an anode which is again connected to the Oscilloscope to record the Time-Of-Flight (TOF) distribution of the atoms in the beam.

The glass-tube section is the heart of our experiment and dedicated to all the magnetic coils for the transverse guiding, longitudinal guiding and deceleration. There are two independent coils for two different purpose. For clarity, a schematic representation of the magnetic coils are presented in Fig.4.34. One is dedicated to the quadrupole transverse guiding, consists of four sets of wires while each set is made up of five copper wires with a radius 0.345mm and 30cm long (see Chapter:3 for details). The other coil is dedicated to the longitudinal guiding and deceleration (also shown in Fig.4.19), is the planner coil, which we have discussed in the previous section. The $27.8cm$ long planner coil consists of four wire modules. Each wire module is $13.9cm$ (12λ with $\lambda = 11.6mm$) long and made up of 32 individual copper wires of diameter 0.345mm. These 32 wires are divided into four sets (two for the red-set and other two for the yellow-set, in the figure) to produce the independent sine and a cosine magnetic waves. Then two modules are mounted above and the other two modules are mounted below the glass-tube. The wires are connected in such a way that the flown currents produces the sine magnetic field due to each red and yellow set of wires inside the glass-tube as mentioned in the previous section. The details of the coils and their dimensions is shown in Fig.4.34. After the completion of connections, there are 32 independent input-output for the whole $28cm$ long planner coil. For each input-output, the resistance and the inductance are $R = 0.6\Omega$ and $L = 2.5\mu H$, respectively. During the experiment the coils are heated up due to high current flow and they are cooled down by the dry air-flow near to the coils.

The other very important part of the experimental set-up is the driver electronics and other associated electronics to drive the decelerator. The major components used to

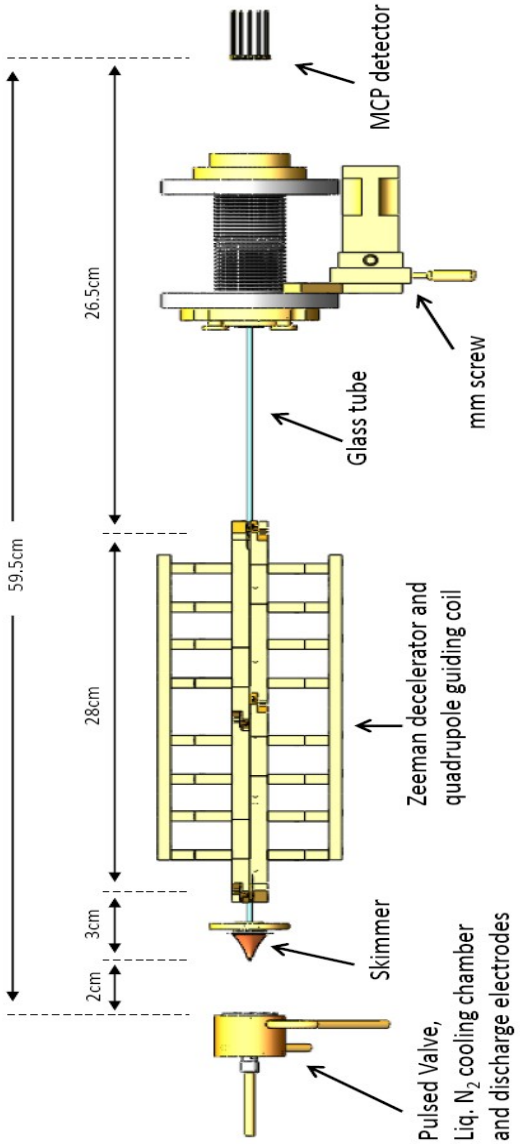

Figure 4.32: The schematic of the side-view of the experimental set-up dedicated to Zeeman deceleration. The supersonic beam metastable argon atoms are prepared using pulsed electric glow discharge of the ground state argon atoms. The discharge is carried out right after exit of the pulsed valve. After that, the beam passes through the skimmer and finally enters the glass tube (43cm long, 1.2mm and 3mm inner and outer diameter, respectively). The beam of metastable argon is decelerated by using 28cm long decelerator, place on the top and the bottom of the glass tube. The Time-Of-Flight (TOF) distribution of the argon atoms traveled over 59.5cm is measured using the MCP detector by recording the emitted electrons, once the metastable argon atoms impinge on it.

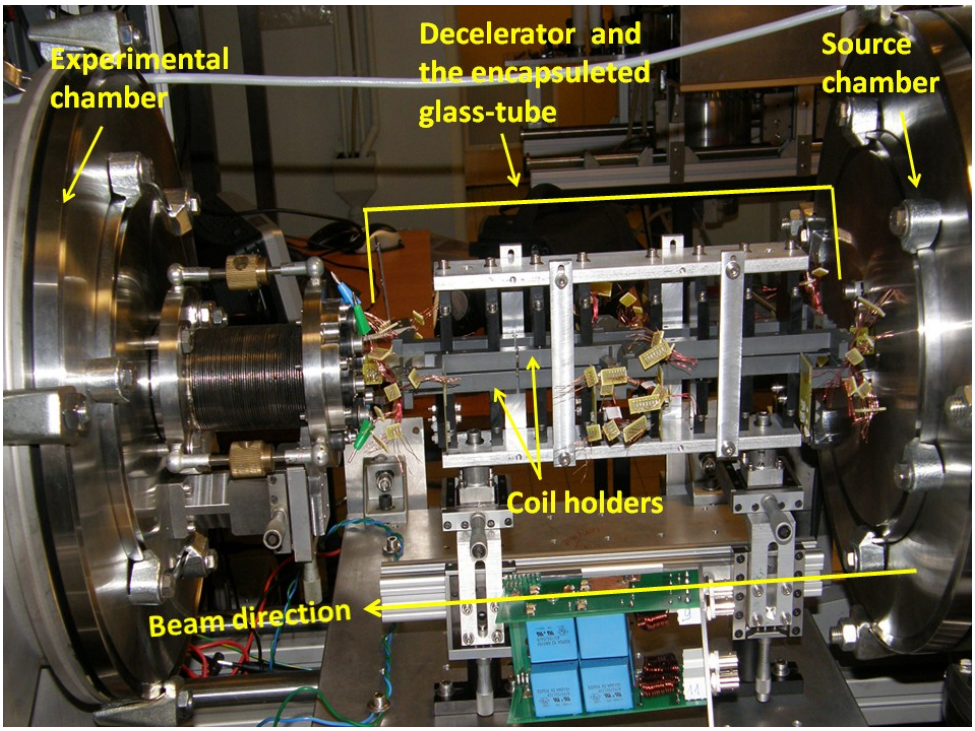

Figure 4.33: The picture of the part of the experimental set-up. The direction of the beam is from the right to the left. The chamber on the right is referred to the source chamber, contains the apparatus to produce the metastable beams like, pulsed valve, $Liq.N_2$ cooling chamber, the discharge electrodes, the skimmer etc. The chamber on the right is referred to the experimental chamber which contains the MCP detector. These two chambers are connected through a narrow glass-tube. The tube is encapsulated by the magnetic coils (the decelerator) and their holders.

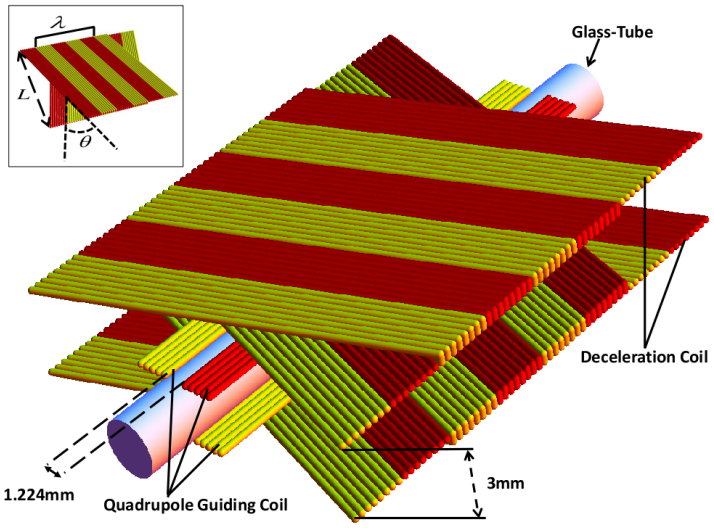

Figure 4.34: The schematic view of the coils used in the deceleration experiment. For the planner coil, the $\lambda = 11.6mm$ and $\theta = 35.752°$ are used with the copper wires of diameter $0.345mm$. The quadrupole guiding coil is installed underneath the planner coil also encasing the glass-tube.

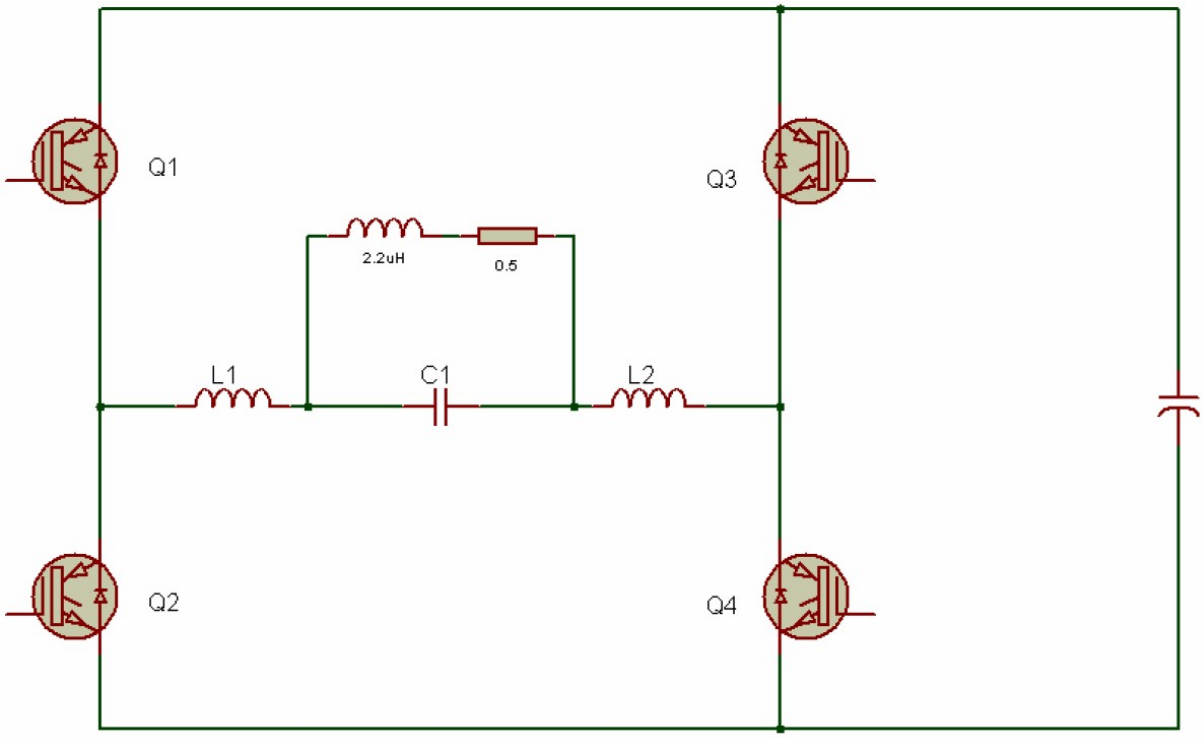

Figure 4.35: The oversimplified scheme for the electronic circuit to drive the planner coil.

produce high frequency AC current with high amplitude, are the power electronics devices. The power electronics device (e.g. inverter) with provided voltage supply variable both in frequency and magnitude, can generate at frequencies other than the supply frequency. In general, there are two basic types of inverter: Voltage-source inverter (VSI) and current-source inverter (CSI). The VSIs employ a DC link capacitor and provide a switched voltage wave form, are more common. The use Pulse Width Modulation (PWM) allows efficient and smooth operation for VSI. Furthermore, the frequency range is higher. The simpler requirement driving the power switches are the device must be capable of fast turn 'on' and turn 'off', higher maximum switching frequency, higher operating frequency and provide continually rising output power. The IGBT has the combined advantages of power MOSFET and bipolar power transistor which has simple gate control circuit design. It has fast switching capability up to 100kHz. It is extensively used in various applications where the voltage exceed 300V. The IGBT offers low saturation voltage and requires very little drive power.

The details of the electronics is out of the scope of this thesis as it is subjected to a patent. An over simplified scheme of the electronic circuit to drive one input-output wire is shown in Fig.4.35. The DC voltage is switched in a two-phase PWM (or *commande décalée*) inverter by four semiconductor switches (Q_1, Q_2, Q_3 *and* Q_4 in the figure) in order to obtain a pulse with two-phase AC voltage with the required frequency and amplitude. To produce high frequency AC one should take care of the limitations of the IGBTs are used due to their heating and dead time effects. Because of that its not possible to generate high frequency since it needs extremely fast modulation in voltage which can destroy the IGBTs. In this case we need to use *commande décalée* signal. But in all cases there present unwanted higher frequency components which has to be filtered out from the main output signal. A third-order filter is used for this purpose made up of the inductors $L1$, $L2$ and the capacitor $C1$ as shown in the Fig.4.35.

Since our decelerator is only 28cm long (the range of wave velocity is used from $464m/s$ to $370m/s$, to decelerate or longitudinal guide the beam) and the experiments are operated with in the range of 40kHz to 31kHz (quite high in driving frequency) we use the commande décalée signal to generate higher frequency. The profile of the generated $800\mu s$ long alternative current signal in the experiment, with the frequency of $34482.76Hz$ (or with a period of $29\mu s$) and the initial amplitude of 280A is shown in Fig.4.36. The current is measured by LeCroy CP500 current probe for each input wire (with the resistance $R = 0.6\Omega$ and inductance $L = 2.5\mu H$) connected with the driver. The observed slow decay in the current follows from the time constant $\tau = RC$ in a RC-circuit with resistance $R = 0.6\Omega$ and the capacitance $C = 2mF$. In a similar way an AC signal is produced which has constant frequency sweep (with time) just by commanding the electronic driver using an appropriate *commande décalée* signal.

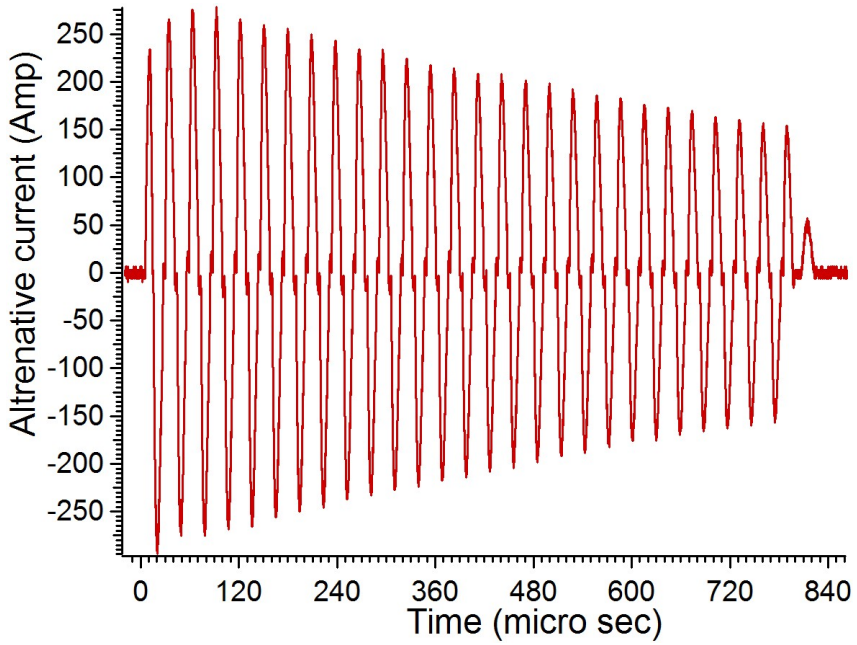

Figure 4.36: The experimentally observed AC current signal operating at the frequency $34482.76Hz$ from one wire output, connected with the electronic driver operated at 150V.

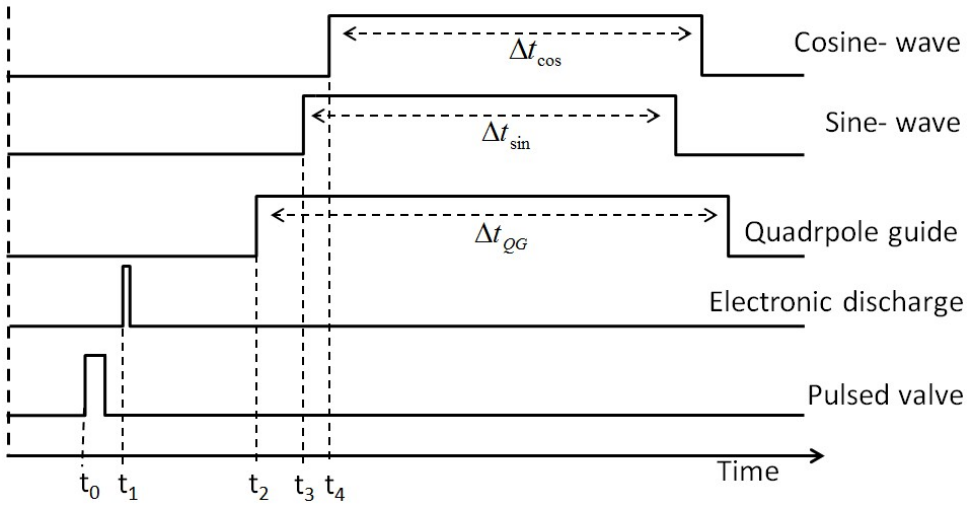

Figure 4.37: The figure illustrates the typical pulse sequences in each repetition of the deceleration experiment.

In general, the experiment is performed with the repetition rate of $0.33Hz$ to $0.25Hz$. The typical pulse sequences of the deceleration experiment is presented in Fig.4.37. The pulse sequence in each repetition of the deceleration experiment starts with $\sim 180\mu s$ valve pulse. The discharge voltage pulse of $\sim 15\mu s$ long is applied for the electric glow discharge. The typical time delay $(t_1 - t_0)$ between beginning of the valve and the discharge voltage pulse is $\sim 75\mu s$. After $\sim 50\mu s$ (which is $t_2 - t_1$) from the beginning of the discharge pulse the $\triangle t_{QG} \sim 750\mu s$ long quadrupole guiding pulse is applied. The beginning (t_3) of the pulse for the sine wave is applied depending on the initial velocity chosen for the deceleration or for the longitudinal guiding. As for the deceleration from the initial velocity $400m/s$ (or for longitudinal guiding at $400m/s$) the sine pulse is applied at $t_3 - t_1 = 178.64\mu s$ while the length of the pulse depends on the rate of deceleration for example to decelerate from $400m/s$ to $370m/s$, the length of the pulse is $\triangle t_{sin} \sim 700\mu s$. The pulse for the cosine wave has the same length of the sine wave in time except has delayed a certain time (depending on the initial frequency of the applied AC) to make phase difference of $2\pi\nu(t_4 - t_3) = \pi/2$ between the sine and cosine waves. Since the typical repetition rate is of $0.25Hz$, the high energy capacitors for the electronics are charged after pulse sequence (which last for $\sim 1ms$).

4.5 Experimental Results, Simulations and Discussion

As the first attempt to demonstrate the deceleration ability of the decelerator, we have performed the longitudinal guiding along with the radial confinement (which is a 3D-guiding) of metastable argon atoms in $^3P_2$ quantum state. The ability to 3D-guide the atoms automatically indicates that the decelerator is capable of exerting force on them and consequently resists their longitudinal spreading (as the beam has non-zero velocity spread) of the beam and the part this force can be used for deceleration. After the first demonstration of the 3D-guiding we have carried out our first deceleration experiment, successfully.

To analyze and verify the experimental signals we performed 3D-trajectory simulations. The magnetic fields are calculated by *Mathematica Program* separately and imported, in a grid (with 10 grid-points/mm in x,y and z-directions) to the 3D-trajectory simulation program (in C++ programing language). The magnetic field is interpolated using linear interpolation which is used to calculated atoms motions by numerically (using Runge-Kutta Nyström algorithm) integrating the equation of motion.

4.5.1 The 3D-guiding

By keeping the frequency of the driven AC current in the decelerator to be constant, we produce a magnetic wave with a constant velocity along the beam axis. It eventually traps a beam packet with a mean velocity equal to the velocity of the wave and with the longitudinal velocity spread depending on the trap-depth. As a first experimental attempt, we longitudinally guide a beam of metastable argon in $^3P_2$ (in LFS) quantum state with the mean velocity of $468m/s$ and the longitudinal velocity spread of $40m/s$ (8.5% of the mean velocity). The magnetic wave is produced by flowing AC current with 300A and a constant driving frequency to the half of the wires (four wires instead of eight wires) of the planner coil. The magnetic field amplitude is approximately half to that of the eight wires coil geometry, in this case. The DC current in quadrupole guiding coil is 75A. The velocity of the magnetic waves with which the longitudinal guiding have been carried out, are $464m/s$, $440.8m/s$ and $429.6m/s$ which correspond to the driving AC frequency of $40kHz$, $38kHz$ and $37.037kHz$, respectively.

For the experiment with the parameters mentioned above, the velocity acceptance (v_{trap}) of the decelerator is $\sim 14m/s$ for the argon atoms in $^3P_2, m_j = 2$ quantum state. The observed experimental results are shown in the Fig.4.38. The fraction of the beam is 3D-guided depends both on the mean velocity, longitudinal velocity spread of the beam and the velocity at which the guiding is carried out. In the experiment mentioned above the fraction of the beam which is 0.16 which is guided at $464m/s$ while its little less

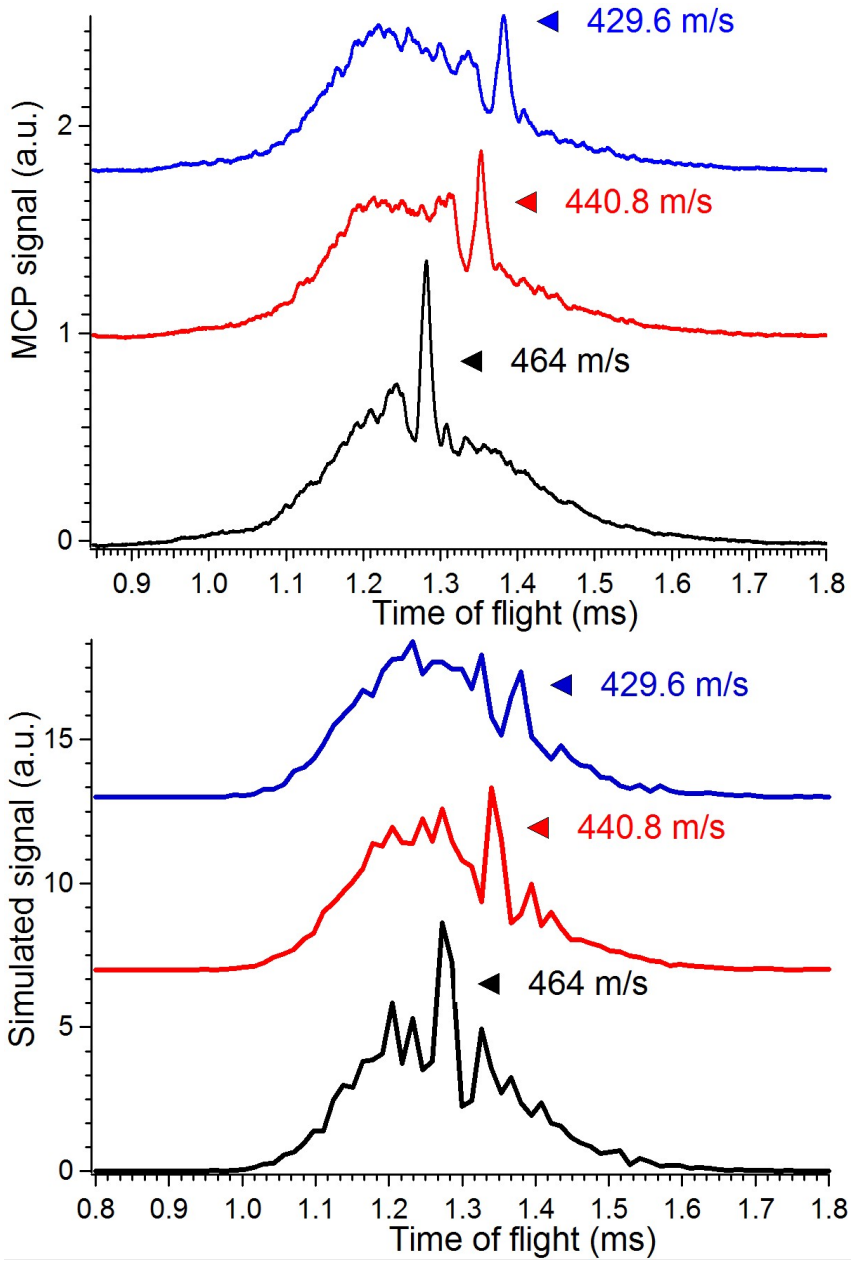

Figure 4.38: The traces in the *figure on the top panel* represents the observed experimental results for 3D-guiding of an argon beam of the mean velocity of $468m/s$ and the longitudinal velocity spread of $40m/s$. The 3D-guidings have been carried out at $464m/s$ (in black trace), $440.8m/s$ (in red trace) and $429.6m/s$ (in blue trace) which are correspond to the driving AC current frequency of $40kHz$, $38kHz$ and $37.037kHz$, respectively. The indicated intense peaks (for $464m/s$ at $1.2823ms$, for $440.8m/s$ at $1.353ms$ and for $429.6m/s$ at $1.3823ms$) in the TOF-signal correspond to the guided beam packets. The traces in the *figure on the bottom panel* represent the corresponding simulated signals. The *black*, *red* and *blue* traces are the simulated 3D-guiding signals at $464m/s$, $440.8m/s$ and $429.6m/s$, respectively.

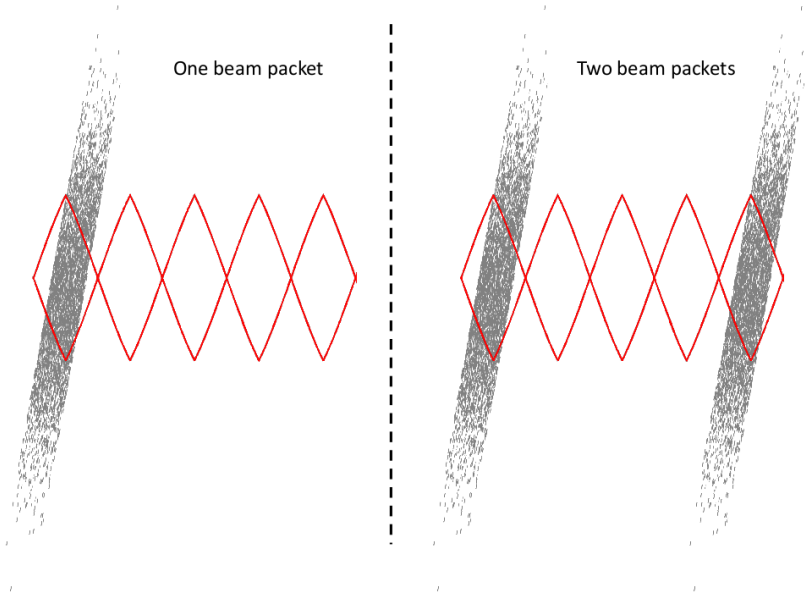

Figure 4.39: The chain of traps along the longitudinal direction which are indicated by the enclosed area of the separatrix, in red line. The *figure on the left* corresponds to a 3D-guiding of one beam packet while the *figure on the right* corresponds to simultaneous 3D-guiding of two beam packets separated by 2λ in the longitudinal direction.

(~ 0.1) for the other guiding velocities ($440.8m/s$ and $429.6m/s$). In all these cases the velocity spread (FWHM) of the guided beam packets is $4.6 \pm 0.03m/s$ which corresponds to the longitudinal temperature of $100mK$.

When the quadrupole guide is turned-on the decelerator produces a chain of real 3D-traps in every $\lambda/2$ distances along the beam axis, moving with the velocity of the magnetic wave. So, depending on the initial length in position (or in time) of the beam pulses and the relative separation between them, we can fill either one trap or multiple traps, as is shown in the Fig.4.39. In Fig.4.40, we present the experimental TOF distribution resulting from simultaneous 3D-guiding of two beam packets separated by 2λ (with $\lambda = 11.6mm$) along the beam axis. These two beam packets separated by 2λ, are produced by discharging a argon beam pulse resulting from the *Liq.* N_2 cooled valve with two consecutive short ($12\mu s$ long) electric discharge pulse separated by $50\mu s$. The 3D-guiding has been performed at $464m/s$. The corresponding signal of the two 3D-guided packets are indicated by the two strong peaks in the TOF signal separated by $50\mu s$ which is equal to the required time to travel 2λ with $464m/s$ mean velocity. The longitudinal temperatures of these packets are exactly same ($100mK$). The 3D-trajectory simulation supporting the experimental results are also shown in the Fig.4.40.

On addition to the signal increased at the guided velocity region in the TOF signal,

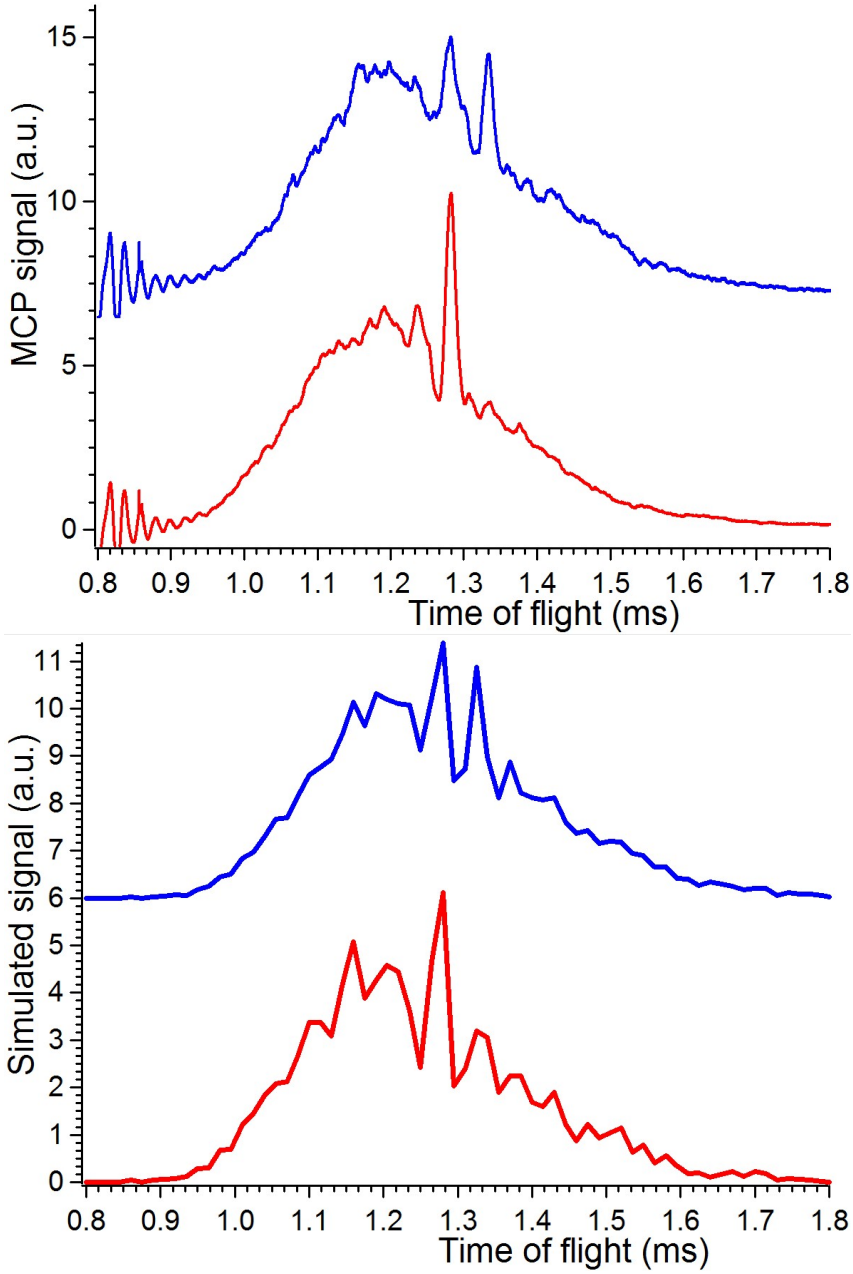

Figure 4.40: The *figure on the top panel* shows the observed experimental signal (from an argon beam of mean velocity $480m/s$ and a velocity spread of $55m/s$) for 3D-guiding at $464m/s$ of one beam packet (the lower trace in red) and of two beam packets (the upper trace in blue) separated by $50\mu s$. The corresponding signals for the guided packets with a longitudinal temperature of $100mk$ are represented by the huge spikes in TOF-signal. The *figure on the bottom panel* shows the simulated signals, with the same experimental conditions, are in well agreement with the experimental signals. The lower trace in red and the upper trace in blue are correspond to the one beam packet and two beam packets guided at $464m/s$.

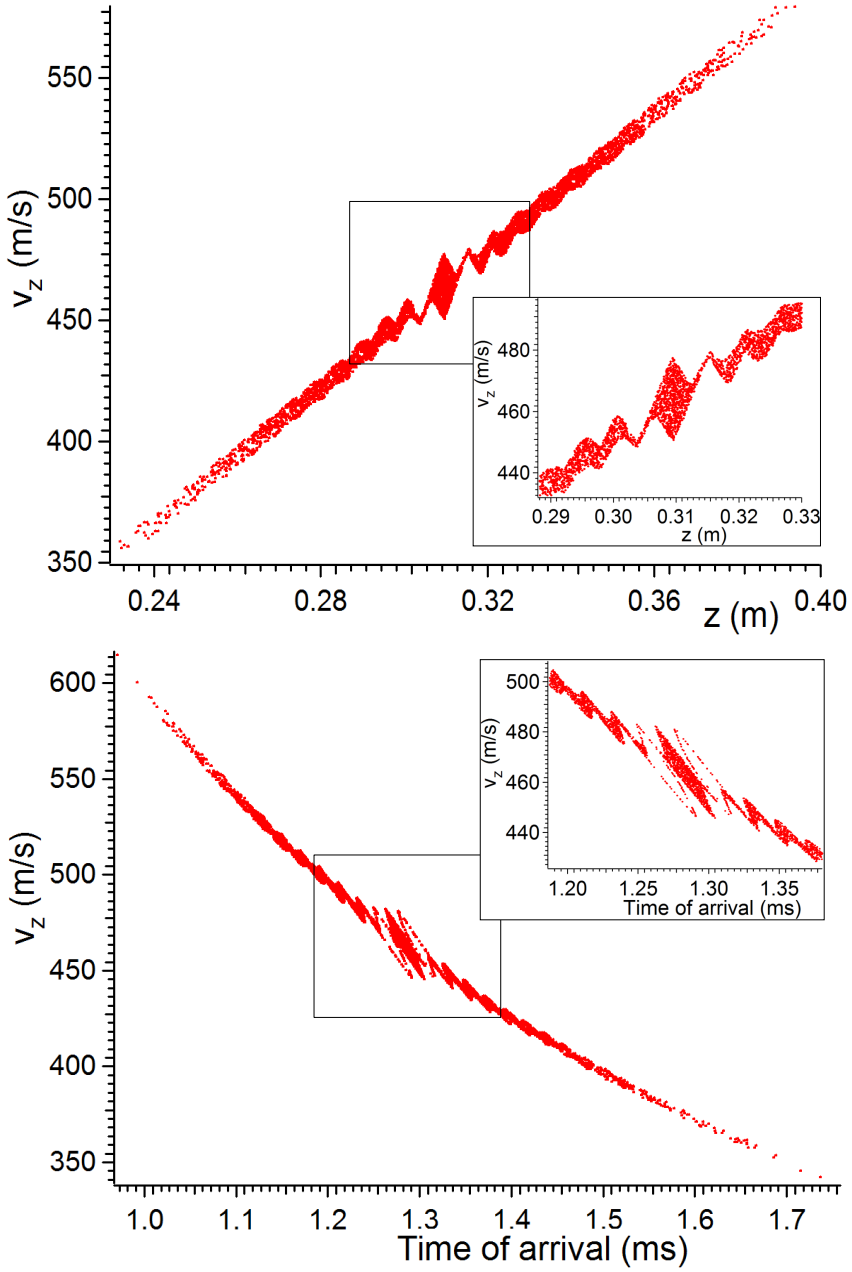

Figure 4.41: The *figure on the top panel* shows the phase space picture (considering only the longitudinal motion and at a time $0.71ms$) of the atoms right after the exit of the decelerator ($32.8cm$ far from the valve), simulated for an argon ($^3P_2$, $m_J = 2$) beam of mean velocity $468m/s$, a longitudinal velocity spread $40m/s$ and 3D-guided at $464m/s$. The *figure on the bottom panel* shows the time-of-arrival at the detector (which is $59.5cm$ far from the valve) with respect to the longitudinal position, z. Due to the longitudinal bunching the atoms that are gathered together at the position of the saddle points (at every $\lambda/2 = 5.9mm$ for the figure on top and at every $\lambda/2v = 12.5\mu s$ for the bottom figure), give rise the higher intensities (the spikes) in the TOF-signals.

the distribution is structured with locally intense peaks (spikes) around the guided packet signal due to the presence of moving chain of traps. The atoms with higher velocity than v_{trap} are slowed down during their passage over the saddle points (potential maximums) between the traps and acquire a velocity which is close to the velocity of the trap and takes much longer time to pass the saddle point. As a result, the probability becomes higher finding the atoms at the position of the saddle points and yield the locally higher intensities in the TOF signal. When the velocity of the atoms are much higher or much lower than the guiding velocity, the we do not expect to see the spike as the atoms spend little time to pass the saddle point and the probability finding them near the saddle point does not increase. These are also well reproduced in the simulation as shown in the Fig.4.41 representing the time-of-arrival to the detector ($59.5cm$ far from the valve) and the phase space picture. The time difference (which is the time taken by the atoms to fly $\lambda/2$) between the spikes in the TOF traces are given by $\lambda/2v$ with the velocity v at which the 3D-guiding is performed.

4.5.2 Deceleration

The next steps to the 3D-guiding were the decelerations. Once a beam packet of atoms are captured in a magnetic trap we can gradually reduce the trap velocity which results in deceleration of the captured beam packet. We already have mentioned that if the strength of deceleration is too high that results a lower trap depth due to the deformation of the trap potential. We need to make a compromise between deceleration strength and the number of atoms to be decelerated in the beam packet. For the first demonstration, we have decelerated the metastable argon beams first, from the initial velocity of $400m/s$ to the final velocities $380m/s$ and $370m/s$ and second, from the initial velocity $392m/s$ to the final velocity $365m/s$ with the AC 300A flown in the planner coil where four wires are used (same as for 3D-guiding cases). In all cases we use 75A pulsed DC current in the quadrupole guiding coil. The deceleration experiment from $400m/s$ to $380m/s$ and $400m/s$ to $370m/s$ are performed with an argon beam of the mean velocity $472m/s$ and the longitudinal velocity spread $42.5m/s$. The initial frequency of the driven AC frequency is $34482.76Hz$ for both the cases while the sweeping rates are $-1233330Hz/s$ and $-1826280Hz/s$, respectively. To compare the decelerated signals we also performed a 3D-guiding experiment at $400m/s$ with the constant driven AC frequency $34482.76Hz$. The experimental results are presented in the *top panel* of the Fig.4.42. The peaks appeared at $1.487ms$, $1.51ms$ and $1.52ms$ in the TOF-signals of the figure are correspond to 3D-guided beam packet at $400m/s$, the decelerated beam packet from $400m/s$ to $380m/s$ and from $400m/s$ to $370m/s$, respectively.

The other deceleration experiment from $392m/s$ to $365m/s$ on the same argon beam

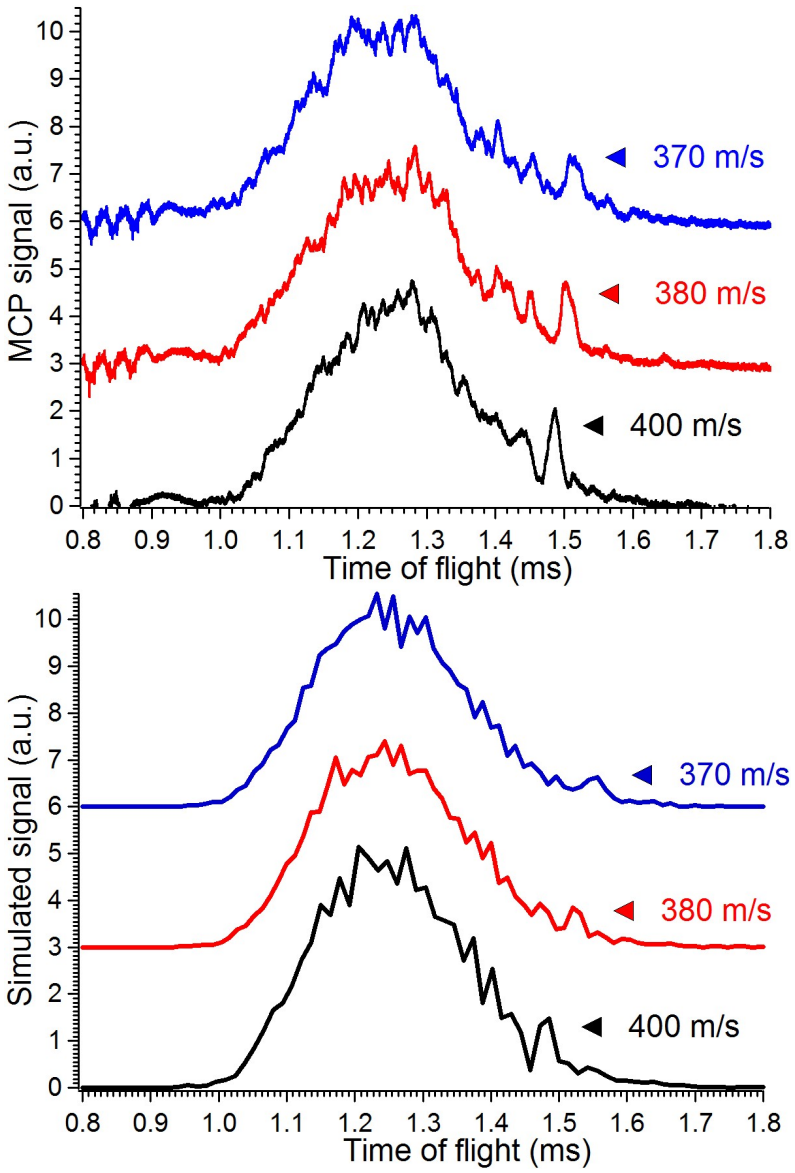

Figure 4.42: The observed experimental TOF-signals and the simulated TOF-signals for the deceleration experiments with a metastable argon beam (with mean velocity $472m/s$ and has a longitudinal velocity spread of $42.5m/s$). In the *figure on the top panel*, the trace in black represents the 3D-guided TOF at $400m/s$ while the traces in red and blue represent the decelerated TOF from $400m/s$ to $380m/s$ and $400m/s$ to $370m/s$, respectively. The *figure in the bottom panel* represents the corresponding simulated TOF-signals with the same experimental conditions. Similarly, the 3D-guiding signal is indicated by the trace in black while the for the deceleration from $400m/s$ to $380m/s$ and $400m/s$ to $370m/s$ are indicated by the traces in red and blue, respectively. The peaks, resulted from the 3D-guided and decelerated beam packets are indicated with the markers.

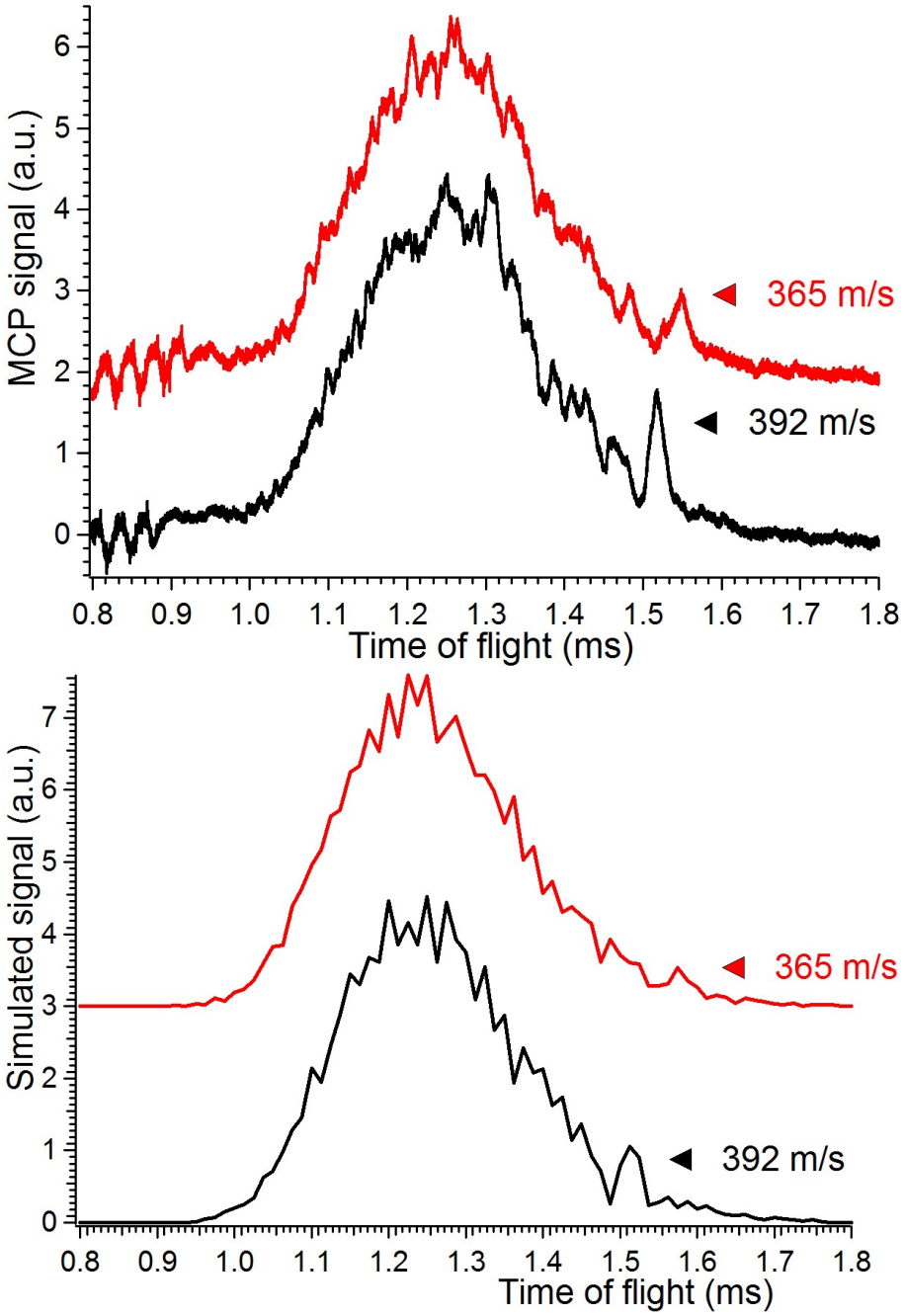

Figure 4.43: The observed experimental TOF-signals and the simulated TOF-signals for the deceleration experiments with a metastable argon beam (with mean velocity $472m/s$ and has a longitudinal velocity spread of $42.5m/s$). In the *figure on the top panel*, the trace in black represents the 3D-guided TOF at $392m/s$ while the traces in red represents the decelerated TOF from $392m/s$ to $365m/s$. The *figure in the bottom panel* represents the corresponding simulated TOF-signals with the same experimental conditions. The 3D-guiding signal is indicated by the trace in black while the for the deceleration from $392m/s$ to $365m/s$ is indicated by the trace in red. The peaks, resulted from the 3D-guided and decelerated beam packets are indicated with the markers.

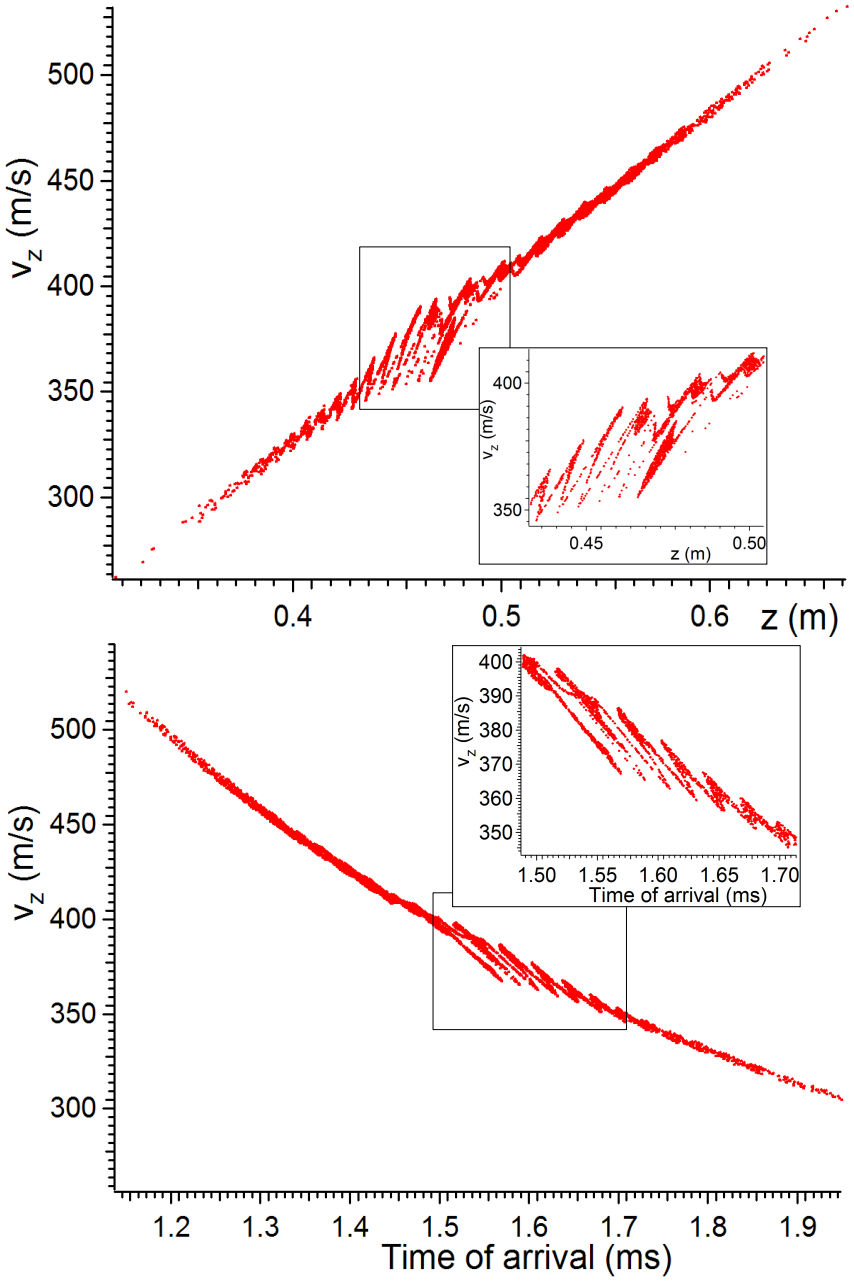

Figure 4.44: The *figure on the top panel* represents the phase-space distribution after the deceleration with considering only the longitudinal motion from $400m/s$ to $370m/s$, simulated for argon (in $^3P_2$, $m_J = 2$ quantum state) beam. The decelerated atoms are correspond to the dense region of the phase space plot centering at $370m/s$. The *figure on the bottom panel* shows the distribution of the longitudinal velocity with respect to the time-of-arrival (TOA) to the detector which is also simulated for argon (in $^3P_2$, $m_J = 2$ quantum state) beam. The dense region in the figure centering at $370m/s$ is indicating the decelerated atoms.

has also been performed with the initial driven AC frequency $33793.1Hz$ and with the rate of frequency sweep $-1615900Hz/s$. To compare, the 3D-guiding experiment has also been done with the same argon beam at $392m/s$. The experimental results for the deceleration from $392m/s$ to $365m/s$ are presented in the *top panel* of the Fig.4.43. In the TOF-signals of the figure, the peak appeared at $1.52ms$ represents the 3D-guided beam packet at $392m/s$ while the peak corresponds to $1.55ms$ is the decelerated from $392m/s$ to $365m/s$ beam packet. In the case of 3D-guiding (both at $400m/s$ and $392m/s$) the longitudinal temperature of the beam is $100mK$. The details of the 3D-guided and the decelerated beam packets are presented in the Table.4.2.

Initial velocity	Final velocity	Fraction of the beam 3D-guided or decelerated	Longitudinal temperature
400m/s	400m/s	0.037	100mK
400m/s	380m/s	0.036	...
400m/s	370m/s	0.035	...
392m/s	392m/s	0.036	100mK
392m/s	365m/s	0.022	...

Table 4.2: The characteristics of the 3D-guided and the decelerated beam packets in the experiments.

The corresponding 3D-trajectory simulations verifying the experimental results are shown in the *bottom panel* of the Fig.4.42 and Fig.4.43 by considering same experimental conditions, are in well agreement. One must note from the experimental results that, the peaks due to the decelerated beam packets have width which are either same or more than that of the 3D-guided peaks. In fact, the peaks corresponding to the decelerated beam packets should be narrower in width (lower longitudinal temperature) due to lower trap depth. That can be explained with the help of the Fig.4.44 which illustrates the phase space position (*on top panel*) and the time-of-arrival (TOA) with respect to the longitudinal velocity (*on the bottom panel*) at the detector, for deceleration of argon atoms (in $^3P_2,\ m_J = 2$) form $400m/s$ to $370m/s$. As is seen from the figure, the time (which is $1.55ms$) required for decelerated beam packet to arrive at the detector is also same for the atoms (which are not primarily captured in the trap and decelerated) with a velocity of $384m/s$ and reach the detector at the same time. Consequently, the resulting appeared peak represents both the atoms which are effectively decelerated as well as the atoms with velocity $384m/s$ (with little more or less). In the case of deceleration, as the velocity of the potential is reduced with time. So, the initially slow atoms (with lower velocity than the potential well) can have closer velocity to the potential well and even after a

certain time, they can be captured in a the trap or they can be gathered around the saddle points of the periodic potential, finally giving rise to the spikes in the TOF-signals. But for the atoms with initially higher velocity than the potential well, increase their relative velocity to the potential well with time and finally stay unaffected. For long decelerator or for a deceleration with higher strength all these effects should be disappeared from the TOF-signal.

4.5.3 The Transverse Motion

We already have seen that the resultant transverse focusing force due to the planner coil and the quadrupole guiding coil, is not cylindrically symmetric. The force along the y-direction is much stronger than the force along x-direction. So, one expect to have a non-cylindrical 3D-guided beam (in velocity) at the end of the decelerator which in fact the case as shown in Fig.4.45 (a) and (b). The final beam has higher velocity component along y-direction than along x-direction. The potential is highly anharmonic in the radial directions. Due to the rapid time-variation of the potential along the radial directions (in the moving frame of the potential well), the trajectories in phase space are not closed and can cross each other (see Fig.4.45 (e) and (f)), as has been seen from numerical simulations. The simulations also show that, the atoms are transversally guided throughout the $27.8cm$ long decelerator as indicated by the higher number of phase space points located centering the zero radial position and velocity (see Fig.4.45 (c) and (d)). The velocity acceptances (see Fig.4.45 (c) and (d)) in x-direction and y-direction are $\sim 2m/s$ and $\sim 4m/s$, respectively for argon atoms in $^3P_2,\ m_J = 2$ with an AC $300A$ in the planner coil and $75A$ DC in the quadrupole guide. In the case of deceleration, all these above mentioned characteristics are also present.

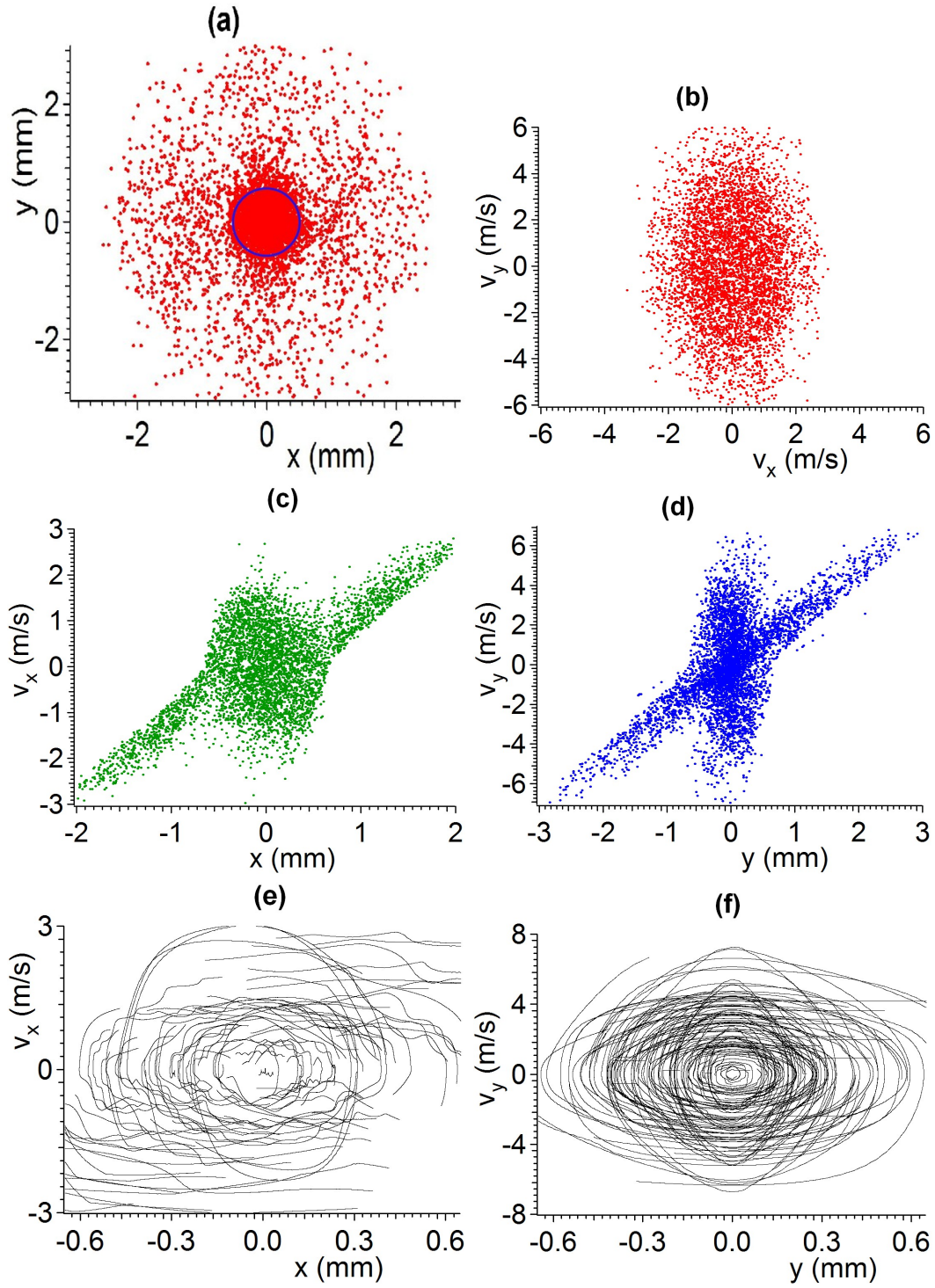

Figure 4.45: The figure represents the transversal motions of the atoms during the course of 3D-guiding, in the decelerator. The figure (a) and (b) illustrate the shape of the beam in position (the glass tube is indicated by the blue circle) and velocity, respectively at the end of the decelerator. The figure (c) and (d) represents the phase space distribution along x and y-directions, respectively. The phase space evolution of the atoms during the course of 3D-guiding are shown in figure (e) and (f).

4.6 Conclusion and Outlook

The proof-of-principle experimental results presented in this chapter clearly demonstrate the potential of the Zeeman decelerator to transfer the initial high phase space densities from moving atomic frame to the laboratory frame or to arbitrary (low) velocities. This demonstrated new deceleration technique exploits continuously modulated magnetic fields to produce a traveling potential. It has been shown that the paramagnetic atoms can be guided at constant velocity (3D-guided) and also they can be decelerated. A metastable argon (in $^3P_2$) beam packet has been 3D-guided at $464m/s$, $440.8m/s$ and $429.6m/s$ with the longitudinal temperature of $100mK$. The ability to simultaneous 3D-guide of two beam packets indicates the potential of the decelerator to 3D-trap and decelerate multiple beam packets in a chain along the beam axis. The deceleration experiments have been carried out for metastable argon (in $^3P_2$) beam decelerated from initial velocities $400m/s$ and $392m/s$ to the final velocities $380m/s$, $370m/s$ and $365m/s$, respectively.

The obvious next step in the experiment would be to further investigations of deceleration process such as study the effect of transverse motions of the atoms in the efficiency of the deceleration process which have been seen in the multistage Zeeman decelerator [129]. Once the detailed study of the decelerator is done, the other paramagnetic species like Ne, H, D, T, O_2, NO, NO_2 and ClO_2 can be decelerated.

A particular interesting feature is that the atoms are confined in three dimensions to form the 3D-trap during the deceleration. The decelerated atoms can be stopped by reducing the modulation frequency to zero while the atoms are still trapped in three dimensions, which indeed requires a longer decelerator and improved electronics for the final stage of the decelerator. The calculations shows that the molecular NO could be brought to stand still with $90cm$ long decelerator while the atomic H could be stopped with $7cm$ long decelerator. As the radial confinement of the atoms are done by the independently implementing the quadrupole guide, a bent decelerator can also be realized which gives rise to the possibility to merge two or more beams. This new decelerator can provide a very good starting point for various experiments such as, molecular fountain, high resolution spectroscopy and various cold scattering experiments with multiple beam packets.

Bibliography

[1] E. P. Wigner. Einige folgerungen aus der schrödingerschen theorie für die termstrukturen. *Z. Phys.*, 43:624, 1927.

[2] H. A. Kramers. *Proc. Acad. Sci. Amsterdam.*, 40,:814, (1937).

[3] T. D. Lee and C. N. Yang. Question of parity conservation in weak interactions. *Phys. Rev.*, 104(1):254, 1956.

[4] C. S. Wu, E. Ambler, R. W. Hayward, D. D. Hoppes, and R. P. Hudson. Experimental test of parity conservation in beta decay. *Phys. Rev.*, 105:1413, 1957.

[5] L. Landau. On the conservation laws for weak interactions,. *Nucl. Phys.*, 3:127, 1957.

[6] J. H. Christenson, J. W. Cronin, V. L. Fitch, and R. Turlay. Evidence for the 2π decay of the K_2^0 meson. *Phys. Rev. Lett.*, 13(4):138, 1964.

[7] James W. Cronin. CP symmetry violation—the search for its origin. *Rev. Mod. Phys.*, 53:373–383, 1981.

[8] Val L. Fitch. The discovery of charge-conjugation parity asymmetry. *Rev. Mod. Phys.*, 53:367–371, 1981.

[9] K. Kleinknecht. CP violation and K_0 decay,. *Annu. Rev. Nucl. Sci.*, 26,:1, (1976).

[10] L. Wolfenstein. Present status of CP violation,. *Annu. Rev. Nucl. Sci.*, 36,:137, (1986).

[11] S. L. Glashow. Partial symmetries of weak interactions. *Nucl. Phys.*, 22:579, 1961.

[12] Steven Weinberg. A model of leptons. *Phys. Rev. Lett.*, 19:1264–1266, 1967.

[13] A. Salam. *Elementary Particle Theory: Relativistic Groups and Analyticity (8th Nobel Symp.)*. Stockholm: Almqvist and Wicksell, 1968.

[14] C. Itzykson and J. B. Zuber. *Quantum Field Theory.* New York: McGraw-Hill, 1980.

[15] B. Odom, D. Hanneke, B. D'Urso, and G. Gabrielse. New measurement of the electron magnetic moment using a one-electron quantum cyclotron. *Phys. Rev. Lett.*, 97(3):030801, Jul 2006.

[16] G. Gabrielse, D. Hanneke, T. Kinoshita, M. Nio, and B. Odom. New determination of the fine structure constant from the electron g value and qed. *Phys. Rev. Lett.*, 97(3):030802, Jul 2006.

[17] Peter J. Mohr and Barry N. Taylor. Codata recommended values of the fundamental physical constants: 2002. *Rev. Mod. Phys.*, 77(1):1–107, Mar 2005.

[18] C. Schwob, L. Jozefowski, B. de Beauvoir, L. Hilico, F. Nez, L. Julien, F. Biraben, O. Acef, J.-J. Zondy, and A. Clairon. Optical frequency measurement of the $2s-12d$ transitions in hydrogen and deuterium: Rydberg constant and lamb shift determinations. *Phys. Rev. Lett.*, 82(25):4960–4963, Jun 1999.

[19] Marie-Anne Bouchiat and Claude Bouchiat. Parity violation in atom. *Rep. Prog. Phys.*, 60:1351, 1997.

[20] V. V. Flambaum and D. W. Murray. Anapole moment and nucleon weak interactions. *Phys. Rev. C*, 56(3):1641–1644, 1997.

[21] S. G. Porsev, K. Beloy, and A. Derevianko. Precision determination of electroweak coupling from atomic parity violation and implications for particle physics. *Phys. Rev. Lett.*, 102:181601, 2009.

[22] C. S. Wood, S. C. Bennett, D. Cho, B. P. Masterson, J. L. Roberts, C. E. Tanner, and C. E. Wieman. Measurement of parity nonconservation and an anapole moment in cesium. *Science*, 275:1759, 1997.

[23] K. Tsigutkin, D. Dounas-Frazer, A. Family, J. E. Stalnaker, V. V. Yashchuk, and D. Budker. Observation of a large atomic parity violation effect in ytterbium. *Phys. Rev. Lett.*, 103(7):071601, 2009.

[24] D. DeMille, S. B. Cahn, D. Murphree, D. A. Rahmlow, and M. G. Kozlov. Using molecules to measure nuclear spin-dependent parity violation. *Phys. Rev. Lett.*, 100:023003, 2008.

[25] V. V. Flambaum and J. S. M. Ginges. Resonance reactions and enhancement of weak interactions in collisions of cold molecules. *Phys. Rev. A*, 74(2):025601, 2006.

[26] Marie-Anne Bouchiat. Linear stark shift in dressed atoms as a signal to measure a nuclear anapole moment with a cold-atom fountain or interferometer. *Phys. Rev. Lett.*, 98(4):043003, 2007.

[27] V. S. Letokhov. On difference of energy levels of left and right molecules due to weak-interactions. *Physics Letter A*, 53:275, 1975.

[28] D. W. Rein. Some remarks on parity violating effects of intramolecular interations. *J. Mol. Evol.*, 4:15, 1974.

[29] M. Ziskind, C. Daussy, T. Marrel, and Ch. Chardonnet. Improved sensitivity in the search for a parity-violating energy difference in the vibrational spectrum of the enantiomers of chfclbr. *Eur. Phys. J. D*, 20:219–225, 2002.

[30] E. M. Purcell and N. F. Ramsey. On the possibility of electric dipole moments for elementary particles and nuclei. *Phys. Rev.*, 78:807, 1950.

[31] L. R. Hunter. Test of time revarsal invariance in atoms, molecule and the neutron. *Science*, 252:73, 1991.

[32] E. Hinds and B. Sauer. Electron dipole moments. *Physics World*, page 37, April 1997.

[33] S. M. Barr. A review of CP violation in atoms. *Int. J. Mod. Phys. A.*, 8:209, 1993.

[34] Stephen Barr, Gino Segrè, and H. Arthur Weldon. Magnitude of the cosmological baryon asymmetry. *Phys. Rev. D*, 20:2494–2498, 1979.

[35] B. C. Regan, Eugene D. Commins, Christian J. Schmidt, and David DeMille. New limit on the electron electric dipole moment. *Phys. Rev. Lett.*, 88:071805, 2002.

[36] P. G. H. Sandars. *Phys. Lett.*, 14:194, 1965.

[37] J. J. Hudson, B. E. Sauer, M. R. Tarbutt, and E. A. Hinds. Measurement of the electron electric dipole moment using YbF molecules. *Phys. Rev. Lett.*, 89:023003, 2002.

[38] D. DeMille, F. Bay, S. Bickman, D. Kawall, D. Krause, S. E. Maxwell, and L. R. Hunter. Investigation of PbO as a system for measuring the electric dipole moment of the electron. *Phys. Rev. A*, 61:052507, 2000.

[39] Amar C. Vutha, Wesley C. Campbell, Yulia V. Gurevich, Nicholas R. Hutzler, Maxwell Parsons, David Pattersonand Elizabeth Petrik, Benjamin Spau, John M.

Doyle, Gerald Gabrielse, and David DeMille. Search for the electric dipole moment of the electron with thorium monoxide. *arXiv:0908.2412v1 [physics.atom-ph].*

[40] V. A. Dzuba, V. V. Flambaum, J. S. M. Ginges, and M. G. Kozlov. Electric dipole moments of Hg, Xe, Rn, Ra, Pu, and TlF induced by the nuclear Schiff moment and limits on time-reversal violating interactions. *Phys. Rev. A*, 66:012111, 2002.

[41] Harry M. Quiney, Jon K. Laerdahl, Knut Fægri, and Trond Saue. Ab initio dirac-hartree-fock calculations of chemical properties and *pt*-odd effects in thallium fluoride. *Phys. Rev. A*, 57:920–944, 1998.

[42] M. G. Kozlov, A. V. Titov, N. S. Mosyagin, and P. V. Souchko. Enhancement of the electric dipole moment of the electron in the BaF molecule. *Phys. Rev. A*, 56:R3326–R3329, 1997.

[43] Boris Ravaine, Sergey G. Porsev, and Andrei Derevianko. Marked influence of the nature of the chemical bond on CP-violating signature in molecular ions HBr^+ and HI^+. *Phys. Rev. Lett.*, 94:013001, 2005.

[44] T. A. Isaev, A. N. Petrov, N. S. Mosyagin, and A. V. Titov. In search of the electron electric dipole moment: Relativistic correlation calculations of the P,T-violating effect in the ground state of HI^+. *Phys. Rev. Lett.*, 95(16):163004, 2005.

[45] Dima Egorov, Jonathan D. Weinstein, David Patterson, Bretislav Friedrich, and John M. Doyle. Spectroscopy of laser-ablated buffer-gas-cooled PbO at 4 k and the prospects for measuring the electric dipole moment of the electron. *Phys. Rev. A*, 63:030501, 2001.

[46] Jean-Philippe Uzan. The fundamental constants and their variation: observational and theoretical status. *Rev. Mod. Phys.*, 75(2):403–455, 2003.

[47] T. M. Fortier, N. Ashby, J. C. Bergquist, M. J. Delaney, S. A. Diddams, T. P. Heavner, L. Hollberg, W. M. Itano, S. R. Jefferts, K. Kim, F. Levi, L. Lorini, W. H. Oskay, T. E. Parker, J. Shirley, and J. E. Stalnaker. Precision atomic spectroscopy for improved limits on variation of the fine structure constant and local position invariance. *Phys. Rev. Lett.*, 98(7):070801, 2007.

[48] Eric R. Hudson, H. J. Lewandowski, Brian C. Sawyer, and Jun Ye. Cold molecule spectroscopy for constraining the evolution of the fine structure constant. *Phys. Rev. Lett.*, 96(14):143004, Apr 2006.

[49] Michael T. Murphy, Victor V. Flambaum, Sébastien Muller, , and Christian Henkel. Strong limit on a variable proton-to-electron mass ratio from molecules in the distant universe. *Science*, 320:1611, 2008.

[50] M. H. Anderson, J. R. Ensher, M. R. Matthews, C. E. Wieman, and E. A. Cornell. Observation of Bose-Einstein condensation in a dilute atomic vapor. *Science*, 269:198–201, 1995.

[51] Andrew G. Truscott, Kevin E. Strecker, William I. McAlexander, Guthrie B. Partridge, and Randall G. Hulet. Observation of fermi pressure in a gas of trapped atoms. *Science*, 291:2570–2572, 2001.

[52] Markus Greiner, Olaf Mandel, Tilman Esslinger, Theodor W. Hänsch, and Immanuel Bloch. Quantum phase transition from a superfluid to a Mott insulator in a gas of ultracold atoms. *Nature*, 415:39–44, 2002.

[53] E. Bodo and F. A. Giaturco. Features of chemical reactions at vanishing kinetic energy: the presence of internally "hot" reagents. *Eur. Phys. J. D*, 31:423, 2004.

[54] A. V. Avdeenkov and John L. Bohn. Linking ultracold polar molecules. *Phys. Rev. Lett.*, 90(4):043006, Jan 2003.

[55] N. Balakrishnan and A. Dalgarno. Chemistry at ultracold temperatures. *Chem. Phys. Lett.*, 341:653, 2001.

[56] T. Takayanagi and Y. Kurosaki. van der Waals resonances in cumulative reaction probabilities for the $F + H_2$, D2 , and HD reactions. *J. Chem. Phys.*, 109:8929, 1998.

[57] E. Bodo, F. A. Gianturco, N. Balakrishnan, and A. Dalgarno. Chemical reactions in the limit of zero kinetic energy: virtual states and ramsauer minima in $F+H_2HF+H$. *J. Phys. B: At. Mol. Opt. Phys.*, 37:3641, 2004.

[58] P. F. Weck and N. Balakrishnan. Chemical reactivity of ultracold polar molecules: investigation of H+HCl and H+DCl collisions. *Eur. Phys. J. D*, 31:417, 2004.

[59] Joop J. Gilijamse, Steven Hoekstra, Sebastiaan Y. T. van de Meerakker, Gerrit C. Groenenboom, and Gerard Meijer. Near-threshold inelastic collisions using molecular beams with a tunable velocity. *Science*, 313(5793):1617–1620, 2006.

[60] Brian C. Sawyer, Benjamin K. Stuhl, Dajun Wang, Mark Yeo, and Jun Ye. Molecular beam collisions with a magnetically trapped target. *Phys. Rev. Lett.*, 101(20):203203, Nov 2008.

[61] G. B. Kistiakowsky and William P. Slichter. A high intensity source for the molecular beam. part *ii*. experimental. *Rev. Sci. Inst.*, 22(5):333–337, 1951.

[62] S. Goyal, D. L. Schutt, and G. Scoles. Vibrational spectroscopy of sulfur hexafluoride attached to helium clusters. *Phys. Rev. Lett.*, 69(6):933â936, 1992.

[63] Harold J. Metcalf and Peter van der Straten. *Laser Cooling and Trapping.* Springer„ 1999.

[64] C. J. Pethick and H. Smith. *Bose-Einstein Condensation in Dilute Gases.* Cambridge„ 2002.

[65] Markus Greiner, Olaf Mandel, Tilman Esslinger, Theodor W. Hänsch, and Imamanuel Bloch. Quantum phase transition from a superfluid to a Mott insulator in a gas of ultracold atoms. *Nature,*, 415:39â44, 2002.

[66] B. DeMarco and D. S. Jin. Onset of Fermi degeneracy in a trapped atomic gas. *Science*, 285:1703â1706, 1999.

[67] Zachary Dutton Lene Vestergaard Hau, S. E. Harris and Cyrus H. Behroozi. Light speed reduction to 17 meters per second in an ultracold atomic gas. *Nature*, 397:594â598, 1999.

[68] Steven Chu Mark A. Kasevich, Erling Riis and Ralph G. DeVoe. rf spectroscopy in an atomic fountain. *Phys. Rev. Lett.*, 63(6):612â615„ 1989.

[69] Immanuel Bloch, Jean Dalibard, and Wilhelm Zwerger. Many-body physics with ultracold gases. *Rev. Mod. Phys.*, 80:885, 2008.

[70] Lincoln D. Carr, David DeMille, Roman V. Krems, and Jun Ye. Cold and ultracold molecules: Science, technology, and applications. *New J. Phys.*, 11:055049, 2009.

[71] J. T. Bahns, W. C. Stwalley, and P. L. Gould. Laser cooling of molecules: A sequential scheme for rotation, translation, and vibration. *Journal of Chemical Physics*, 104:9689, 1996.

[72] G. Herzberg. *Molecular Spectra and Molecular Structure,*. Krieger, Malabar, (1989).

[73] M. D. Di Rosa. Laser-cooling molecules. *Eur. Phys. J. D*, 31:395â402, 2004.

[74] E. S. Shuman, J. F. Barry, D. R. Glenn, and D. DeMille. Radiative force from optical cycling on a diatomic molecule. *Phys. Rev. Lett.*, 103(22):223001, 2009.

[75] J. Doyle, B. Friedrich, R. V. Krems, and F. Masnou-Seeuws. Editorial: Quo vadis, cold molecules? *European Physical Journal D*, 31:149, 2004.

[76] Jeremy M. Sage, Sunil Sainis, Thomas Bergeman, and David DeMille. Optical production of ultracold polar molecules. *Phys. Rev. Lett.*, 94(20):203001, 2005.

[77] Matthieu Viteau, Amodsen Chotia, Maria Allegrini, Nadia Bouloufa, Olivier Dulieu, Daniel Comparat, and Pierre Pillet. Optical pumping and vibrational cooling of molecules. *Science*, 321:232–234, 2008.

[78] J. D. Miller, R. A. Cline, and D. J. Heinzen. Photoassociation spectrum of ultracold Rb atoms. *Phys. Rev. Lett.*, 71(14):2204–2207, 1993.

[79] C. Gabbanini, A. Fioretti, A. Lucchesini, S. Gozzini, and M. Mazzoni. Cold rubidium molecules formed in a magneto-optical trap. *Phys. Rev. Lett.*, 84(13):2814–2817, 2000.

[80] P. D. Lett, K. Helmerson, W. D. Phillips, L. P. Ratliff, S. L. Rolston, and M. E. Wagshul. Spectroscopy of Na_2 by photoassociation of laser-cooled Na. *Phys. Rev. Lett.*, 71(14):2200–2203, 1993.

[81] E. R. I. Abraham, W. I. McAlexander, C. A. Sackett, and Randall G. Hulet. Spectroscopic determination of the s-wave scattering length of lithium. *Phys. Rev. Lett.*, 74(8):1315–1318, 1995.

[82] A. Fioretti, D. Comparat, A. Crubellier, O. Dulieu, F. Masnou-Seeuws, and P. Pillet. Formation of cold Cs_2 molecules through photoassociation. *Phys. Rev. Lett.*, 80(20):4402–4405, 1998.

[83] A. N. Nikolov, E. E. Eyler, X. T. Wang, J. Li, H. Wang, W. C. Stwalley, and P. L. Gould. Observation of ultracold ground-state potassium molecules. *Phys. Rev. Lett.*, 82(4):703–706, 1999.

[84] Götz Zinner, Tomas Binnewies, Fritz Riehle, and Eberhard Tiemann. Photoassociation of cold Ca atoms. *Phys. Rev. Lett.*, 85(11):2292–2295, 2000.

[85] A. P. Mosk, M. W. Reynolds, T. W. Hijmans, and J. T. M. Walraven. Photoassociation of spin-polarized hydrogen. *Phys. Rev. Lett.*, 82(2):307–310, 1999.

[86] N. Herschbach, P. J. J. Tol, W. Vassen, W. Hogervorst, G. Woestenenk, J. W. Thomsen, P. van der Straten, and A. Niehaus. Photoassociation spectroscopy of cold $He(2^3S)$ atoms. *Phys. Rev. Lett.*, 84(9):1874–1877, 2000.

[87] C. Haimberger, J. Kleinert, M. Bhattacharya, and N. P. Bigelow. Formation and detection of ultracold ground-state polar molecules. *Phys. Rev. A*, 70(2):021402, 2004.

[88] D. Wang, J. Qi, M. F. Stone, O. Nikolayeva, H. Wang, B. Hattaway, S. D. Gensemer, P. L. Gould, E. E. Eyler, and W. C. Stwalley. Photoassociative production and trapping of ultracold KRb molecules. *Phys. Rev. Lett.*, 93(24):243005, 2004.

[89] Andrew J. Kerman, Jeremy M. Sage, Sunil Sainis, Thomas Bergeman, and David DeMille. Production and state-selective detection of ultracold RbCs molecules. *Phys. Rev. Lett.*, 92(15):153001, 2004.

[90] Roahn Wynar, R. S. Freeland, D. J. Han, C. Ryu, and D. J. Heinzen. Molecules in a bose-einstein condensate. *Science*, 287:1016–1019, 2000.

[91] Jordan M. Gerton, Dmitry Strekalov, Ionut Prodan, and Randall G. Hulet. Direct observation of growth and collapse of a Bose-Einstein condensate with attractive interactions. *Nature*, 408:692–695, 2000.

[92] C. McKenzie, J. Hecker Denschlag, H. Häffner, A. Browaeys, Luís E. E. de Araujo, F. K. Fatemi, K. M. Jones, J. E. Simsarian, D. Cho, A. Simoni, E. Tiesinga, P. S. Julienne, K. Helmerson, P. D. Lett, S. L. Rolston, and W. D. Phillips. Photoassociation of sodium in a Bose-Einstein condensate. *Phys. Rev. Lett.*, 88(12):120403, 2002.

[93] Thorsten Köhler, Krzysztof Góral, and Paul S. Julienne. Production of cold molecules via magnetically tunable Feshbach resonances. *Rev. Mod. Phys.*, 78(4):1311–1361, 2006.

[94] E. A. Donley, N. R. Claussen, S. T. Thompson, and C. E. Wieman. Atom-molecule coherence in a Bose-Einstein condensate. *Nature*, 417:529, 2002.

[95] Kevin E. Strecker, Guthrie B. Partridge, and Randall G. Hulet. Conversion of an Atomic Fermi Gas to a Long-Lived Molecular Bose Gas. *Phys. Rev. Lett.*, 91(8):080406, 2003.

[96] K. Xu, T. Mukaiyama, J. R. Abo-Shaeer, J. K. Chin, D. E. Miller, and W. Ketterle. Formation of quantum-degenerate sodium molecules. *Phys. Rev. Lett.*, 91(21):210402, 2003.

[97] Cindy A. Regal, Christopher Ticknor, John L. Bohn, and Deborah S. Jin. Creation of ultracold molecules from a Fermi gas of atoms. *Nature*, 424:47–50, 2003.

[98] Jens Herbig, Tobias Kraemer, Michael Mark, Tino Weber, Cheng Chin, Hanns-Christoph Nagerl, and Rudolf Grimm. Preparation of a pure molecular quantum gas. *Science*, 301:1510–1513, 2003.

[99] Cheng Chin, Rudolf Grimm, Paul Julienne, and Eite Tiesinga. Feshbach resonances in ultracold gases. *Rev. Mod. Phys.*, 82(2):1225–1286, 2010.

[100] L. Costa, J. Brachmann, A.-C. Voigt, C. Hahn, M. Taglieber, T. W. Hänsch, and K. Dieckmann. s-wave interaction in a two-species Fermi-Fermi mixture at a narrow Feshbach resonance. *Phys. Rev. Lett.*, 105(12):123201, 2010.

[101] Rekishu Yamazaki, Shintaro Taie, Seiji Sugawa, and Yoshiro Takahashi. Submicron spatial modulation of an interatomic interaction in a Bose-Einstein condensate. *Phys. Rev. Lett.*, 105(5):050405, 2010.

[102] Benjamin L. Brown, Alexander J. Dicks, and Ian A. Walmsley. Coherent control of ultracold molecule dynamics in a magneto-optical trap by use of chirped femtosecond laser pulses. *Phys. Rev. Lett.*, 96(17):173002, 2006.

[103] John Weiner, Vanderlei S. Bagnato, Sergio Zilio, and Paul S. Julienne. Experiments and theory in cold and ultracold collisions. *Rev. Mod. Phys.*, 71(1):1–85, 1999.

[104] John M. Doyle, Bretislav Friedrich, Jinha Kim, and David Patterson. Buffer-gas loading of atoms and molecules into a magnetic trap. *Phys. Rev. A*, 52(4):R2515–R2518, Oct 1995.

[105] Jinha Kim, Bretislav Friedrich, Daniel P. Katz, David Patterson, Jonathan D. Weinstein, Robert DeCarvalho, and John M. Doyle. Buffer-gas loading and magnetic trapping of atomic europium. *Phys. Rev. Lett.*, 78(19):3665–3668, May 1997.

[106] Jonathan D. Weinstein, Robert deCarvalho, Jinha Kim, David Patterson, Bretislav Friedrich, and John M. Doyle. Magnetic trapping of atomic chromium. *Phys. Rev. A*, 57(5):R3173–R3175, May 1998.

[107] Jonathan D. Weinstein, Robert deCarvalho, Thierry Guillet, Bretislav Friedrich, and John M. Doyle. Magnetic trapping of calcium monohydride molecules at millikelvin temperatures. *Nature*, 395:148–150, 1998.

[108] Norman F. Ramsey. *Molecular Beams*. The International Series of Monographs on Physics, Oxford University Press, 1956.

[109] B. Ghaffari, J. M. Gerton, W. I. McAlexander, K. E. Strecker, D. M. Homan, and R. G. Hulet. Laser-free slow atom source. *Phys. Rev. A*, 60(5):3878–3881, Nov 1999.

[110] S. A. Rangwala, T. Junglen, T. Rieger, P. W. H. Pinkse, and G. Rempe. Continuous source of translationally cold dipolar molecules. *Phys. Rev. A*, 67(4):043406, Apr 2003.

[111] Stefan Willitsch, Martin T. Bell, Alexander D. Gingell, Simon R. Procter, and Timothy P. Softley. Cold reactive collisions between laser-cooled ions and velocity-selected neutral molecules. *Phys. Rev. Lett.*, 100(4):043203, Jan 2008.

[112] Hendrick L. Bethlem, Giel Berden, and Gerard Meijer. Decelerating neutral dipolar molecules. *Phys. Rev. Lett.*, 83(8):1558–1561, 1999.

[113] Hendrick L. Bethlem, Giel Berden, Floris M. H. Crompvoets, Rienk T. Jongma, André J. A. van Roij, and Gerard Meijer. Electrostatic trapping of ammonia molecules. *Nature*, 406:491–494, 2000.

[114] Eric R. Hudson, Christopher Ticknor, Brian C. Sawyer, Craig A. Taatjes, H. J. Lewandowski, J. R. Bochinski, J. L. Bohn, and Jun Ye. Production of cold formaldehyde molecules for study and control of chemical reaction dynamics with hydroxyl radicals. *Phys. Rev. A*, 73(6):063404, 2006.

[115] Sebastian Jung, Eberhard Tiemann, and Christian Lisdat. Cold atoms and molecules from fragmentation of decelerated SO_2. *Phys. Rev. A*, 74(4):040701, 2006.

[116] J. R. Bochinski, Eric R. Hudson, H. J. Lewandowski, Gerard Meijer, and Jun Ye. Phase space manipulation of cold free radical OH molecules. *Phys. Rev. Lett.*, 91(24):243001, 2003.

[117] Sebastiaan Y. T. van de Meerakker, Paul H. M. Smeets, Nicolas Vanhaecke, Rienk T. Jongma, and Gerard Meijer. Deceleration and electrostatic trapping of OH radicals. *Phys. Rev. Lett.*, 94(2):023004, 2005.

[118] Steven Hoekstra, Joop J. Gilijamse, Boris Sartakov, Nicolas Vanhaecke, Ludwig Scharfenberg, Sebastiaan Y. T. van de Meerakker, and Gerard Meijer. Optical pumping of trapped neutral molecules by blackbody radiation. *Phys. Rev. Lett.*, 98(13):133001, 2007.

[119] Sebastiaan Y.T. van de Meerakker, Irena Labazan, Steven Hoekstra, Jochen Küpper, and Gerard Meijer. Production and deceleration of a pulsed beam of metastable $NH(a^1D)$ radicals. *J. Phys. B: At. Mol. Opt. Phys.*, 39:S1077, 2006.

[120] Brian C. Sawyer, Benjamin K. Stuhl, Dajun Wang, Mark Yeo, and Jun Ye. Molecular beam collisions with a magnetically trapped target. *Phys. Rev. Lett.*, 101:203203, 2008.

[121] Floris M.H. Crompvoets, Hendrick L. Bethlem, Rienk T. Jongma, and Gerard Meijer. A prototype storage ring for neutral molecules. *Nature*, 411:174–176, 2001.

[122] Nicolas Vanhaecke, Urban Meier, Markus Andrist, Beat H. Meier, and Frédéric Merkt. Multistage Zeeman deceleration of hydrogen atoms. *Phys. Rev. A*, 75:031402(R), 2007.

[123] E. Narevicius, C. G. Parthey, A. Libson, J. Narevicius, E. Chavez, U. Even, and M. G. Raizen. Towards magnetic slowing of atoms and molecules. *New J. Phys.*, 9:358, 2007.

[124] Edvardas Narevicius, Adam Libson, Christian G. Parthey, Isaac Chavez, Julia Narevicius, Uzi Even, and Mark G. Raizen. Stopping supersonic beams with a series of pulsed electromagnetic coils: An atomic coilgun. *Phys. Rev. Lett.*, 100(9):093003, 2008.

[125] Edvardas Narevicius, Adam Libson, Christian G. Parthey, Isaac Chavez, Julia Narevicius, Uzi Even, and Mark G. Raizen. Stopping supersonic oxygen with a series of pulsed electromagnetic coils: A molecular coilgun. *Phys. Rev. A*, 77(5):051401, 2008.

[126] S. D. Hogan, A. W. Wiederkehr, H. Schmutz, and F. Merkt. Magnetic trapping of hydrogen after multistage Zeeman deceleration. *Phys. Rev. Lett.*, 101(14):143001, 2008.

[127] Ludwig Scharfenberg, Henrik Haak, Gerard Meijer, and Sebastiaan Y. T. van de Meerakker. Operation of a stark decelerator with optimum acceptance. *Phys. Rev. A*, 79(2):023410, 2009.

[128] Andreas Osterwalder, Samuel A. Meek, Georg Hammer, Henrik Haak, and Gerard Meijer. Deceleration of neutral molecules in macroscopic traveling traps. *Phys. Rev. A*, 81(5):051401, 2010.

[129] A. W. Wiederkehr, S. D. Hogan, and F. Merkt. Phase stability in a multistage zeeman decelerator. *Phys. Rev. A*, 82(4):043428, Oct 2010.

[130] L. Dunoyer. *Comptes Rendus*, 157:594, 1911.

[131] O. Stern. *Zeit. f. Physik*, 39:751, 1926.

[132] F. Knauer and O. Stern. *Zeit. f. Physik*, 53:766, 1929.

[133] I. I. Rabi, J. R. Zacharias, S. Millman, and P. Kusch. *Phys. Rev.*, 53:318, 1938.

[134] J. M. B. Kellogg, I. I. Rabi, N. F. Ramsey, and J. R. Zacharias. The magnetic moments of the proton and the deuteron. The radiofrequency spectrum of H_2 in various magnetic fields. *Phys. Rev.*, 56:728–743, 1939.

[135] P. Kusch, S. Millman, and I. I. Rabi. The radiofrequency spectra of atoms hyperfine structure and Zeeman effect in the ground state of Li^6, Li^7, K^39 and K^41. *Phys. Rev.*, 57:765–780, 1940.

[136] B. C. Regan, Eugene D. Commins, Christian J. Schmidt, and David DeMille. New limit on the electron electric dipole moment. *Phys. Rev. Lett.*, 88:071805, 2002.

[137] Björn Brezger, Lucia Hackermüller, Stefan Uttenthaler, Julia Petschinka, Markus Arndt, and Anton Zeilinger. Matter-wave interferometer for large molecules. *Phys. Rev. Lett.*, 88:100404, 2002.

[138] M. Sander, L. A. Chewter, K. Müller-Dethlefs, and E. W. Schlag. High-resolution zero-kinetic-energy photoelectron spectroscopy of nitric oxide. *Phys. Rev. A*, 36:4543–4546, 1987.

[139] B. E. Sauer, Jun Wang, and E. A. Hinds. Anomalous spin-rotation coupling in the $X^2\Sigma^+$ state of YbF. *Phys. Rev. Lett.*, 74:1554, 1995.

[140] A. Amy-Klein, L. F. Constantin, R. J. Butcher, G. Charton, and Ch. Chardonnet. High-resolution spectroscopy with a molecular beam at 10.6 μm. *Phys. Rev. A*, 63:013404, 2000.

[141] John B. Fenn, Matthias Mann, Chin Kai Meng, Shek Fu Wong, and Craig M. Whitehouse. Electrospray ionization for mass spectrometry of large biomolecules. *Science*, 246:64–71, 1989.

[142] William D. Phillips. Nobel lecture: Laser cooling and trapping of neutral atoms. *Rev. Mod. Phys.*, 70(3):721–741, 1998.

[143] Claude N. Cohen-Tannoudji. Nobel lecture: Manipulating atoms with photons. *Rev. Mod. Phys.*, 70(3):707–719, 1998.

[144] Steven Chu. Nobel lecture: The manipulation of neutral particles. *Rev. Mod. Phys.*, 70(3):685–706, 1998.

[145] Wolfgang Ketterle. Nobel lecture: When atoms behave as waves: Bose-einstein condensation and the atom laser. *Rev. Mod. Phys.*, 74(4):1131–1151, 2002.

[146] E. A. Cornell and C. E. Wieman. Nobel lecture: Bose-Einstein condensation in a dilute gas, the first 70 years and some recent experiments. *Rev. Mod. Phys.*, 74(3):875–893, 2002.

[147] Immanuel Bloch, Jean Dalibard, and Wilhelm Zwerger. Many-body physics with ultracold gases. *Rev. Mod. Phys.*, 80(3):885–964, 2008.

[148] E. S. Shuman, J. F. Barry, D. R. Glenn, and D. DeMille. Radiative force from optical cycling on a diatomic molecule. *Phys. Rev. Lett.*, 103:223001, 2009.

[149] G. Scoles, D. Bassi, D. Buck, U.and Laine, and C. Braun. *Atomic and Molecular Beam Methods, Vol. I. Applied Optics, 28 :16.* 1989.

[150] J. Peter Toennies and Klaus Winkelmann. Theoretical studies of highly expanded free jets: Influence of quantum effects and a realistic intermolecular potential. *J. Chem. Phys.*, 66:3965, 1977.

[151] Nicolas SAQUET. *REALISATION D'UN DECELERATEUR STARK POUR ATOMES ET MOLECULES DE RYDBERG.* PhD thesis, UNIVERSITÉ PARIS SUD XI, 2009.

[152] Y. P. Raizer. *Gas discharge physics.* Springer-Verlag, Berlin, 1997.

[153] S. Davis, D. T. Anderson, G. Duxbury, and D. J. Nesbitt. Jet-cooled molecular radicals in slit supersonic discharges: sub-doppler infrared studies of methyl radical. *Journal of Chemical Physics*, 107:5661, 1997.

[154] Erik Wagenaars. *Plasma Breakdown of Low-pressure Gas Discharge.* PhD thesis, Technische Universiteit Eindhoven, 2006.

[155] A. Bogaerts and R. Gijbels. Modeling of metastable argon atoms in a direct-current glow discharge. *Phys. Rev. A*, 52:3743, 1995.

[156] A. Benston, C. Yang, and W. W. Harrison. Microsecond pulsed glow discharge opticall emmision spectrometry- investigation of temporal emmision characteristics. *J. Anal. At. Spectrom.*, 15:1279, 2000.

[157] W. Hang, W. O. Walden, and W. W. Harrison. Microsecond pulsed glow discharge as an analytical spectroscopic source. *Anal. Chem.*, 68:1148, 1996.

[158] J. A. Aparicio, J. A. del Val, V. R. Gonzalez, M. A. Gigosas, C. Perez, I. de la Roza, and S. Mar. Measurement of excitation equilibrium departure evolution in an argon pulsed plasma. *J. Phys. Soc. Jpn.*, 68:3885, 1999.

[159] Azer TRIMECHE. Décélération magnétique dâun jet supersonique de radicaux libres. Master's thesis, Université Paris-Sud 11, 2010.

[160] O. Stern. Ein weg zur experimentellen prüfung der richtungsquantelung im magnetfeld. *Zeitschrift für Physik*, 7:249, 1921.

[161] W. Gerlach and O. Stern. Das magnetische moment des silberatoms. *Zeitschrift für Physik*, 9:353–355, 1922.

[162] B. Friedrich and D. Herschbach. Stern and Gerlach: How a bad cigar helped reorient atomic physics. *Physics Today*, 56:53, 2003.

[163] T.E. Phipps and J.B. Taylor. The magnetic moment of the hydrogen atom. *Physical Review*, 29:309–320.

[164] H. G. Bennewitz and W. Paul. *Z. Phys.*, 139:489, 1954.

[165] H. G. Bennewitz and W. Paul. *Z. Phys.*, 141:6, 1955.

[166] H Friedburg and W. Paul. *Naturewissenschaften*, 38:159, 1951.

[167] C. H. Townes. *Proc. Nat. Acad. Sci.*, 80:7679, 1983.

[168] W. H. Wing. On neutral particle trapping in quasistatic electromagnetic fields. *Prog. Quant. Electr.*, 8:181, 1984.

[169] Pritchard D. E. Ketterle, W. Trapping and focusing ground state atoms with static fields. *J. Appl. Phys. B*, 54:403, 1992.

[170] *NIST: Atomic Spectra Database, Ar I energy levels. Available from: http://physics.nist.gov/PhysRefData/Handbook/Tables/argontable5.htm.*

[171] Michael S. Elioff, James J. Valentini, and David W. Chandler. Subkelvin cooling NO molecules via "billiard-like" collisions with argon. *Science*, 302:1940–1943, 2003.

[172] Dima Egorov, Thierry Lahaye, Wieland Schöllkopf, Bretislav Friedrich, and John M. Doyle. Buffer-gas cooling of atomic and molecular beams. *Phys. Rev. A*, 66(4):043401, 2002.

[173] R. Fulton, A. I. Bishop, and P. F. Barker. Optical stark decelerator for molecules. *Phys. Rev. Lett.*, 93(24):243004, Dec 2004.

[174] Sebastiaan Y. T. van de Meerakker, Hendrick L. Bethlem, and Gerard Meijer. Taming molecular beams. *Nature Physics*, 4:595–602, 2008.

[175] Hendrick L. Bethlem, Giel Berden, André J. A. van Roij, Floris M. H. Crompvoets, and Gerard Meijer. Trapping neutral molecules in a traveling potential well. *Phys. Rev. Lett.*, 84(25):5744–5747, 2000.

[176] S. D. Hogan, D. Sprecher, M. Andrist, N. Vanhaecke, and F. Merkt. Zeeman deceleration of H and D. *Phys. Rev. A*, 76:023412, 2007.

[177] Sebastiaan Y. T. van de Meerakker, Nicolas Vanhaecke, Hendrick L. Bethlem, and Gerard Meijer. Higher-order resonances in a stark decelerator. *Phys. Rev. A*, 71(5):053409, 2005.

[178] B.C. Sawyer, B.K. Stuhl, B.L. Lev, J. Ye, and E.R. Hudson. Mitigation of loss within a molecular stark decelerator. *Eur. Phys. J. D*, 48:197–209, 2008.

[179] Horst Conrad Samuel A. Meek and Gerard Meijer. Trapping molecules on a chip. *Science*, 324:1699–1702, 2009.

[180] Hendrick Lucas Bethlem. *Deceleration and Trapping of Polar Molecules using Time-varying Electric Fields.* PhD thesis, Katholieke Universiteit Nijmegen, 2002.

[181] A. W. Wiederkehr, S. D. Hogan, B. Lambillotte, M. Andrist, H. Schmutz, J. Agner, Y. Salathé, and F. Merkt. Trapping deuterium atoms. *Phys. Rev. A*, 81(2):021402, 2010.

[182] Hendrick L. Bethlem, Floris M. H. Crompvoets, Rienk T. Jongma, Sebastiaan Y. T. van de Meerakker, and Gerard Meijer. Deceleration and trapping of ammonia using time-varying electric fields. *Phys. Rev. A*, 65:053416, 2002.

[183] Hendrick L. Bethlem, Giel Berden, and Gerard Meijer. Decelerating neutral dipolar molecules. *Phys. Rev. Lett.*, 83:1558, 1999.

[184] Edwin M. McMillan. The synchrotron—a proposed high energy particle accelerator. *Phys. Rev.*, 68:143, 1945.

[185] Sebastiaan Y.T. van de Meerakker. *Deceleration and Electrostatic Trapping of OH Radicals.* PhD thesis, Radboud Universiteit Nijmegen, 2006.

[186] Jr. S. Humphries. *Principle of charged part accelerators.* Wiley, New York, 1986.

[187] Sebastiaan Y. T. van de Meerakker, Nicolas Vanhaecke, Hendrick L. Bethlem, and Gerard Meijer. Transverse stability in a Stark decelerator. *Phys. Rev. A*, 73(2):023401, 2006.